Dongli Li

St Anne's College

Supervisor

Robin Cleveland
Antoine Jérusalem

Computational and experimental study of shock wave interactions with cells

A thesis submitted for the degree of Doctor of Philosophy

Michaelmas 2016

For my grandfather.

A thesis submitted for the degree of Doctor of Philosophy.

Computational and experimental study of shock wave interactions with cells

By Dongli Li, St Anne's College.

Submitted Michaelmas 2016.

Extended Abstract

This thesis presents a combined numerical and experimental study on the response of kidney cells to shock waves. The motivation was to develop a mechanistic model of cell deformation in order to improve the clinical use of shock waves, by either enhancing their therapeutic action against target cells or minimising their impact on healthy cells.

An ultra-high speed camera was used to visualise individual cells, embedded in tissue-mimicking gel, in order to measure their deformation when subject to a shock wave from a clinical shock wave source. Advanced image processing was employed to extract the contour of the cell from the images. The evolution of the observed cell contour revealed a relatively small deformation during the compressional phase and a much larger deformation during the tensile phases of a shock wave. The experimental observations were captured by a numerical model which describes the volumetric cell response with a bilinear Equation of State and the deviatoric cell response with a viscoelastic framework. Experiments using human kidney cancer cells (CAKI-2) and noncancerous kidney cells (HRE and HK-2) were compared to the model in order to determine their mechanical properties. The differences between cancerous and noncancerous cells were exploited to demonstrate a design process by which shock waves may be able to improve the specificity on targeted cancer cells while having minimal effect on normal cells.

The cell response to shock waves was studied in a more biophysically realistic environment to include influence of cell size, shape and orientation, and the presence of neighbouring cells. The most significant difference was predicted when cells were in a cluster in which case the presence of neighbouring cells resulted in a four-fold increase on the von Mises stress and the membrane strain.

Finally the numerical model was extended to capture the effect of cell damage using one of two paradigms. In the first paradigm the model captured microdamage during one shock wave but then assumed that the cell recovered by the time the next shock wave arrived. The second model allowed microdamage to accumulate with increasing number of shock waves. These models may be able to explain the strong effect that shock wave loading rate has on tissue damage.

In conclusion a validated numerical model has been developed which provides a mechanistic understanding of how cells respond to shock waves. The model has application in suggesting improved strategies for current uses of shock waves, e.g., lithotripsy, as well as opening up new indications such as cancer treatment.

Statement of Originality

I hereby declare that this submission is my own work and to the best of my knowledge it contains no materials previously published or written by another person, or substantial proportions of material which have been accepted for the award of any other degree or diploma at the University of Oxford or any other educational institution, except where due acknowledgement is made in the thesis.

Any contribution made to the research by others, with whom I have worked at the University of Oxford or elsewhere, is explicitly acknowledged in the thesis.

I also declare that the intellectual content of this thesis is the product of my own work, except to the extent that assistance from others in the project's design and conception or in style, presentation and linguistic expression is acknowledged.

Dongli Li.
20 December 2016.

Acknowledgements

I would like to thank both of my supervisors, Professor Robin Cleveland and Professor Antoine Jérusalem. Robin for continuously providing me with valuable inspirations and guidance throughout my DPhil, which is extremely important for shaping my research, and Antoine for many one-to-one meetings and helping me establish collaboration and network, which is essential for my project and to develop my research career.

My research has greatly benefited from the endeavours of fellow researchers undertaking complementary work. My particular thanks go to Dr. Antonio Pellegrino from the Impact Engineering Laboratory and Andre Hallack from the Biomedical Image Analysis group at the University of Oxford. Antonio provided immense help in operating the ultra-high speed camera which is a critical component in the experiment. Andre helped perform advanced image processing algorithm and offered inspirations for the work. I am deeply grateful for their effort and time spent for my project. It is a great privilege to view both of these individuals as friends as well as colleagues.

I must express particular gratitude to Professor Nik Petrinic for his in-kind contribution on the experimental facilities and advices. I would also like to thank people from both of my labs (BUBBL and CMM), in particular, Sandra Nwokeoha, Kya Shoar, Emily Kwong, Daniel Barba and Dr. Lili Zhang for their day-to-day support and encouragement during my DPhil.

Finally I must express my appreciation for my wonderful family. My parents' advices, support and encouragement play an important role in my DPhil study. My grandfather's work ethic and competitive spirit in his own career has always been my source of inspiration, without which I would not be where I am today. Above all, this thesis is my gift to my family, especially my grandfather.

I kindly acknowledge the RCUK Digital Economy Programme grant number EP/G036861/1 (Oxford Centre for Doctoral Training in Healthcare Innovation) and Oxford Centre for Drug Delivery Devices for their financial support during this project.

Dissemination

Peer-Reviewed Journal Papers

Dongli Li, Antonio Pellegrino, Andre Hallack, Nik Petrinic, Antoine Jérusalem and Robin Cleveland. Charaterisation of single cell response to shock waves and *in silico* optimisation of shock wave-mediated therapy. *Biophysical jouurnal*. (under review)

Lili Zhang, Zesheng Zhang, John Jasa, Dongli Li, Robin Cleveland, Mehrdad Negahban and Antoine Jérusalem. A molecular mechanistic perspective on cell membrane response to therapeutic shock waves. *Scientific Reports*. (under review)

Conference Presentations and Posters

Dongli Li, Robin Cleveland and Antoine Jérusalem. Numerical modelling of shock wave interactions with kidney cells. Oral presentation, *11th. World Congress on Computational Mechanics (WCCM XI), 2014*.

Dongli Li, Antonio Pellegrino, Andre Hallack, Nik Petrinic, Antoine Jérusalem and Robin Cleveland. Oral presentation and junior co-chair, Ultra-high speed imaging and modelling of shock wave interactions with cells. *International Society for Therapeutic Ultrasound, 2016*.

Dongli Li, Robin Cleveland and Antoine Jérusalem. Numerical modelling of cell response to shock waves. *Best poster, Quantitative Biology Oxford, 2016*.

Contents

List of Figures

List of Tables

Acronyms

AFM	Atomic force microscopy
EoS	Equation of State
FBS	Fetal bovine serum
FEM	Finite element method
FOPH	Fibre-optic probe hydrophone
HIFU	High intensity focussed ultrasound
MMRE	Multifrequency magnetic resonance elastography
MPM	Multiphoton microscope
MRE	Magnetic resonance elastography
NL-means	Non-local means
SDUV	Shearwave dispersion ultrasound vibrometry

CHAPTER 1

Introduction

Shock waves have been applied in several medical therapies such as lithotripsy, orthotripsy, histotripsy and have been suggested for cancer therapy. The premise of this work is the study of these shock wave mediated treatments, including the underlying biophysics and the experimental optimisation of shock waves for better therapeutic efficacy.

1.1 Background

Shock waves have been used medically for decades in a procedure called lithotripsy in which shock waves fragment kidney stones into a size that can be naturally expelled from the body through ureter. However, clinical reports have shown that shock waves can also lead to renal haemorrhage and scarring with a permanent loss of functional renal volume during treatment (McAteer and Evan, 2008; Brümmer et al., 1990). It has also been suggested that shock waves can result in some complications including metabolic acidosis, high level of potassium and imbalance of body fluid (Stewart et al., 2009; Lingeman et al., 1989). Shock wave lithotripsy has also been reported to be associated with the development of some chronic diseases like diabetes and hypertension (McAteer and Evan, 2008). These side-effects motivate better understanding of shock wave damage to soft tissue in order to achieve high therapeutic efficacy while minimising interference

on normal healthy tissue. However, the mechanisms for shock wave injury are not fully understood. Two major hypotheses for tissue damage have been proposed: cavitation and direct mechanical forces (e.g., shear stress and tension), which will be discussed in details in Chapter 2.

Shock waves have also been employed for orthotripsy, which treats musculoskeletal disorders such as plantar fasciitis, tendon pain, calcific tendonitis of the shoulder and non-unions or delayed unions of long bone fractures (Wang, 2003; Rompe et al., 2009). The mechanism by which shock waves have an effect on musculoskeletal conditions is not well understood. One of the hypotheses is that the disruption of tissue by shock waves results in "microtrauma" which then induces neovascularisation to improve blood supply and tissue regeneration. The increased permeability of the vessel wall may also promote the healing process (Wang, 2003).

A relatively new field for shock wave application is histotripsy, which incites a localised cavitation cloud to mechanically fractionate tissue (Maxwell et al., 2010). Research studies have observed the precise formation of lesions in target phantoms and tissues (Lin et al., 2014; Maxwell et al., 2010). Cavitation cloud histotripsy activates cavitation bubble clouds within the portion of focal zone where the negative pressure exceeds the intrinsic threshold of dense bubble cloud. The repeated expansion and contraction of the bubble clouds mechanically disintegrate tissue without thermal lesions (Khokhlova et al., 2015).

Shock waves have also been suggested for cancer therapy. It has been reported that besides mechanically rupturing cancer cells, shock waves may temporarily increase the membrane permeability (sonoporation effect) to allow molecules in the surrounding medium to diffuse into cells, which provides a mechanism for shock wave-mediated therapeutic drug delivery and gene transfer (Murata et al., 2007). Meanwhile, some experimental results have shown a positive influence of shock waves on suppressing tumour growth and selectively killing malignant cells (Gamarra et al., 1993; Steinhauser and Schmidt, 2014). The mechanisms by which shock waves affect cancer cells, however, are not well understood.

Understanding the underlying mechanisms is important to help predict cell or tissue behaviour subject to shock waves and thus allow for the exploration of better treatment outcomes such as enhanced drug delivery and reduced side-

effects on normal healthy tissue.

Many *in vitro* studies have focussed on optimising different bioeffects (e.g., cell permeability and viability) induced by therapeutic ultrasound such as high intensity focussed ultrasound (HIFU) and shock waves, by experimentally studying the influence of acoustic parameters on cells (Kodama et al., 2002; Karshafian et al., 2009). The studies have found that both cell viability and permeability are strongly dependent on the acoustic loading, and the degree of viability and permeabilisation are inversely correlated, hence a trade-off between sufficient delivery and excessive toxicity needs to be managed through optimised acoustical parameters.

For focussed ultrasound mediated drug delivery, the optimisation of acoustic parameters is based on the therapeutic ratio which is the number of reversibly permeabilised cells divided by that of non-viable cells with the same exposure (Karshafian et al., 2009). The therapeutic ratio was found to initially increase with acoustic pressure, pulse duration, pulse repetition frequency and insonation time, reach a maximum and then decrease. Furthermore, lower frequency ultrasound pulses were found to be more effective at both permeabilising and killing cells (Karshafian et al., 2009).

For shock wave mediated delivery, an experimental study has also demonstrated that the gene transfection induced by lithotripter shock waves was roughly 15 times greater than by direct injection alone (Bao et al., 1998). The sonoporation effect on the cell membrane was found to be correlated to the number of shock waves applied, with the percentage of permeabilised cells levelling off after a couple of shock wave pulses (Kodama et al., 2002).

In summary, the experimental studies have showed promising results on acoustic wave mediated drug delivery: 70%-90% viable cells with 30%-70% of fluorescent molecule internalisation (Karshafian et al., 2009; Larina et al., 2005; Mehier-Humbert et al., 2005; Kodama et al., 2002). However, the data vary largely due to different experimental settings (e.g., molecules for delivery and sample variability) and are strongly limited by experimental resources.

Therefore, I propose to study cell interactions with therapeutic shock waves through a numerical means in order to better understand the underlying mechanisms of cell response to shock waves, thus facilitating the optimisation of thera-

peutic outcomes of shock wave mediated treatments while minimising side-effects on surrounding healthy tissue. A 3D continuum model was developed with a combined fluid and hyper-viscoelastic material framework to simulate single cell deformation in response to shock waves (strain rate typically above 10^4/s). The model was calibrated and validated against experimental observations of single cell deformation under the action of shock waves using ultra-high speed imaging. The numerical simulation was then used to analyse the development of stress and strain fields under the compressive and tensile phases of a shock wave, from which insights into the mechanisms of cell destruction and sonoporation can be obtained. The analysis also provides the basis for the optimisation of shock wave input for different therapeutic outcomes.

This work focuses initially on kidney, which has both lithotripsy and cancer applications. However, the model can be extended to other organs.

1.2 Scope of this work

The work begins with the experimental observation of single cell deformation under shock wave exposure, which is captured by an ultra-high speed imaging experiment. The description of the experimental setup, imaging procedure and post-imaging processing are described in Chapter 3. Following it, detailed experimental results of cell deformation in response to shock waves are presented in Chapter 4. In this chapter, the comparison of cell response from different cell lines (e.g. invasive cancer cells, healthy normal cells and virus transformed immortalised cells) is also included. In Chapter 5, a numerical model which captures the experimental measurement is presented. The model uses a constitutive framework which combines the acoustic Equation of State for the volumetric response and a non-linear viscoelasticity for the deviatoric response. The mechanical properties of the three cell types in response to shock waves are calibrated and validated against the experimental observations using the proposed numerical model, see Chapter 6. This chapter also proposes two designed shock wave profiles to achieve cancer cell specific bioeffects (sonoporation or cell damage) while minimising the interference on surrounding healthy cells. Finally, moving towards a more biophysically realistic scenario, Chapter 7 presents the influence of biological factors that are important *in vitro* or *in vivo*, such as cell size, shape, orientation and neighbouring cell clusters on the shock wave interactions with cells. Further-

more, potential damage mechanism induced during each shock wave exposure is discussed in Chapter 8, which may explain the noncavitational effects observed in the experiments using multiple shock loading.

CHAPTER 2

Prior work on cell interactions with acoustic waves

This chapter briefly reviews the physics of shock waves and two major hypotheses of underlying mechanisms of acoustic wave induced bioeffects. It also provides a comprehensive summary of studies on cell interactions with acoustic waves using experimental and computational methods. A summary of mechanical properties of cell components and kidney tissues is also provided.

2.1 Shock waves

A shock wave is an acoustic wave characterised by the presence of a rapid pressure jump due to the acoustic non-linearity where the velocity of the sound wave increases with the increasing pressure, which steepens the waveform. For very high sound intensities, the wave crest assumes a sawtooth appearance. A clinically applicable shock wave is formed when a balance between the non-linear distortion and absorption of the waveform in tissue is attained, therefore the shock front normally has a rise time of 10 ns to 100 ns instead of presenting a discontinuity of pressure at the shock front. Figure 2.1(a) shows an analytical shock wave profile that mimics a pressure wave measured at the focus of a lithotripter (Dornier HM3) (Cleveland and McAteer, 2012). The peak positive pressure in this example is 40 MPa after a transient pressure jump of less than 10 ns from the ambient pressure. The compressional phase of the shock wave (i.e. positive pressure phase) lasts

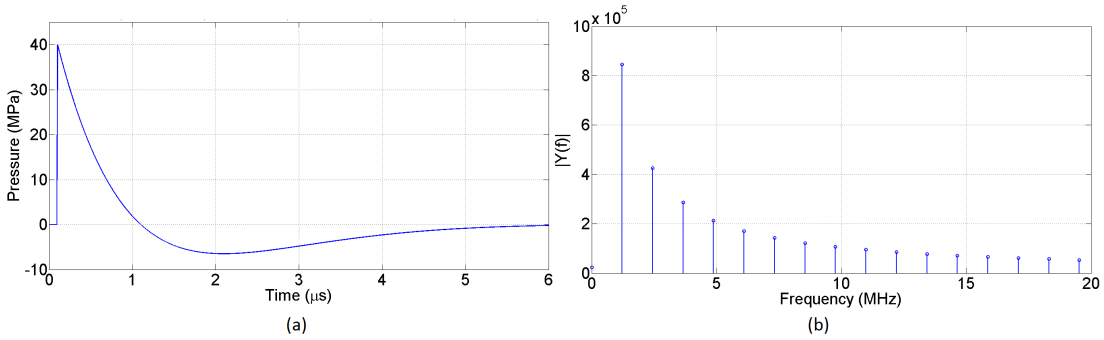

Figure 2.1: Full analytical shock wave representing a pressure wave measured at the focus of a lithotripter (Dornier HM3) (Cleveland and McAteer, 2012): (a) Shock wave profile in time domain (b) in frequency spectrum

for around 1 μs and is followed by a tensile phase with a lower negative pressure (around -7 MPa). Figure 2.1(b) shows the frequency components of the shock wave, indicating a broadband frequency spectrum.

2.1.1 Mechanism hypotheses of cell response to shock waves

Two major hypotheses have been proposed to explain the mechanisms for acoustic effects on cell viability and permeability: cavitation and direct mechanical forces (e.g., shear stress and tension).

2.1.1.1 Cavitation

Acoustic cavitation is caused by the negative pressure component of a shock wave rupturing the medium it is propagating through. This process creates expanding voids and bubbles. The violent collapse of the bubble emits microjetting and secondary shock waves which are damaging to the surrounding tissue (Church, 1989). As shown in Figure 2.2(c) in an *in vitro* study of lithotripsy induced cavitation (Coleman et al., 1992), an initial acoustic emission was released at $t = 0$ when the bubble collapsed encountering the high pressure phase of the pulse, then the bubble expanded for 200 μs (Figure 2.2(b)) which is longer than the shock wave duration (10 μs, Figure 2.2(a)) before it eventually collapsed, releasing a secondary shock wave exhibiting a much stronger magnitude than the initial pulse (a factor of 10).

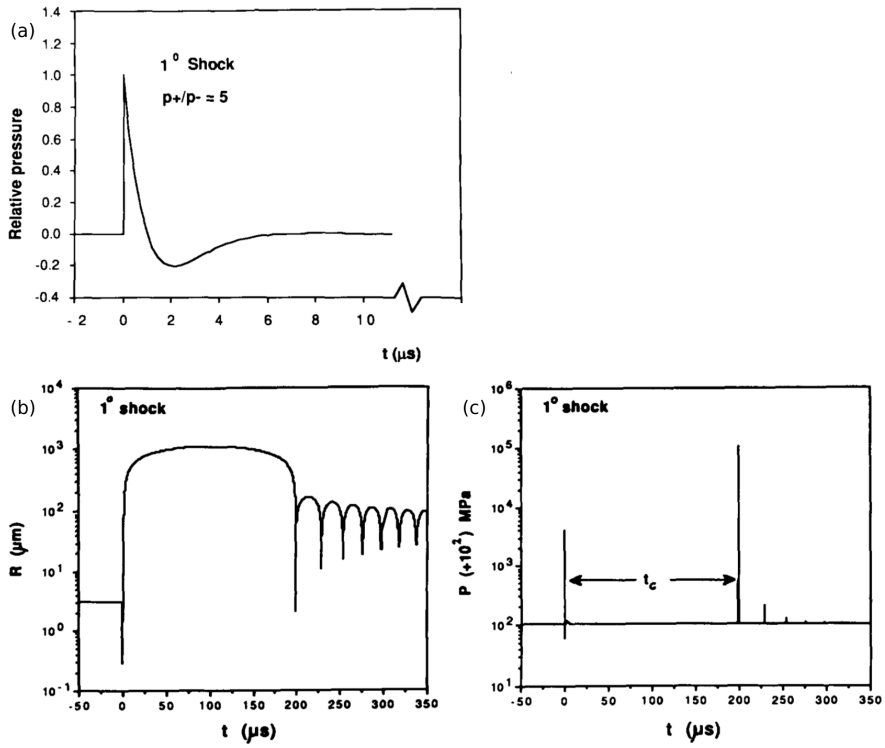

Figure 2.2: Predicted bubble dynamics under the influence of a lithotripsy pulse (Coleman et al., 1992), (a) a driving pressure wave of interest, the primary shock wave (1°) has a peak positive pressure of 50 MPa; (b) calculated radius vs time curve for an initial 3 µm radius bubble, (c) calculated radiated pressure at the bubble wall.

Cavitation has been strongly implicated in shock wave damage on tissue as the presence of microbubbles, which can enhance cavitation activities, was found to result in an increased amount of haemorrhage (Carstensen et al., 2000), whilst the interruption of cavitation process was reported to dramatically reduce tissue damage (Zhong and Zhou, 2001). In addition, it was suggested that the bubble expansion and collapse resulting in repetitive dilation of vessels could be the causes for damaging small capillaries (Zhong and Zhou, 2001; Zhong et al., 2001). Blood vessel invagination during bubble collapse may lead to high strains on the vessel wall and thus result in vessel rupture (Chen et al., 2011). Also liquid jetting emitted from bubble collapse was found to rupture small blood vessels (Chen et al., 2011). Similarly, a study using polystyrene microsphere to serve as cavitation nuclei found that cavitation alone can result in vessel rupture far away from the focal zone where acoustic pressures are minimal (peak negative pressure ∼0.15 MPa) (Matlaga et al., 2008).

An *in vitro* study also found that a single shock wave in combination with cavitation can cause cell membrane damage, cell detachment and cell death (Sonden et al., 2000). The extent of cell injury increased as the monolayers were exposed to higher level of cavitation (Sonden et al., 2000). Cavitation was also found to help increase the cell membrane permeability without killing the cell (Larina et al., 2005; Mehier-Humbert et al., 2005). These studies give insights into the delivery of therapeutic molecules such as oncolytic virus, genes and chemotherapeutic drugs. Improved delivery of target molecules into viable cells were consistently observed in the studies with the presence of ultrasound and microbubbles (Larina et al., 2005; Mehier-Humbert et al., 2005).

2.1.1.2 Direct mechanical forces

Cavitation, although strongly related to bioeffects on cells or tissues, may not be the primary mechanism responsible for tissue damage (McAteer et al., 2007).

In vitro studies have shown that, with the elimination of cavitation, suspended cells still showed about 10% of injury at high shock wave energy settings (Williams Jr et al., 1999). The cavitation was eliminated by using a pressure chamber where the static pressure was higher than the magnitude of the tensile phase of the shock waves. The results reported 97% more cell lysis than the control sample where cells were not exposed to shock waves. This indicates a noncavitational component in shock wave induced cell injury *in vitro*. The noncavitational mechanisms, although not well understood, were hypothesised as following: shear forces generated by shock waves passing through inhomogeneous medium, large tensile forces working on the cell membrane, and fluid streaming produced by the radiation pressure of shock waves on the cell sample vials.

In vivo studies have shown that tissue damage still occurs even in the absence of cavitation (Evan et al., 2002). In order to suppress cavitation, the study used a pressure release reflector which transposed the compressive and tensile phases of the lithotripter shock waves (see Figure 2.3). The pressure release reflector generated a negative pressure trough of slightly greater amplitude and slightly shorter duration, followed by the positive spike which cut short the cavitation bubble expansion collapse cycle and the resultant bubble collapse was less violent (Evan et al., 2002). The overall duration, frequency content and amplitude of compressive and tensile phases were almost preserved. It was reported that the kidney

damage was significantly reduced with the suppression of cavitation, however, the shock wave generated with the pressure release reflector still showed haemorrhage of vessels near the papilla tip (a region most sensitive to shock waves (McAteer et al., 2007)) and disruption of kidney function (e.g., glomerular filtration rate) (Evan et al., 2002). This suggests that mechanical stresses may be responsible for tissue damage.

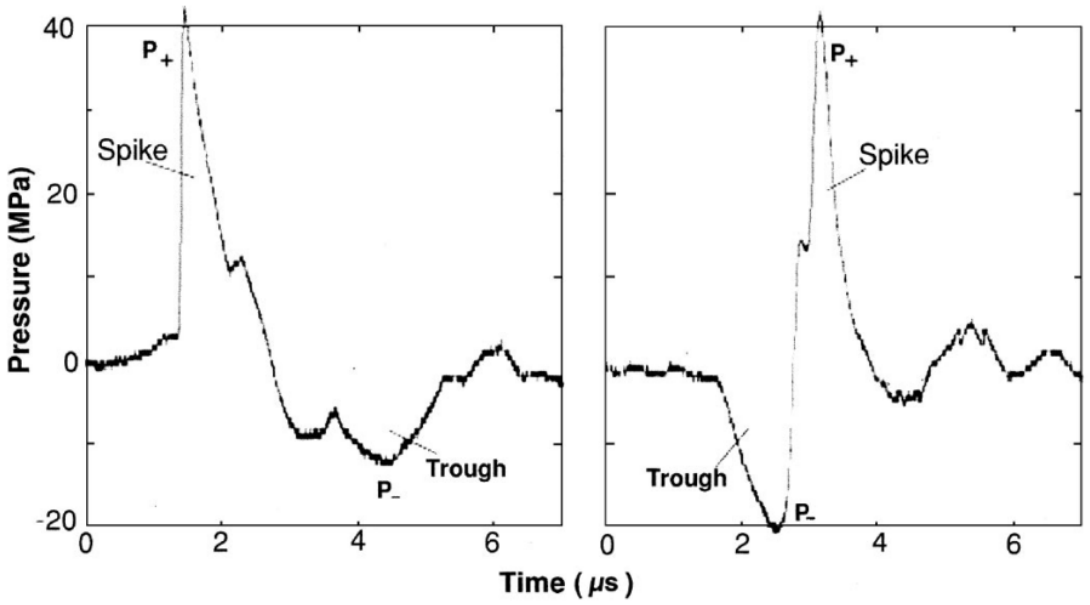

Figure 2.3: Lithotripter shock wave profiles (Evan et al., 2002), (a) original lithotripter shock wave, (b) shock wave pressure waveforms with a pressure release reflector.

A numerical study also suggested that even if the shear deformation resulting from a single shock wave pulse was ∼0.1%, an accumulation of 15% of shear strain can be achieved after 1000 shock waves and such strain is sufficient to cause damage in the absence of cavitation (Freund et al., 2007). Near the papilla tip, the large interstitial volume (∼40%) gave the tissue a relaxation time comparable to clinical shock wave delivery rate (1Hz), thus allowing for the accumulation of shear stress. On the other hand, away from the papilla tip, as the interstitial volume reduced (<20%), the tissue may have relaxed before the next shock wave pulse was delivered, and consequently the resultant strain will not accumulate (Freund et al., 2007).

In summary, acoustic cavitation plays an important role in acoustic bioeffects

on cells such as cell death and enhanced permeability. This is related to the cavity bubble expansion and the microjetting and secondary shock waves associated with cavity bubbles collapse. On the other hand, it is also found that noncavitational forces such as tension and shear stress may be the primary mechanism for those bioeffects. However, a clear conclusion on the contribution of cavitation or noncavitation activities for certain bioeffects are not drawn.

2.2 Cell structure

Cell is the smallest unit that can perform all functions of life. All eukaryotic cells share the same basic layout in which a bilipid layered membrane is filled with cytoplasm providing environment for a variety of organelles to perform their specialised tasks (Allen and Cowling, 2011).

The cell membrane is a very thin but extremely tough and flexible layer which provides a barrier to the external environment. At the same time, it allows for the constant exchange of molecules between the cell and its surroundings through passive or active processes. There are around 500 different membrane lipids which surround and anchor various proteins to form channels and control the continuous molecule flow across them (Allen and Cowling, 2011).

Cytoplasm is made of cytoskeletons bathing in a fluid environment called cytosol, which helps to maintain structural integrity, mechanical stability and protect the organelles from external forces. Also, it is responsible for cell's motility and migration abilities (Steinhauser and Schmidt, 2014; Allen and Cowling, 2011). There are three major components in the cytoskeletal network: microfilament or actin filament, intermediate filament and microtubules. They differ in size, structure and their roles in mechanical properties.

Actin filaments are the thinest filamentous proteins, around 6-8nm in diameter. The interactions between actin filaments and myosin motors supply the motile force involved in cell division and cell movement (Allen and Cowling, 2011; Steinhauser and Schmidt, 2014; Jonas et al., 2011). Microtubules have a hollow tube structure with 14nm inner and 25nm outer diameter. Cytoplasmic microtubules radiate outwards from the centre. Microtubules are involved in cell division and migration (Allen and Cowling, 2011; Akhshi et al., 2014). Intermediate filaments are 10nm in diameter which is intermediate between actin filaments

and microtubules. They permeate the entire cell and provide it with mechanical strength. Cells in tissue are joined to their neighbours in the cell-cell junctions where the intermediate filaments are anchored to the cell plasma membrane.

Within the cytoplasm, the three groups of filaments connect with each other through protein bridges like integrins and plakins to resist the external forces (Allen and Cowling, 2011; Akhshi et al., 2014). Studies have shown that actin filaments and intermediate filaments provide resistance to tension (acting like springs) while microtubules are resistant to compression (acting like rods) (Suresh, 2007; Ji and Bao, 2011).

The cell nucleus is a highly specialised organelle which stores the cell's hereditary materials (DNA), and it also coordinates the cell's activities including growth, protein synthesis, cell reproduction and intermediary metabolism (Tripathi and Prasanth, 2011). Research studies have found that the nuclear to cellular volume remains constant throughout cell cycle and the nucleus exhibits higher stiffness than the cytoplasm (Webster et al., 2009; Gregory, 2005; Jérusalem and Dao, 2012). Therefore, cells have been studied as a homogeneous entity (Schmid-Schonbein et al., 1981; Sato et al., 1990), with a differentiated cell membrane (Mishra et al., 2014) or with differentiated cell components (cell nucleus, cytoplasm and membrane) (Jérusalem and Dao, 2012).

2.3 Cell interaction with acoustic waves

Several studies have been focussing on the study of acoustic effects on single cells or sub-cellular components in order to understand the underlying mechanisms of drug delivery and cell or tissue injury. Both experimental and computational approaches are summarised here.

2.3.1 Experimental studies

A recent study presented the interaction of a single HeLa cell with the tandem bubble-induced jetting flow (Yuan et al., 2015). The study captured the tandem bubble formation and collapse and their influence on the single cell deformation at a controllable standoff distance. The bubbles were generated by illuminating two laser pulses with time delay on a pair of gold dots. The time delay produced phase difference between the two bubbles which then formed a highly localised

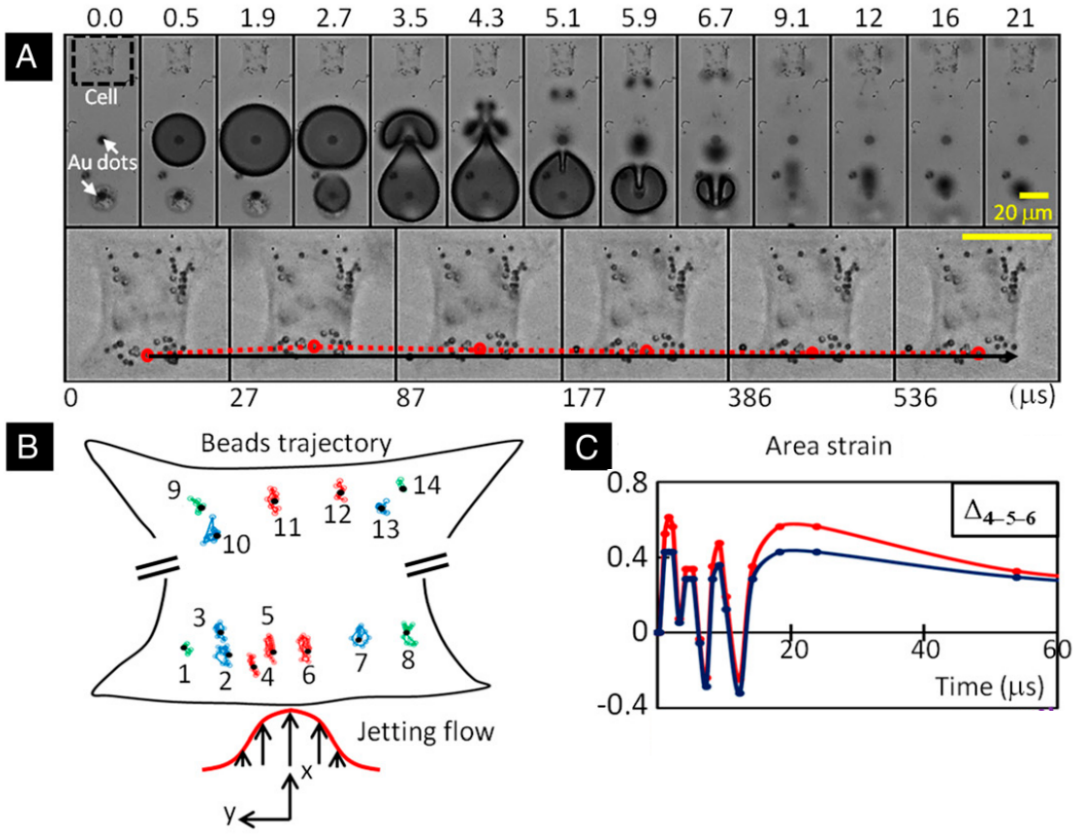

Figure 2.4: Cell membrane deformation in response to tandem bubble interaction (Yuan et al., 2015), (A) Tandem bubble cell interaction at standoff distance = 40 µm, (B) Trajectory of 14 individual beads (1 µm) identified on the membrane of the target cell with the localised jet flow presented, (C) The area strains, calculated based on principal strain derived from the deformation of the triad (in red color) or the geometric area change of the triad (in blue color) defined by beads 4, 5 and 6.

jet (the jet flow width was on the order of 10 µm) towards the cell. Figure 2.4 shows the cell deformation in response to the jet flow created by the tandem bubbles at standoff distance of 40 µm. The local area strain was reported as 60% in response to the jet (Figure 2.4C). The measurement was based on the area change of adjacent beads (bead 4, 5, 6 in Figure 2.4B) at the leading edge of the cell. In some cases (standoff distance <20 µm), the local area strain of the leading edge can exceed 100% (Yuan et al., 2015). Furthermore, the tandem bubbles resulted in a jetting flow with vortex formation in a proximity-dependant manner which was not observed in the single bubble case in which the acoustic influence is more global on cells. This vortex flow was found to prolong the jetting

flow-induced stretch on the cell membrane, which was correlated to the resultant bioeffects such as cell necrosis and repairable poration.

Other studies have also found that the microjetting or secondary shock waves generated through single bubble collapse during acoustic waves can result in sonoporation effect on the adjacent cell (Fan et al., 2012; Vlaisavljevich et al., 2016). An average pore size of around 16 nm (Fan et al., 2012) was found in repairable poration, based on the membrane current change and an electro-diffusion model (Fan et al., 2012). In the context of histotripsy, extremely large transient area strain (>150%) adjacent to the bubble cloud was reported (Vlaisavljevich et al., 2016).

The bioeffects on cells were also explained at the sub-cellular level with the hypothesis of intramembrane cavitation under acoustic waves (Krasovitski et al., 2011). The study used a model membrane composing of two monolayer leaflets to study the membrane behaviour under acoustic wave exposure. The results of the model membrane in water found that at negative pressure (-0.7 MPa), the two leaflets of the cell membrane were pulled apart overcoming the molecular traction forces, which resulted in large areal strain (∼30%) in the pulsating leaflet. This process was reversed under the positive phase of the acoustic pressure, i.e., the two leaflets were forced to approach each other during compression. The maximum areal strain and the deviation between the two leaflets were hypothesised to be related to pore formation which is essential for bioeffects on cells such as sonoporation and cell death. Moreover, the tension on the membrane leaflets may activate or even damage the membrane protein which may then cause membrane rupture or pore formation (see Figure 2.5). The study also found that the maximum areal strain differed with various ultrasound exposure parameters, surrounding mechanical properties, proximity to free surfaces and the presence of extracellular gas bubbles.

In summary, these studies have shown the possible mechanisms of single cell interactions with acoustic waves, mainly in the context of cavity bubble dynamics and jetting flow or secondary shock waves generated by cavitation. However, the effects of the incident acoustic waves on the single cell response were not studied.

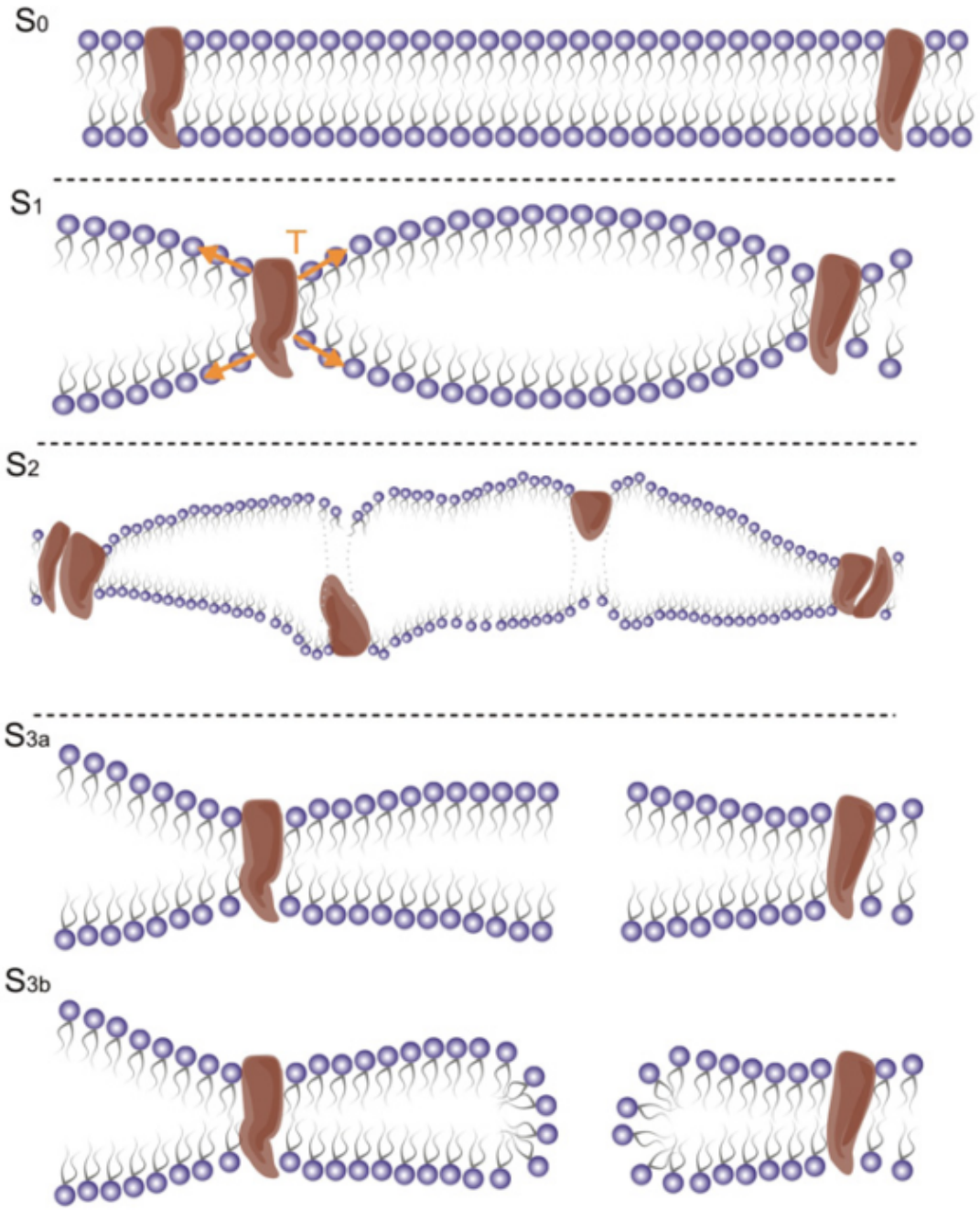

Figure 2.5: Schematics of membrane interaction with ultrasound (Krasovitski et al., 2011), (S0) reference state of the bilayer membrane, (S1) Slightly stretched leaflets might firstly activate membrane proteins, (S2) the growing tension in the leaflets may damage the membrane protein, and cause different bioeffects (S3a) membrane rupture or (S3b) pore formation.

2.3.2 Continuum mechanics studies

An increasing number of studies have been focussing on understanding the biological changes of tissues and cells under mechanical stimuli using computational and mathematical methods at multiple scales. A review of computational models and material properties related to our research of interest are presented in this section.

2.3.2.1 Overview of continuum models

Continuum mechanical models for living cells can be generally categorised as liquid drop models and solid models (Lim et al., 2006). The liquid drop model was firstly developed to model cells as Newtonian viscous fluid. However, experimental data found that the equilibrium of cells is achieved after a certain amount of loading, indicating a solid framework for the cell's material properties. It was also found that the cell cytoplasm behaves more like a solid than fluid due to the embedded cytoskeleton. Therefore, cells are more commonly described by solid models (i.e., elastic or viscoelastic models).

Based on the conservation of linear momentum, the continuum system is described as:

$$\nabla \mathbf{P} + \rho_0 \mathbf{b} = \rho_0 \ddot{\mathbf{x}}, \qquad \forall \mathbf{X} \in B_0 \tag{2.1}$$

where $\mathbf{P}$ is the first Piola-Kirchhoff stress tensor which relates force in the deformed configuration to area in the reference (undeformed) configuration, B_0. $\mathbf{b}$ is the body force vector per unit mass, $\mathbf{X}$ and $\mathbf{x}$ are the point coordinates vector in the reference and deformed configuration respectively. Alternative stress measures that are typically used are:

$$\begin{cases} \text{the second Piola-Kirchhoff stress} & \mathbf{S} = \mathbf{F}^{-1}\mathbf{P} \\ \text{the Cauchy stress} & \boldsymbol{\sigma} = J^{-1}\mathbf{P}\mathbf{F}^T \\ \text{the Kirchhoff stress} & \boldsymbol{\tau} = \mathbf{P}\mathbf{F}^T \end{cases} \tag{2.2}$$

The second Piola-Kirchhoff stress is fully defined in the reference configuration while the Cauchy stress is fully defined in the deformed configuration. The Kirchhoff stress, on the other hand, has little physical significance but brings convenience to mathematical and numerical operations. Here, $\mathbf{F} = \frac{\partial \mathbf{x}}{\partial \mathbf{X}}$ is the deformation gradient and $J = det\,(\mathbf{F})$ is the Jacobian which is the volumetric change with respect to the reference configuration.

The determination of the stress measure is also related to the deformation of the material of interest through its constitutive material law. Viscoelastic and hyperelastic constitutive frameworks are commonly applied to model cells and soft tissues. In general, for the case of viscoelasticity, the second Piola-Kirchhoff stress $\mathbf{S}$ can be defined by a combination of the initial elastic response $\mathbf{S}^\circ$ and viscous response $\mathbf{S}_{vis}$ (Simo and Hughes, 2008):

$$\mathbf{S} = \mathbf{S}^\circ + \mathbf{S}_{vis} \tag{2.3}$$

The initial elastic stress, $\mathbf{S}^\circ$, can be derived from an elastic strain energy W through the right Cauchy-Green tensor $\mathbf{C} = \mathbf{F}^T\mathbf{F}$ (Holzapfel, 2000), which can be decomposed additively into its volumetric and isochoric (deviatoric) components (Holzapfel, 2000):

$$\begin{cases} W(\mathbf{C}) = U(J) + \bar{W}(\bar{\mathbf{C}}) \\ \mathbf{S}^\circ = 2\dfrac{\partial W(\mathbf{C})}{\partial \mathbf{C}} = \mathbf{S}^\circ_{vol} + \mathbf{S}^\circ_{iso} \end{cases} \tag{2.4}$$

where U and $\bar{W}$ are the volumetric and deviatoric contributions to the stored energy function, and $\bar{\mathbf{C}}$ is the deviatoric part of the right Cauchy-Green tensor. Hence, the initial elastic stress can be represented as:

$$\mathbf{S}^\circ = \underbrace{JU'(J)\mathbf{C}^{-1}}_{\mathbf{S}^\circ_{vol}} + \underbrace{J^{-\frac{2}{3}}\mathrm{DEV}\left[2\frac{\partial W(\bar{\mathbf{C}})}{\partial \bar{\mathbf{C}}}\right]}_{\mathbf{S}^\circ_{iso}} \tag{2.5}$$

where the operator "DEV" provides correct notion of "deviatoric" stress tensor in terms of $\mathbf{C}$ (Simo and Hughes, 2008):

$$\mathrm{DEV}\left[2\frac{\partial W(\bar{\mathbf{C}})}{\partial \bar{\mathbf{C}}}\right] = 2\frac{\partial W(\bar{\mathbf{C}})}{\partial \bar{\mathbf{C}}} - \frac{1}{3}\left[2\frac{\partial W(\bar{\mathbf{C}})}{\partial \bar{\mathbf{C}}} : \mathbf{C}\right]\mathbf{C}^{-1} \tag{2.6}$$

Note that Equation (2.5) also describes the elastic response of a hyperelastic material where the stress-strain relationship is studied in a non-linear regime.

The volumetric stress, $\mathbf{S}^\circ_{vol}$ can also be represented through pressure, p, in the principal directions:

$$\mathbf{S}^\circ_{vol} = J(p\mathbf{I})\mathbf{C}^{-1} \tag{2.7}$$

where $\mathbf{I}$ is the identity matrix.

The elastic strain energy and the evolution of viscous effects differ from one study to another in terms of stress measure and viscoelasticity frameworks. Further discussion will be presented in the following sections.

2.3.2.2 Computational studies

Several numerical works using continuum solid models have focussed on the interactions between cells and acoustic waves (Miller et al., 2010; Jérusalem and Dao, 2012; Mishra et al., 2014). The material models involved in these studies are the detailed descriptions of the general material frameworks illustrated in Equations (2.3)-(2.7).

The detachment process of cells to substrates when subject to laser-induced stress waves was investigated (Miller et al., 2010). The cell was modelled with differentiated nucleus, cytoplasm and plasma membrane. Both nucleus and cytoplasm were described by the same constitutive equations, either linear elasticity ($\bar{W} = \frac{1}{2}\mu e^2$) or the first-order generalised Maxwell viscoelasticity (see Figure 2.6) where the long term modulus, μ^∞ and instantaneous shear modulus, $\mu_0 = \mu^\infty + \mu_1$, are included.

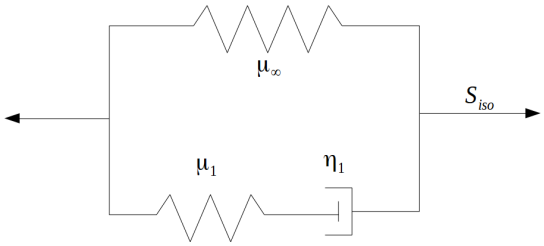

Figure 2.6: Schematic for the first-order generalised Maxwell model where springs account for elastic response while the dashpot describes the viscous effects; μ^∞ is the long term shear modulus, and μ_1 and η_i are the shear modulus and viscosity accounts for the viscoelastic behaviour.

Similar to Equations 2.3-2.4, The resultant viscoelastic stress in a Kirchhoff notation, $\boldsymbol{\tau}$, is measured by its viscous evolution $\boldsymbol{\tau}_{vis}$ and the instantaneous shear stress tensor $\boldsymbol{\tau}^\circ$ obtained from the derivative of the strain energy W:

$$\begin{cases} \mathbf{S}^\circ = 2\dfrac{\partial W(\mathbf{C})}{\partial \mathbf{C}} \\ \boldsymbol{\tau}^\circ = \mathbf{F}\mathbf{S}^\circ\mathbf{F}^T = JU'(J)\mathbf{I} + \mathrm{dev}[\bar{\mathbf{F}}\partial_{\bar{\mathbf{C}}}\bar{W}(\bar{\mathbf{C}})\bar{\mathbf{F}}^T] \\ \boldsymbol{\tau} = \boldsymbol{\tau}^\circ + \underbrace{\mathrm{dev}\displaystyle\int_0^t \dot{g_R}(s)\bar{\mathbf{F}}_t^{-1}(t-s)\boldsymbol{\tau}^\circ(t-s)\bar{\mathbf{F}}_t^{-T}(t-s)ds}_{\boldsymbol{\tau}_{vis}} \end{cases} \tag{2.8}$$

where "dev" is the deviator operator in terms of identity matrix $\mathbf{I}$: $\mathrm{dev}[\bullet] = (\bullet) - \frac{1}{3}[(\bullet) : \mathbf{I}]\mathbf{I}$, $\bar{W}$ is the deviatoric strain energy from the linear elasticity,

$U = \frac{1}{2}K[\frac{1}{2}(J^2-1) - \ln J]$ is the volumetric strain energy, J is the Jacobian of the deformation gradient tensor, g_R(t) is the dimensionless shear relaxation modulus which can be expanded by Prony series to link to the short- and long- term shear moduli and viscosity and $\bar{\mathbf{F}}_t(t-s)$ is the isochoric part of the relative deformation gradient $\mathbf{F}_t(t-s) = \frac{\partial \mathbf{x}(t-s)}{\partial \mathbf{x}(t)}$:

$$g_R(t) = 1 - \sum_{i=1}^{N} g_i(1 - e^{-t/\tau_i}) \tag{2.9}$$

where g_i and τ_i are the Prony series coefficients which can be converted from shear modulus μ_i and viscosity η.

$$\begin{cases} g_i = \dfrac{\mu_i}{\mu_0} \\ \tau_i = \dfrac{\eta_i}{\mu_i} \end{cases} \tag{2.10}$$

The shear modulus of the nucleus was taken to be four times stiffer than that of the cytoplasm (Miller et al., 2010). The cell membrane was chosen to be 6nm thick and described by the linear elasticity. The volumetric response was modelled by an elastic bulk material behaviour, where pressure p is proportional to the ratio of current volume to initial volume $\frac{V_i}{V_0}$, i.e., $p = -Kln\frac{V_i}{V_0}$.

The simulation results showed that the cell detachment under stress waves was caused by the large strain at the interface due to the cell's tendency to flatten and elongate during the rapid movement of the substrate, driven by the pressure waves. It was also found that the detachment behaviour was similar in both elastic and viscoelastic models as the characteristic creep time of the viscoelastic material law was many orders of magnitude larger than the duration time of the applied stress wave.

A fluid-structure continuum model was presented to analyse the response of a neuron cell when subject to a blast wave (Jérusalem and Dao, 2012). The cell was modelled as attached to a substrate with differentiated nucleus, cytoplasm and membrane compartments. The deviatoric response of the model was described by a visco-hyperelastic constitutive equation using the first-order generalised Maxwell model (Equations(2.8)). The elastic strain energy, W, used in this study takes into account of large deformation using Neo-Hookean hyperelasticity, as opposed to the linear elasticity in the previous study by (Miller et al., 2010).

$$W = \underbrace{C_1(\bar{I}_1 - 3)}_{\bar{W}(\bar{\mathbf{C}})} + \underbrace{D_1(J-1)^2}_{U(J)} \tag{2.11}$$

where C_1 and D_1 are the Neo-Hookean material coefficients associated with shear modulus and bulk modulus respectively, $\bar{I}_1$ is the deviatoric part of the first invariant of the deviatoric right Cauchy-Green tensor.

The volumetric response, on the other hand, was modelled by a Mie-Grüneisen/Hugoniot Equation of State (EoS) which links pressure p to the change of density based on conservation laws of mass, momentum and energy:

$$p = p_H(1 - \frac{\Gamma_0}{2}(1 - \frac{\rho_0}{\rho})) + \Gamma_0 \rho_0 E \tag{2.12}$$

where p_H is the pressure behind the shock front, E is the internal energy per unit mass and Γ_0 denotes the Grüneisen parameter in the initial state.

The material properties of the cell components were calibrated against nanoindentation test results. The simulation results found that whereas pressure affects the cell homogeneously, shearing effects were mainly localised at the cellular and nuclear membranes, indicating that damage in the cell may be caused by loss of membranes' integrity.

A numerical model on single blood cell deformation under acoustic radiation forces was studied (Mishra et al., 2014). The cell was modelled with a thin shell structure accounting for the red blood cell membrane, and an artificial volume dependent pressure was also used on the membrane to constrain the cell volume within 0.5% change. The material law was governed by a linear elasticity for the membrane. A linear acoustic model linking the change of pressure to the first-order change of density ($\Delta P = K\left(\frac{\Delta\rho}{\rho_0}\right)$) was also used to estimate the acoustic radiation stresses acting on the cell membrane. The results, matched with experimental observations, showed that the deformation of the cell increased with the increase of acoustic pressure amplitude, and the maximum aspect ratio of 1.35 was found in the deformed blood cell compared to the initial value of 0.98 in the reference state. The deformation was found to be the result of variations in an acoustic force that is directed outwards at all points on the cell membrane (Mishra et al., 2014).

In summary, numerical studies have been implemented to analyse cell response to acoustic waves and have shown the stress and strain evolution during the interaction process. However, the mechanical properties used in the models are not correctly calibrated against cell experiments under ultra-high strain rate loading which is important for modelling the effects of shock waves.

2.3.3 Summary of relevant material properties

Since the work mainly focuses on kidney for its application in both lithotripsy and cancer therapy, the material properties summarised here are targeting such organ. However, in general the cell constitution in healthy normal cells are similar except for some difference in cytoplasmic filaments related to the tissue type and embryonic origin Allen and Cowling (2011); Steinhauser and Schmidt (2014), therefore the cell mechanical properties may be applied to other cell lines.

The material properties of tissues and cells are essential inputs for simulations in order to mimic *in vitro* or *in vivo* scenarios. They can be obtained from experiments such as uniaxial tension and compression tests on tissues, micropipette aspiration, microplate manipulation and atomic force microscopy (AFM) on individual cells (Weinberg and Ortiz, 2009; S. Nicolle, 2010; Umale et al., 2012; Egorov et al., 2008; Snedeker et al., 2005; Amador et al., 2009; Nasseri et al., 2002). In general, material properties are obtained by optimising material parameters in the numerical model, until the simulation results fit into the response or phenomena observed in mechanical experiments. It is important to note that these experiments generally use mechanical stimuli with low to moderate strain rate (less than 100/s), therefore the values may not be accurate for modelling cell response under shock waves (strain rate $>10^4$/s).

At tissue level, uniaxial tension and compression tests are commonly used for measuring material elasticity (Weinberg and Ortiz, 2009; Umale et al., 2012; Snedeker et al., 2005). The tests are normally conducted in quasi-static conditions and using multiple strains to calibrate the elastic modulus of the specimen at linear and nonlinear regimes. Oscillation tests (S. Nicolle, 2010; Nasseri et al., 2002), on the other hand, sweep over a range of frequency domain with a small deformation ($\sim$0.1%) to assess the material response in longer or shorter timescales in order to quantify the viscous effects on the material response. Magnetic Resonance Elastography (MRE) (Bensamoun et al., 2011), Multifrequency Magnetic

Resonance Elastography (MMRE) (Leclerc et al., 2012) and Shearwave Dispersion Ultrasound Vibrometry (SDUV) (Amador et al., 2009) are all based on image processing of shear wave propagation in the material at a certain frequency. The shear wave properties such as wave speed and phase change reveal the viscoelastic material characteristics. Reviewed material properties of kidney tissue are summarised in Table 2.1. Note that almost all the studies assume that the materials are incompressible, hence the shear modulus is assumed to be 1/3 of the elastic modulus (Poisson's ratio is $\sim$0.5).

Table 2.1: Basic biomechanical parameters derived from kidney tissue compartments, including elastic modulus, tissue density, shear modulus,and viscosity. The summary is illustrated in Figure 2.7.

Kidney Tissue			
Source	Methods	Parameter	Values
Weinberg and Ortiz (2009)	uniaxial tension	Elastic modulus: Cortex	1.2 MPa
	extrapolation	Elastic modulus: Medulla	1 MPa
		Elastic modulus: Pyramid	0.55 MPa
		Density	1050 kg/m^3
		Bulk modulus	2500 MPa
S. Nicolle (2010)	oscillation test	Shear modulus	0.315 $\pm$ 0.142 kPa
	(0.1 - 4 Hz)	viscosity	3.5 $\pm$ 3 Pa.s
Umale et al. (2012)	uniaxial tension	Elastic modulus: Capsule (Low strain)	7.1 $\pm$ 3.75 MPa
	0.002 /s	Elastic modulus: Capsule (High strain)	16.35 $\pm$ 4.52 MPa
	uniaxial compression	Elastic modulus: Cortex (Low strain)	15 $\pm$ 7.2 kPa
	0.007 /s	Elastic modulus: Cortex (High strain)	1.16 $\pm$ 0.1 MPa
Egorov et al. (2008)	tissue elastomtry	Elastic modulus: Smooth surface	5.9 $\pm$ 0.7 kPa
	50 - 100]lm/s	Elastic modulus: Cut surface	6.3 $\pm$ 0.7 kPa
Snedeker et al. (2005)	quasi-static tension	Elastic modulus: Capsule (Low strain)	14.7 $\pm$ 5.5 MPa
	0.005 /s	Elastic modulus: Capsule (High strain)	35.9 $\pm$ 13.3 MPa
Amador et al. (2009)	SDUV	Shear modulus: Cortex (50 - 500 Hz)	1.7 - 2.3 kPa
	50 - 550 Hz	Viscosity: Cortex	1.8 - 2.2 Pa.s
Nasseri et al. (2002)	oscillation test	Viscosity, strain = 0.004	20 kPa.s (0.01 Hz)- 200 Pa.s (10 Hz)
	0.01 - 10 Hz	Viscosity, strain = 0.01	20 kPa.s (0.01 Hz) - 90 Pa.s (10 Hz)
		Viscosity, strain = 0.02	20 kPa.s (0.01 Hz)- 70 Pa.s (10 Hz)
Bensamoun et al. (2011)	MRE	Shear modulus	4.12 $\pm$ 0.24 kPa
	60 Hz		
Leclerc et al. (2012)	MMRE	Shear modulus	3.45 kPa
	60 Hz	Viscosity	6.17 Pa.s

Figure 2.7 shows the majority range of shear moduli and viscosities of the kidney tissue summarised from the literature (for visualisation purpose some data are excluded from the graph but will be discussed here). Note that the material properties of kidney capsule are excluded as they are not in the region of interest and their mechanical stiffness is significantly larger (three orders of magnitude)

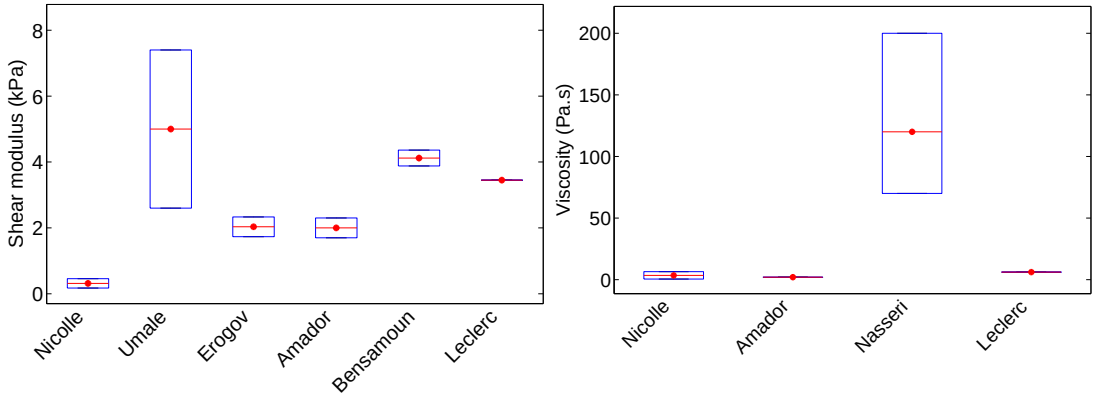

Figure 2.7: (A) range of the shear modulus values for kidney tissues from the literature (B) range of the viscosity values for kidney tissues from the literature, see Table 2.1.

than the rest of the kidney. The differences between the results may be caused by discrepancies in the tested kidney regions, biological variability and the experimental setup, including measurement devices and the loading strain and strain rate. The figure indicates that the shear modulus of the kidney tissue mainly ranges from ∼2 kPa to ∼4 kPa and the kidney viscosity varies from ∼2 Pa.s to ∼7 Pa.s. Exceptions (not shown in the figure) are found in the value range for both shear modulus and viscosity, e.g., the shear modulus of kidney tissue was reported to be around 300-400 kPa under very large strain tests (45%) (Umale et al., 2012), and a 20 kPa.s viscosity was found in the kidney cortex at 0.01Hz sweep frequency when the applied strain exceeded the linear viscoelastic limit (0.2%) (Nasseri et al., 2002). Measurements using relatively high strain rates and small strains are more relevant for our work as shock waves result in small deformation (∼1%) with very high strain rate (Jérusalem and Dao, 2012).

The material properties of cells and cell components from various cell lines are summarised in Table 2.2. At the cellular or subcellular levels, mechanical tests are often performed using micro- or nano-scale mechanical stimuli. AFM, nano- or micro-indenters probe the material with different strain rates and measure the relationship between force and displacement (Ebert et al., 2004; Rebelo et al., 2013; Qiuquan et al., 2012). Micropipette aspiration or recovery tests use a micropipette with a diameter of 2-4 µm to apply a gentle controllable suction and release on cells. The cell deformation is tracked with high speed imaging (McGarry and Prendergast, 2004; Guilak et al., 2000; Houchmandzadeh et al., 1997; Kamm et al., 2000; Evans and Yeung, 1989; Lim et al., 2006). Optical

Table 2.2: Basic biomechanical parameters of different cell components. Different cell lines were used. The summary is illustrated in Figures 2.8 and 2.9.

Cell

Source	Method	Parameter	Values	Cell Type
Ebert et al. (2004)	AFM	Elastic modulus	10 - 70 kPa	Hamster kidney cell
Rebelo et al. (2013)	AFM	Median elastic modulus	9.38 kPa	Human kidney cell lines
		Median viscosity	69.6 Pa.s	
Qiuquan et al. (2012)	AFM	Elasticity: on Polystyrene substrate	8.71 $\pm$ 0.9 kPa	Human aortic endothelial cells
		Elasticity: on Matrigel substrate	7.62 $\pm$ 0.81 kPa	

Membrane

Source	Method	Parameter	Values	Cell Type
Dao et al. (2003)	optical tweezers	Elastic modulus	$\sim$300 Pa	Blood red cells
McGarry and Prendergast (2004)	Micropipette aspiration	Elastic modulus	1000 Pa	Airway epithelial cells

Nucleus

Source	Method	Parameter	Values	Cell Type
Guilak et al. (2000)	Micropipette aspiration	Elastic modulus	$\sim$1 kPa	Chondrocytes
		Viscosity	$\sim$500 Pa.s	
Houchmandzadeh et al. (1997)	Micropipette aspiration	Elastic modulus	1 - 5 kPa	lung cells
Tseng et al. (2004)	Particle nanotracking	Viscosity	52 Pa.s	Fibroblasts
		shear modulus	18 Pa	

Cytoplasm

Source	Method	Parameter	Values	Cell Type
Kamm et al. (2000)	Micropipette aspiration	Elastic modulus	100 Pa	Airway epithelial cells
Karcher et al. (2003)	Magnetocytometry	Elastic modulus	$\sim$1000 Pa	Fibroblasts
Evans and Yeung (1989)	Micropipette aspiration	Viscosity	210 $\pm$ 100 Pa.s	Granulocytes
Lim et al. (2006)	Micropipette aspiration	Viscosity	135 $\pm$ 54 Pa.s	Neutrophils
Tran-Son-Tay et al. (1991)	Micropipette recovery	Viscosity	151.7 $\pm$ 19.8 Pa.s	Neutrophils

tweezers use a similar principle in which cells are stretched using two microbeads controlled by laser beams, and the cell deformation is recorded by high speed imaging (Dao et al., 2003). Finally, particle nanotracking or magnetocytometry use microbeads injected or attached to cell components to assess their deformation under shear flow (Tseng et al., 2004; Karcher et al., 2003).

Figures 2.8 and 2.9 respectively present the elastic moduli and viscosity values of different cells and cellular components. The elastic modulus of the whole cell is in the order of 10 kPa while the subcellular components exhibit 10 times lower stiffness. The membrane elasticity is found to be between 300 Pa to 1 kPa,

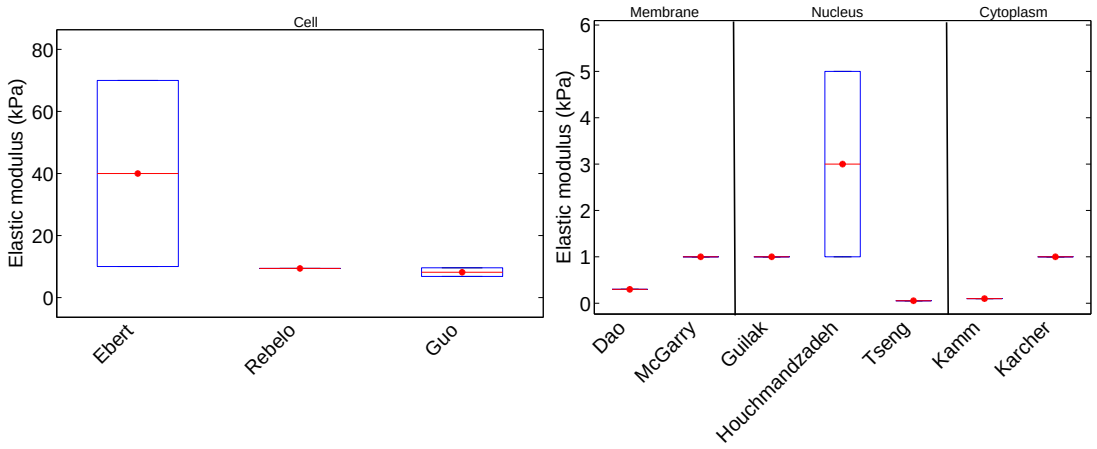

Figure 2.8: Reviewed elastic moduli of different cell components, see Table 2.2.

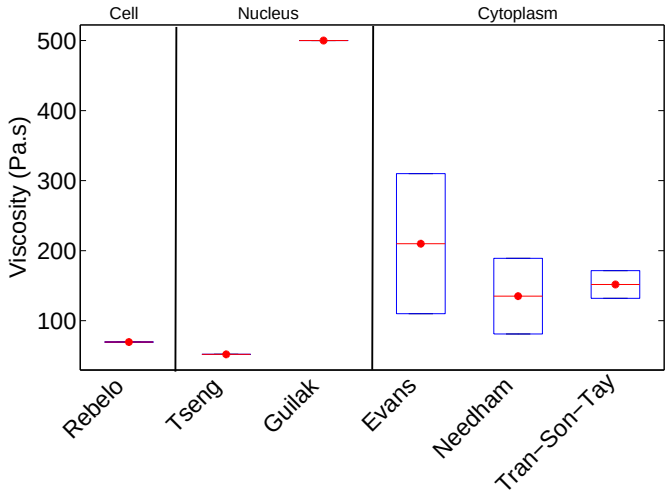

Figure 2.9: Reviewed viscosity values of cell nucleus and cytoplasm, see Table 2.2.

mainly depending on the tested cell lines (or cell granularity). The cell nucleus has been reported to be 3-4 times stiffer and twice viscous as the cytoplasm (Guilak et al., 2000). Therefore, an acceptable range of elasticity for the nucleus lies between 1 kPa and 5 kPa with an exception of 54 Pa found in fibroblast cells measured by tracking nanospheres injected to their nuclei (Tseng et al., 2004). The large difference reported here could be caused by different cell lines used in the measurements, whether or not the nucleus is isolated from the cell, and the magnitude of applied force (picoNewton vs. nanoNewton). The cytoplasm was reported to be much softer than the nucleus, with an elastic modulus between 100 Pa and 250 Pa, although an elastic modulus around 1 kPa was found in a

magnetic trapping experiment (Karcher et al., 2003). Finally, as little literature data available, the viscosity of the nucleus and cytoplasm were reported to be ranging from 52 Pa.s to 500 Pa.s, and 81 Pa.s to 310 Pa.s, respectively.

CHAPTER 3

Experimental methods

An ultra-high speed imaging experiment which visualises cell deformation under shock waves is presented. A clinical shock wave transducer is used to generate shock waves for the experiment. The dynamics of cell response are captured by an ultra-high speed imaging system with high power laser providing sufficient lighting for the imaging procedure. A hydrophone is utilised to measure pressures in the sample. Image analysis techniques are used to analyse the experimental results of cell deformation under shock waves in order to build simulations that are matched to the experimental observations. Imaging and segmentation variability are also analysed.

3.1 Experimental setup

The experimental setup is described in Figure 3.1, mainly consists of a tissue sample with individual cells embedded in, a shock wave source with a needle hydrophone for alignment and an ultra-high speed imaging system.

3.1.1 Cell culture and tissue phantom preparation

Three cell lines from the same origin (human kidney epithelium) were used in the experiment in order to compare the mechanical difference between cancer cells and their noncancerous counterparts. Human renal epithelial cells (HRE, Lonza) are normal and healthy primary cells isolated from human renal cortex and glomerular, which represented the normal healthy kidney cells in the experiment. The invasive cancer cells used in the experiment were CAKI-2 (ATCC HTB-47)

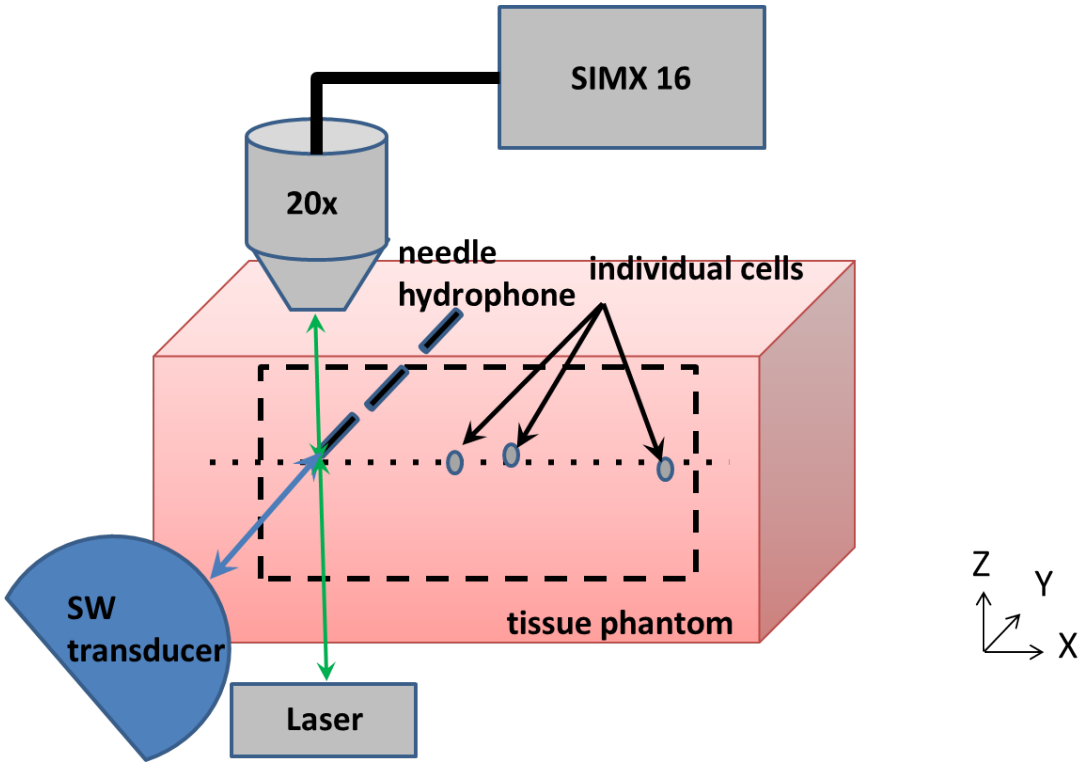

Figure 3.1: Overview of the experimental setup containing a SIMX 16 ultra-high speed camera, a 20× microscopic objective, a laser source, a shock wave transducer, a needle hydrophone and a cell-agarose tissue phantom.

which is also an epithelial cell line established from a clear cell carcinoma of the human kidney. The third cell line used in the experiment was HK-2 (ATCC CRL-2190) cell line which is a HPV-16 transformed immortalised human kidney epithelial cell line.

The three cell lines were routinely maintained in their corresponding culture medium in a cell culture incubator: BulletKit human renal cell system (Lonza) was used for HRE cells, McCoy's 5a Medium Modified (ATCC) and DMEM (Life Technology) both supplemented with 10% FBS and 1% antibiotic/antimycotic solution were used for CAKI-2 and HK-2 cells respectively.

The day before the experiment, cells from each cell line were trypsinized and resuspended in culture medium to a density of $\sim 0.1 \times 10^6$ cells/mL before being injected into a tissue-mimicking phantom.

Three different tissue-mimicking phantoms were made for the three cell lines with the same consistency. Each phantom consisted of 672 mg purified

agarose powder (UltraPure Agarose, Invitrogen), 100mL phosphate buffered saline (Gibco, ThermoFisher Scientific), 112mL of culture media with resuspended cells (∼1.2 million cells). The mixture was stirred gently at 37°C and poured into a plexiglass mould, see Figure 3.2, to set over 24 hours. The resulting phantoms had an elastic modulus of ∼10 kPa, similar to what would be expected for soft tissue (Leclerc et al., 2012; Bensamoun et al., 2011). The customised mould has four transparent windows, allowing for simultaneous application of shock waves, imaging and lighting. Hence, the target cells embedded in the sample can be imaged during shock wave experiments. The low cell density employed here allowed for the separation of individual cells and their homogeneous distribution in the sample so that a single cell can be observed during shock wave interactions.

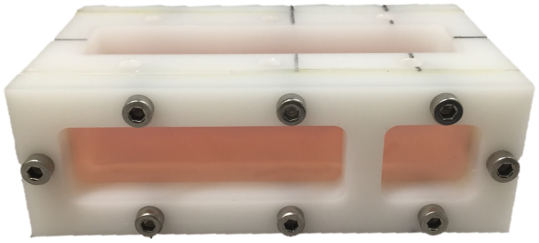

Figure 3.2: Sample mould containing cell-agarose gel. It has four transparent windows for imaging, lighting and applying shock waves at the same time

The viability of cells in the phantom was assessed by using a trypan blue solution (which selectively stains dead cells) 24 hours after they were embedded in the tissue phantom. Figure 3.3(a) shows a healthy cell after 24 hours in the tissue phantom with a well defined boundary. In comparison Figure 3.3(b) shows a cell that was non-viable, based on the blue stain, and also demonstrated a diffuse cell boundary. Fewer than 1% of cells were non-viable after 24 hours in the tissue phantom. The distinctive diffuse boundary was used to identify and exclude dead cells in the phantom when high speed imaging was done.

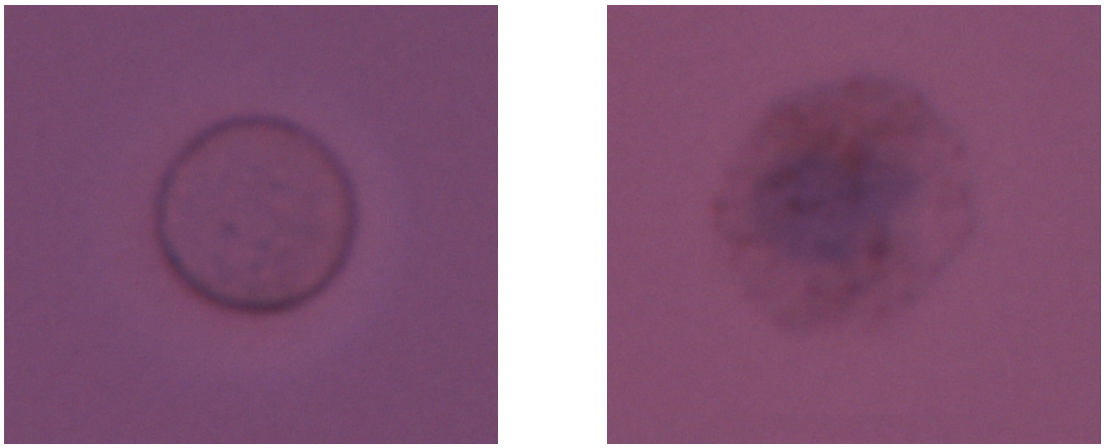

(a) (b)

Figure 3.3: Examples of HK-2 cells (at 40× magnification) embedded in a 3D agarose tissue phantom. (a) a healthy cell with a well defined intact boundary; (b) a dead cell showing a diffuse boundary.

3.1.2 Shock wave source

A STORZ shock wave device (Minilith SL1-0G, STORZ) was used to generate shock waves. The Minilith is an electromagnetic source which has a magnetic coil and a metal membrane opposite to it. A strong varying magnetic field is induced by a high current pulse going through the coil. The electromagnetic forces thus accelerate the metal membrane away to create acoustic pulses which are focussed by an acoustic lens. The focus occurs 50mm from the face of the source and the focal zone is ellipsoidal in shape approximately 25mm long in axial direction by 2.4mm in diameter.

3.1.3 Pressure measurement with Fibre-optic probe hydrophone (FOPH)

The shock wave pressure was measured inside the tissue phantoms using a customised FOPH which can measure acoustic pressure up to 100 MPa (Jessica E Parsons, 2006; Betney et al., 2015). The shock wave pressure propagating in the medium temporally causes a change of the medium density and hence influences the index of refraction of the medium. These changes can be captured by analysing the reflected light intensity based on piezo-optic effects (Jessica E Parsons, 2006).

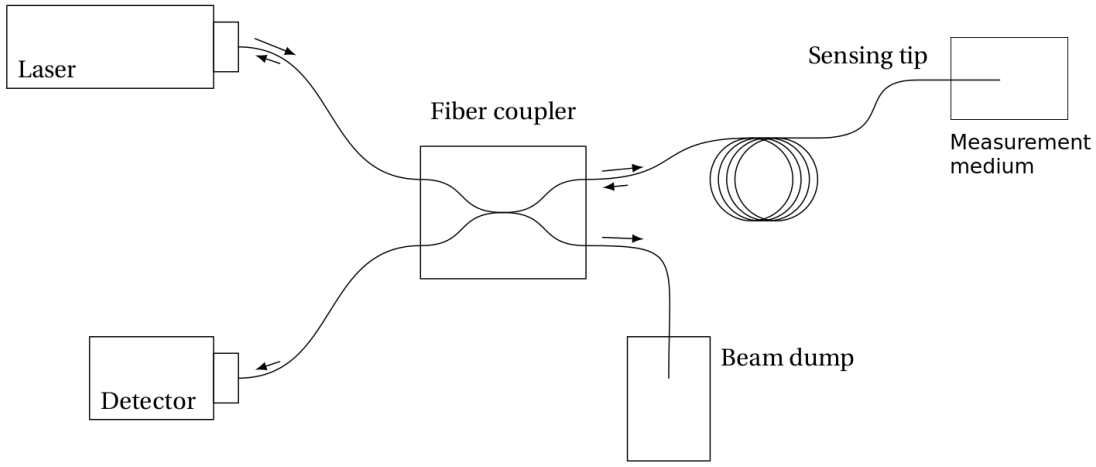

Figure 3.4: Schematic diagram of the customised FOPH (Betney et al., 2015). The arrows show the direction of light propagation.

The FOPH (shown in Figure 3.4) was built by Dr. Phillip Anderson (University of Oxford), which mainly consists of a 850 nm laser (QPhotonics QFLD-850-1000M) with a constant output, a 100 µm beam core optical fibre (Gould Fiber Optics 64-02522-30-05001) inserted into the medium, a silicon fixed gain detector (Thorlabs, PDA10A-EC) recording the reflected light measured at the fibre tip, and a multi-mode fibre-coupler (Gould Fiber Optics 15-22500-50-66640) for light transmission.

Voltage to index of refraction: the voltage output V from a photodetector is proportional to the light reflected $R(n)$ at the fibre tip.

$$V(n) = gR(n) + S \tag{3.1}$$

where g is the gain and S is an offset due to the cross-talk in the fibre-coupler. They can be inferred by measuring the voltage output from multiple materials with known refractive index (air, water or calibration oil). The reflectivity $R(n)$ is defined as:

$$R(n) = \left(\frac{n_f - n}{n_f + n}\right)^2 \tag{3.2}$$

where n_f is the index of refraction at the fibre which is assumed to be constant in all conditions ($n_f = 1.33$). n is the index of refraction of the medium.

By inverting Equations (3.1)-(3.2), the index of refraction of the medium can

be measured as:

$$\begin{cases} n(V) = n_f \dfrac{1-k}{1+k} \\ k = \sqrt{\dfrac{V-S}{g}} \end{cases} \tag{3.3}$$

Index of refraction to density: According to Gladstone-Dale relation (Gladstone and Dale, 1863),

$$\frac{n(t)-1}{\rho(t)} = constant \tag{3.4}$$

With the known ambient conditions (n_0, ρ_0), the medium density can be inferred as:

$$\rho(t) = \rho_0 \frac{n(t)-1}{n_0-1} \tag{3.5}$$

Density to pressure: The link between density and pressure is established through the Tait Equation of State,

$$p(\rho) = (Q + P_0)\left(\frac{\rho}{\rho_0}\right)^{\gamma} - Q \tag{3.6}$$

where $Q = 295.5$ MPa, $\gamma = 7.44$ for the conditions $T = 20°$C, $P_0 = 100$ kPa and ρ_0 = 1000 kg/m^3 (Jessica E Parsons, 2006). Therefore, using Equations (3.3)-(3.6), the pressure can be calculated from the voltage measured from the photodiode.

3.1.4 High speed camera and lighting source

An ultra-high speed camera (SIMX 16, Specialised Imaging) was used in the experiment. This camera has 16 channels which can be triggered independently with a maximum frame rate of 200 million frames per second (i.e., 5ns exposure time per frame). One drawback for this camera is that the total number of imaging frames is limited to 16. Hence, a trade-off between frame rate and imaging duration needs to made in order to capture the phenomena of interest. The frame rate used in the experiment was 3.3Mfps (interframe time of 300 ns with an exposure time of 200ns) to record the cell deformation under the overall shock wave duration with acceptable image quality as shorter time resulted in too little light to generate images of sufficient fidelity. The camera was connected to a 20× microscopic objective (UMPLFLN20XW, Olympus) through a turning prism mirror (CM1-P01, Thorlabs) to magnify the region of interest and thus

allow for close observation of a single cell (image resolution: 0.2 µm/pixel; field of view: 1.325 mm in diameter). All the connections between the microscopic objective and the camera were sealed to minimise interference from the ambient light.

The agar gel was backlit with a high speed visualisation laser (SI-LUX640, CAVITAR) which was fitted with a collimating lens. The visualisation laser was mounted onto a 3D microstage to align with the camera objective.

3.1.5 System alignment

In order to image single cell deformation under shock waves, the target cell needs to be aligned with both the shock wave focal zone and the imaging field of the 20× microscopic objective. This was achieved by placing a piezoelectric needle hydrophone (Müller Instruments) inside the gel coupled to the shock wave source.

The alignment between the microscopic objective connected to the camera, the tissue phantom and the laser was achieved by tuning the microstages for both the tissue phantom and the laser until a sharp image of the tip of the needle hydrophone inserted in the phantom was observed with the optimal light on the background.

The needle hydrophone was then aligned with the shock wave focal point by comparing the measured pressure to the reference value pre-measured at the shock wave focal point. The shock wave transducer was manually adjusted accordingly to make sure the measurement from the needle hydrophone matched with the reference value. This thus aligned the optics and shock wave source.

The alignment of the needle hydrophone to both the imaging field and the shock wave focus ensures that the hydrophone can be imaged properly while being at the shock wave focal zone. Target cells were then translated to the focii position by only sliding the sample in the coronal direction (i.e. X direction in Figure 3.1) without disturbing the position of the shock wave source or optics, until the hydrophone was out of the region of interest and a cell could be observed. The optical system was finely adjusted (but still within the 2mm focal spot of the shock source) to bring the cell sharply into focus.

3.1.6 Imaging procedures

An electromagnetic radiation detector was mounted onto the shock wave source which detected the electromagnetic signal generated when the shock wave source was excited. An oscilloscope was then used to generate a Transistor-Transistor Logic signal to trigger the camera after detecting a minimum of 175 mV signal with the electromagnetic radiation detector. Each camera channel was programmed with a different triggering time delay which allows for the capture of cell interactions with shock waves at different observatory time points. The imaging experiment was repeated on 8 different target cells per cell line with 3 different shock wave energy levels.

For a target cell, high speed images were taken both in its reference state (i.e., before triggering shock waves) and during shock wave loading with the same imaging settings. The cell images taken during shock wave exposure were always compared to their reference images in the same camera channel to avoid channel-to-channel differences introduced by the spatial misalignment between different camera channels.

3.2 Post-imaging analysis

Post-imaging analysis involved four image processing steps: image filtering, registration, automatic segmentation and feature extraction in order to determine cell boundaries. From the cell boundary, area and perimeter were used for quantitative analysis. All the analysis were implemented in MATLAB scripts and C++ programs.

3.2.1 High speed image filtering

Ultra-high speed images are generally noisy due to the low light levels, thus image filtering is desirable to allow for automatic cell contour segmentations. A non-local means (NL-means) filter was applied to reduce noise while preserving the fine features of the original images (Buades et al., 2005). This algorithm takes advantage of the high degree of redundancy of images, i.e. images are constituted of patterns which are usually repetitive across the image (Buades et al., 2005). Hence a noise reduced image can be reconstructed in which the value of any pixel is estimated by all the pixels in the image. This filtering technique is more

advanced than other local smoothing methods or frequency domain filters as in the latter methods the relevant fine structures, details and texture of the original images are also smoothed out (Buades et al., 2005).

Given a noisy image v defined in a discrete gridded format I, the estimated value for pixel i is computed as a weighted average of all the pixels in the image (Buades et al., 2005):

$$NL(v)(i) = \sum_{j \in I} w(i,j)v(j) \tag{3.7}$$

where the weights $w(i,j)$ depend on the similarity between the subsets around pixels i and j defined by the discrete grid:

$$w(i,j) = \frac{1}{Z(i)} e^{-\frac{\|v(N_i)-v(N_j)\|^2}{h^2}} \tag{3.8}$$

where the subset N_i is called the neighbourhood or similarity window of i (user-defined based on outcome quality and computational costs), $Z_i = \sum_j e^{-\frac{\|v(N_i)-v(N_j)\|^2}{h^2}}$ is the normalising factor and h is the parameter which controls the decay of the weight function.

The high speed images were firstly cropped to the region of the cell in order to improve the filter efficiency. The parameters used for the filter were optimised based on the balance between computational efficiency and filtering quality. The neighbourhood N was chosen to be 4×4 pixels, and the decay parameter $h = 100$. Figure 3.5 shows an example of cell images before and after filtering. The NL-means algorithm filtered out the background noise such as speckles and grids but kept the relevant cell features.

3.2.2 Cell contour segmentation

The cell contour segmentation algorithm consisted of an initial cell contour guess which was originally based on circle detection but was later refined by Andre Hallack (Biomedical image analysis, University of Oxford) with an image registration process. The initial guess of cell contour for each image frame was then optimised by an active contour segmentation algorithm with user-defined criteria.

Initial guess of cell contour: The initial guess of the cell contour was originally based on a refined MATLAB circle detection algorithm (MathWorks)

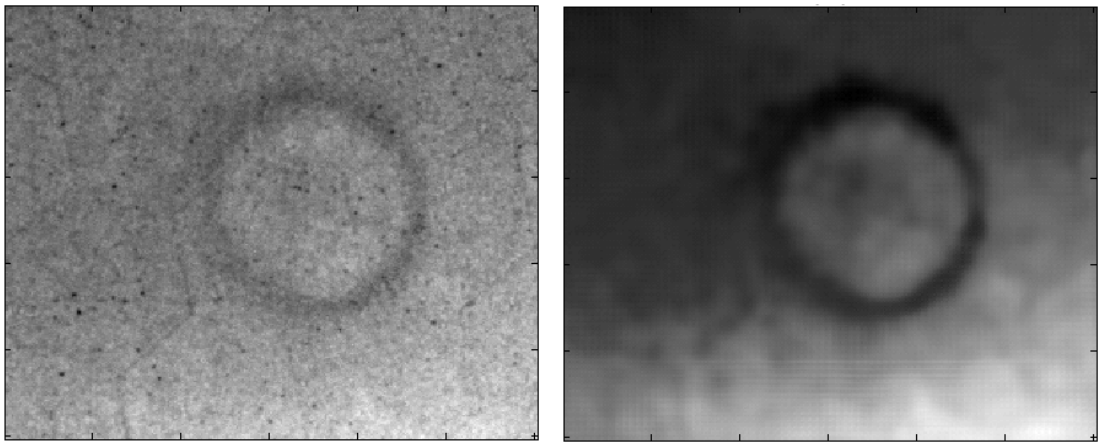

(a) (b)

Figure 3.5: (a) cropped raw image on the region of interest; (b) NL-means filtered image.

which detects any shape similar to a circle. This algorithm will be discussed in more details in Section 7.1.1.2 as it was mainly used for static cell contour analysis. A more efficient algorithm was used for the initial cell contour guess here, which was developed by Andre Hallack from the Biomedical Image analysis group in the University of Oxford. The algorithm essentially propagates the initial segmentation mask obtained by a manual segmentation of the cell contour on a reference image (i.e., one of the 16 image frames taken before shock wave exposure) to all the other high speed images.

Active contour segmentation: Cell contours in each high speed image sequences were refined automatically using an active contour segmentation (Kass et al., 1987). The initial guess of the cell contour served as the input to the active contour segmentation algorithm. The active contour segmentation is an energy-minimising spline influenced by the image features and constrained by external forces which are user-defined in order to achieve the best contour segmentation results. Any segmentation that was unsuccessful or unsatisfactory by eye was then segmented manually with three repeats.

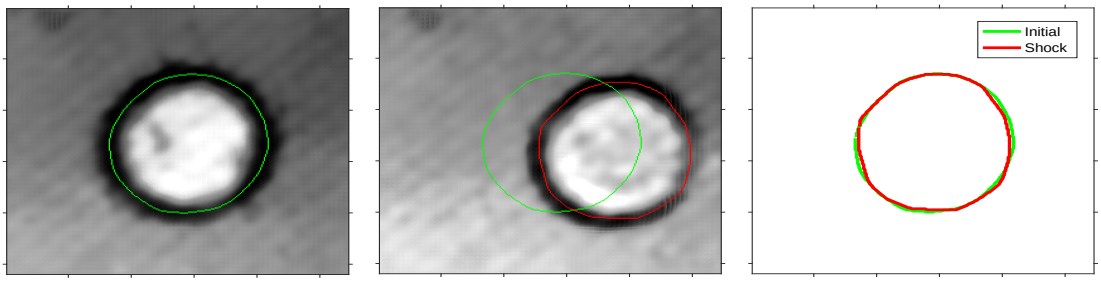

(a) (b) (c)

Figure 3.6: Deformation of a healthy HRE cell during the compression phase at energy level 8: (a) image and segmented cell contour before the shock wave was sent; (b) image and segmented cell contour during compressive phase; (c) comparison of the cell contours before (green) and during (red) shock wave exposure.

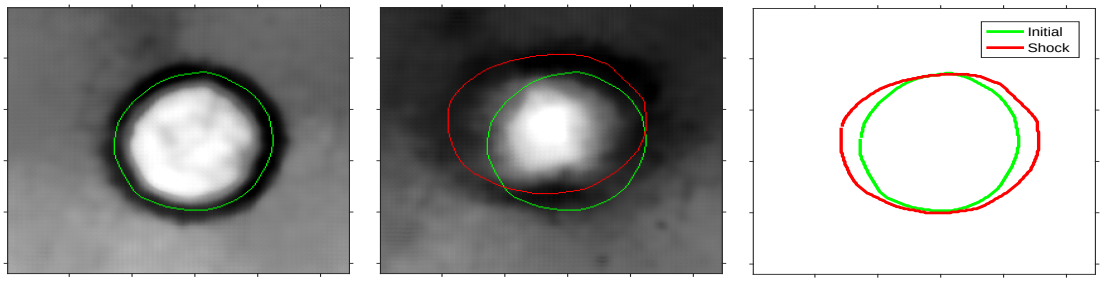

(a) (b) (c)

Figure 3.7: Deformation of a healthy HRE cell under tension at energy level 8: (a) before shock wave (b) during tensile phase (c) cell contour comparison before (green) and during (red) shock wave exposure.

3.2.3 Feature extraction and analysis

The projected cell boundary and centre of mass were determined from the cell contour segmentations. The cell features were extracted from both sets of cell images taken before and during shock wave exposure so that the change of cell contours can be quantified at different imaging time points while excluding the channel-to-channel difference. Figure 3.6 shows representative images of an individual healthy human kidney cell during the compressive phase of a shock wave at energy level 8. The cell boundary was extracted before and during the shock wave exposure and it can be seen that the contour is slightly compressed in this phase of the shock wave. Figure 3.7 shows a cell during the tensile phase and it can be seen that the boundary has expanded and also become more diffuse in the images.

The cell area was estimated by counting the number of pixels within the cell contour and the cell perimeter was evaluated by summing the distance between adjacent pixels on the contour. Normalised area and perimeter changes at each imaging time point were defined by dividing the area or perimeter difference by their initial values at the reference state (i.e., before shock wave exposure), A_0 and P_0:

$$\begin{aligned} \frac{\Delta A}{A_0} &= \frac{A(t) - A_0}{A_0} \\ \frac{\Delta P}{P_0} &= \frac{P(t) - P_0}{P_0} \end{aligned} \tag{3.9}$$

where $A(t)$ and $P(t)$ are the measurements of area and perimeter during shock wave exposure at time t.

In order to study the shearing related perimeter change which excludes the effect of area change, the shear perimeter, $\Delta P_s(t) = P(t) - P_A(t)$, was analysed by comparing the perimeter change, $P(t)$, during shock waves to P_A, the expected perimeter change due to the influence of area change for a circle.

$$\begin{aligned} P_A(t) &= P_0\sqrt{\frac{A(t)}{A_0}} \\ \frac{\Delta P_s}{P_A(t)} &= \frac{P(t) - P_A(t)}{P_A(t)} \end{aligned} \tag{3.10}$$

The time base associated with each data set was aligned based on the zero-crossing of the area change (i.e. transition between negative and positive values). This step removed the time delay between cell samples due to the misalignment of their transverse positions in the experiments.

The image processing procedures described above are summarised in Figure 3.8.

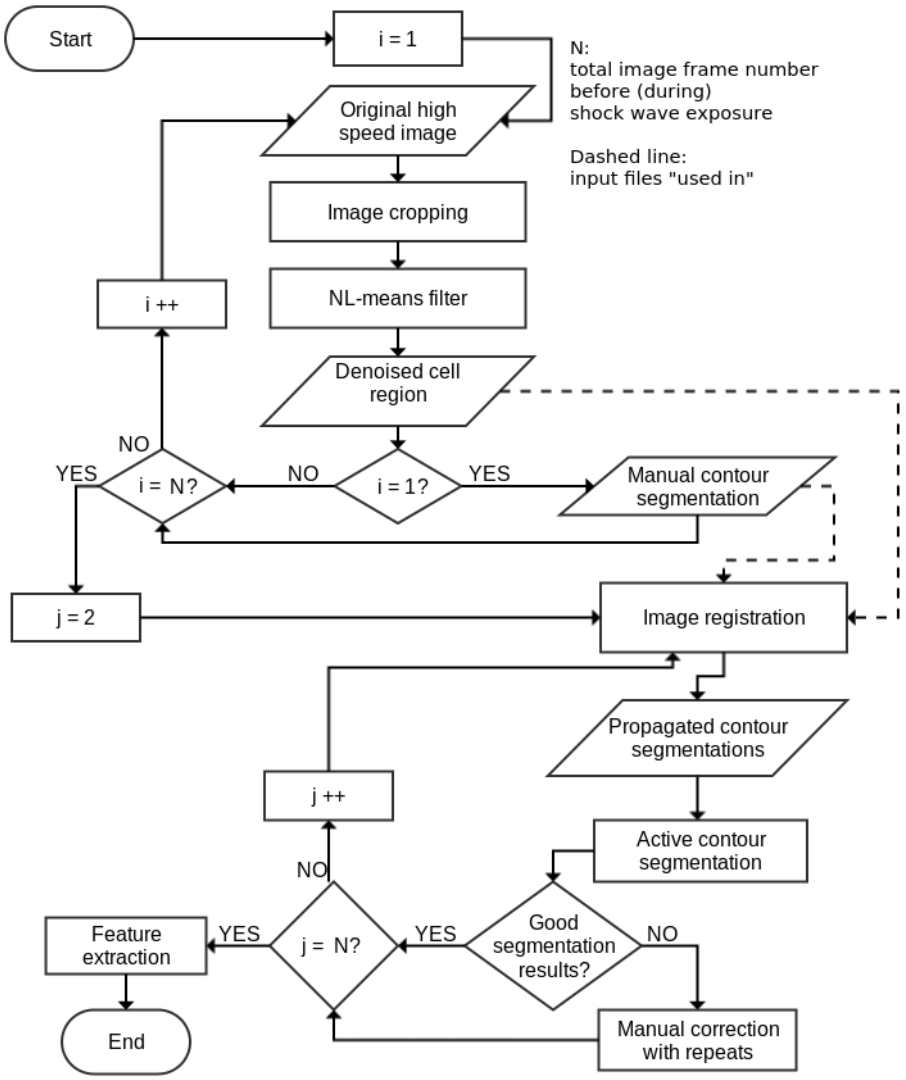

Figure 3.8: Summary of the main procedures of cell imaging procedures.

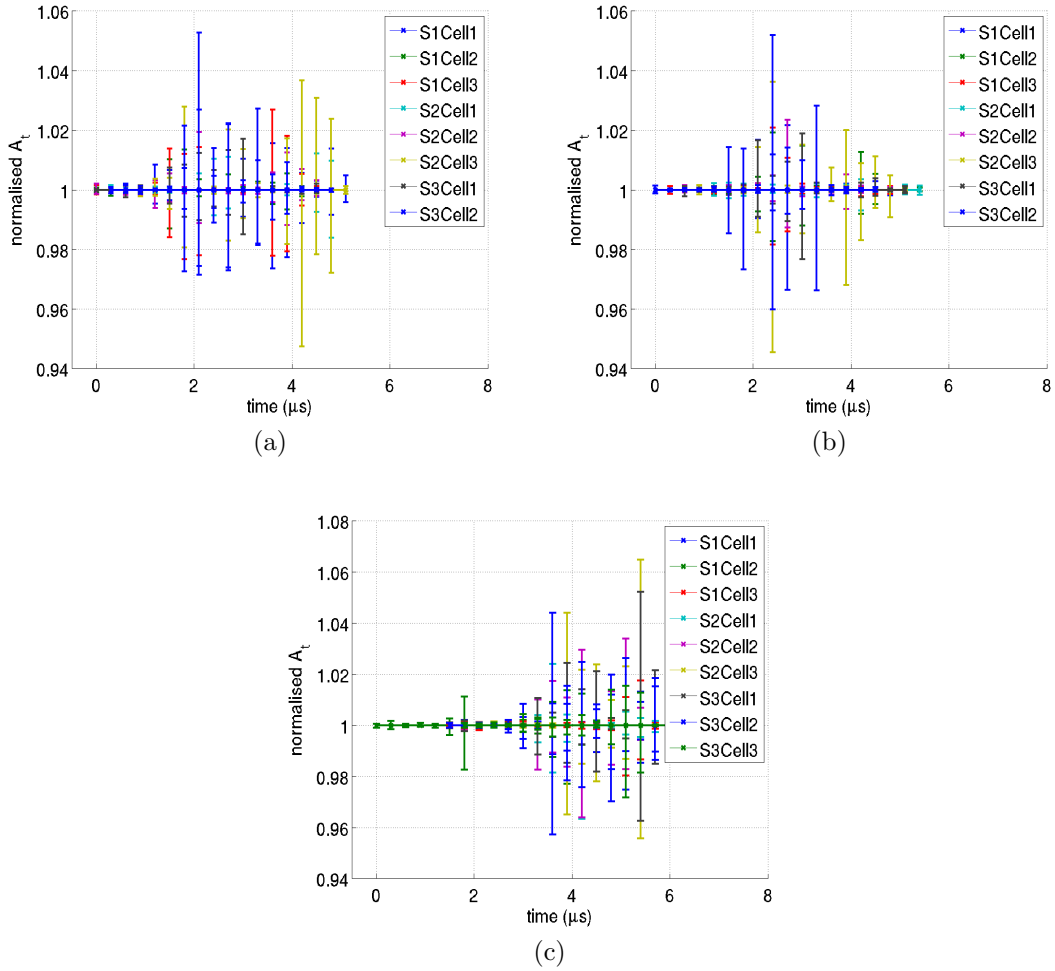

Figure 3.9: The minimum and maximum segmented areas relative to the mean value of 8 cell samples taken at shock wave energy level 8 in (a) CAKI-2 cells; (b) HK-2 cells and (c) HRE cells.

3.2.4 Segmentation variability

In order to quantify the variability in the segmentation process, a test was conducted on 8 different cells per cell line subject to shock waves with three energy levels, respectively. Each cell was manually segmented three times. The image processing algorithms described in Section 3.2.1-3.2.3 were then performed on each manual cell segmentation in order to compare the measured area in each segmentation. The segmentation variability was defined as the variation of the measured area in the three segmentations. The test was repeated for each cell sample per cell line. Figure 3.9 shows the segmentation variability of the three cell lines measured at shock wave energy level 8 where the largest variability was

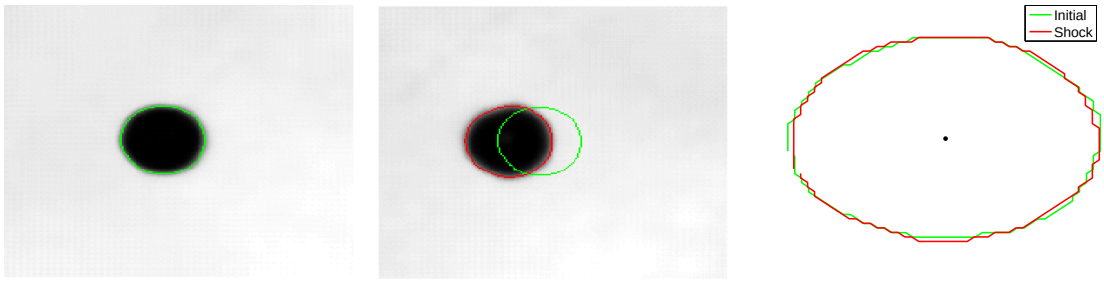

(a) (b) (c)

Figure 3.10: An example of segmented microbeads at shock wave energy level 8. (a) before shock wave exposure; (b) during shock wave loadings; (c) contour comparison.

found. In all the cell samples the maximum variability introduced to the area estimation before shock loading was less than 0.2%. During shock loading, the majority of the cell samples exhibited less than 1% variability. In a few cases a variability of 2-5% occurred during stretching, due to reduced image qualities and thicker cell contours during the tensile phase of shock wave exposure.

3.2.5 Imaging variability

During the imaging process, the movement of the cells and the interaction between acoustics and optics may result in artefacts or interference on cell images, leading to a change of cell contour during imaging which is not due to the cell deformation in response to shock waves. Therefore, 10 µm polystyrene microspheres (Polybead, black, Polyscience Inc.) were used in the same experimental setting and post-imaging analysis as that of the cells. Due to the large bulk modulus of the microbeads (∼4 GPa (Mott et al., 2008)), shock waves should not lead to a detectable area change of the beads. Therefore, they can be used to assess the influence of acousto-optic effects, bead and gel movement and image quality on the cell images. Representative images and the segmentation of a microbead are presented in Figure 3.10.

The area change of the microbead contour measured at the three shock wave energy levels are presented in Figure 3.11. The results showed that the area change of the 10 µm microbeads varied between -3% and 3% at the three shock wave energy levels. The mean variability of area change found in the three shock wave energy levels (level 4-8) were 0.1%, 0.4% and -1.1%, respectively. The area

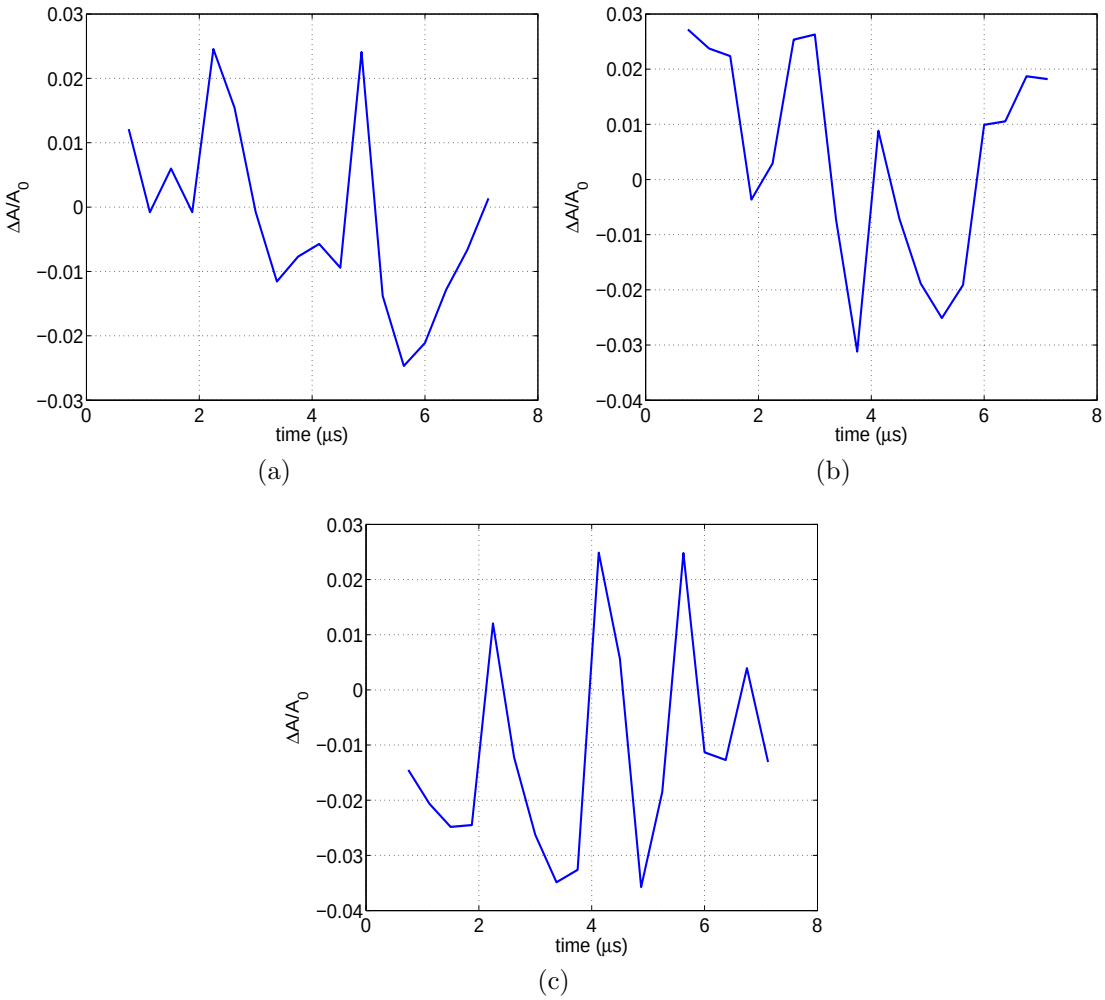

Figure 3.11: Area change of the microbead contour at different shock wave energy levels (a) level 4; (b) level 6; and (c) level 8.

change of microbeads did not show a correlation with the shock wave profile whilst that of cells showed clear negative and positive phases of area change consistent with the compressive and tensile portions of the shock wave. This indicates that the imaging variability of microbeads may not be caused by shock wave interactions but the small movement of the objects inside the gel and segmentation variability.

Other experimental variabilities such as pressure variation in each shock loading and cell sample variation due to the variation of cell condition and agaorose gel composition in each experiment are assumed negligible compared to the segmentation and imaging variabilities and are further reduced with the eight time

experiment repeats for each cell.

CHAPTER 4

Experimental results of single cell deformation under shock waves

In this chapter, the experimental measurement of single cell deformation in response to shock waves with three different shock wave energy levels is presented. The difference in multiple cell lines is also explained. It is shown that the tested cells behave differently under compression and tension: the cell deformation under compression is found to be small (less than 2%) while that during tension is in the order of 10%. The cell response is also found to be differentiated between cancer cells and normal cells under some shock wave conditions.

4.1 Shock wave pressure profiles

The waveforms of a shock wave pulse from the focus of a clinical shock wave source (Minilith SL1-0G, STORZ) at three different energy settings (level 4, 6 and 8) were measured using a bespoke fibre-optic probe hydrophone (Jessica E Parsons, 2006). Figure 4.1(a) shows the measurement taken inside the tissue mimicking phantom at the three energy levels. The standard errorbar (<10%) indicates the variation of pressure waveform in each shock wave measurement. In each case the shock wave consisted of a compressional phase (positive pressure with a duration ∼1.5 µs) followed by a tensile phase (negative pressure with a duration ∼2.1 µs). As the energy level increased three effects were observed: an increase in the peak positive pressure; a decrease in the shock rise time; and a gradual increase in the peak negative pressure. These are characteristic behaviours of a

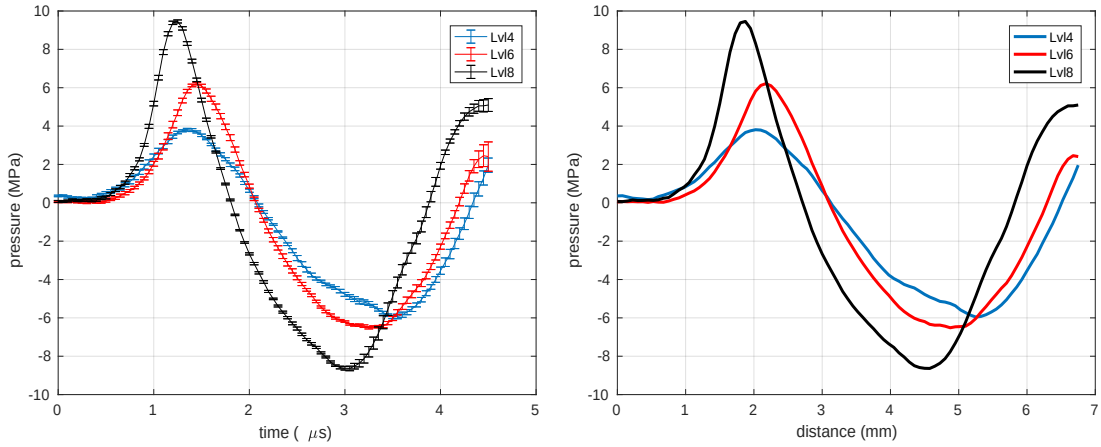

(a) (b)

Figure 4.1: Shock wave pressure measured with customised FOPH at shock wave energy settings level 4, level 6 and level 8: (a) pressure variation with time; (b) pressure with spatial distance.

focussed non-linear acoustic wave (MA and MF., 1997). Figure 4.1(b) shows the spatial domain of the shock wave profiles. Compared to the cell size (∼20 µm), a pressure change of 0.5 MPa is expected across the cell. The plane wave acting on individual cells with pressure gradient across the cell thus results in a slightly ellipsoidal shape of cell deformation in the axial direction. More details about the pressure measurement are discussed in Appendix A.

4.2 Single cell deformation under a shock wave

An individual healthy human kidney (HRE) cell was selected using a 20× microscopic objective. While under the action of shock waves, the cell deformation was recorded by the ultra-high speed camera in the axial plane of shock waves propagation. Images were acquired as described in Chapter 3. Three shock wave energy levels were used on the 8 cell samples, respectively. At each shock wave energy level, the averaged cell deformation from the 8 cell samples was analysed, in terms of area and perimeter change of the projected cell contour over time, see Figure 4.2. Assuming an isotropic deformation in the axial direction, the area and perimeter changes were used as 2D proxies of the volumetric and deviatoric response of the cell, respectively.

Figure 4.2 shows that under a shock wave, cells initially undergo a small area

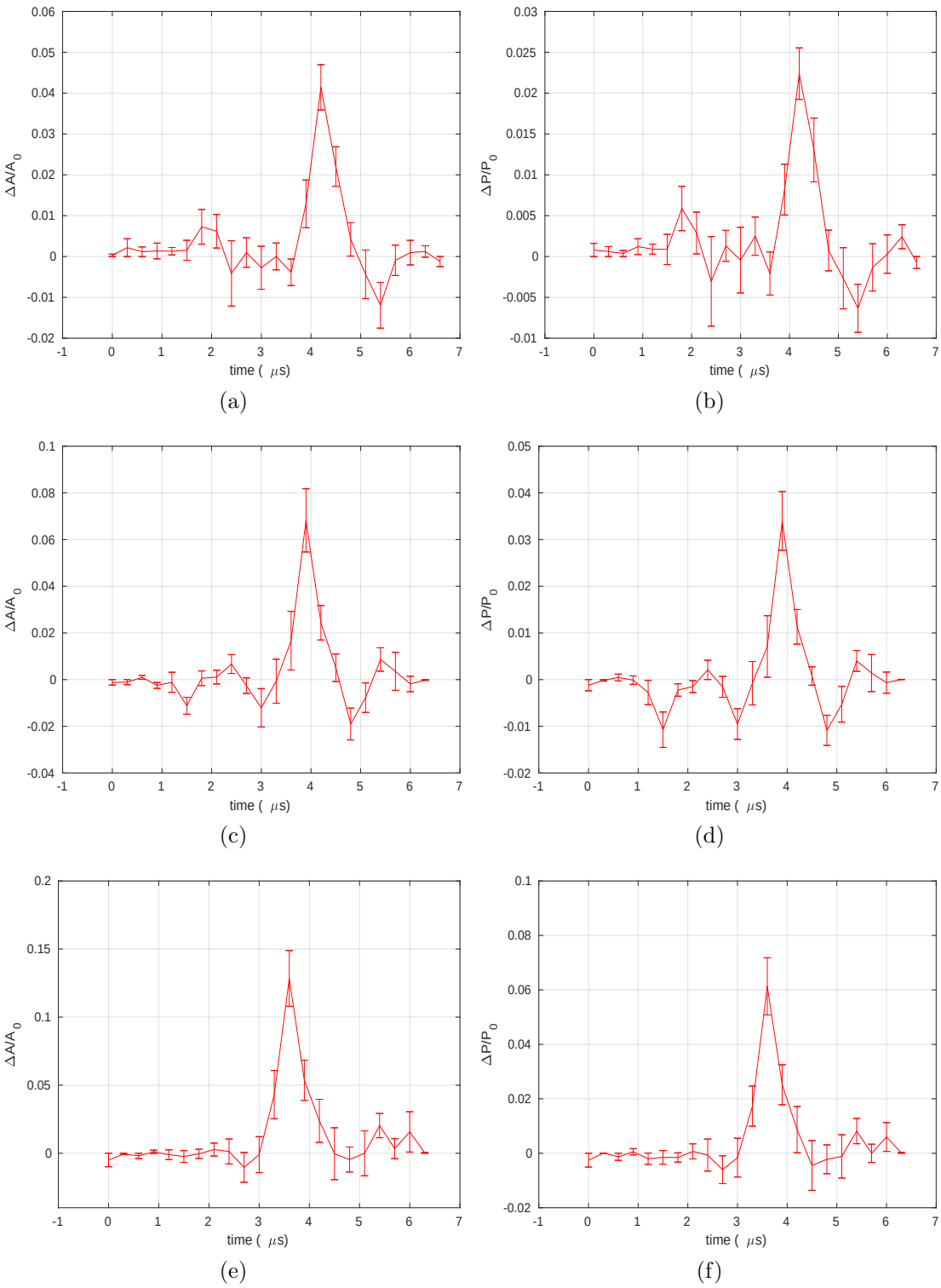

Figure 4.2: Cell area and perimeter change of HRE cells over time at shock wave energy (a)-(b), level 4, (c)-(d), level 6 and (e)-(f) level 8. Error bar indicates the standard error of the measured data.

Table 4.1: Estimation of cell bulk moduli.

Energy level	Shock phase	Maximum pressure	$\Delta A/A_0$	Estimated bulk modulus
Lvl 4	Compression	∼4 MPa	∼-0.5%	0.5 GPa
	Tension	∼-6 MPa	∼4%	100 MPa
Lvl 6	Compression	∼6 MPa	∼-1%	0.4 GPa
	Tension	∼-7 MPa	∼7%	66 MPa
Lvl 8	Compression	∼10 MPa	∼-1%	0.7 GPa
	Tension	∼-8 MPa	∼13%	51 MPa

compression followed by a large expansion which increases with the increase of shock wave energy levels (up to 13% area increase at shock wave energy level 8). The timing of cell deformation was found to be consistent with the compressive phase and tensile phase of the shock wave, however, the six-fold increase in cell area between tension and compression was not consistent with the fact that the magnitude of tensile stress was comparable to that of compression with similar loading rates. These data suggest that the cells are stiffer during compression than in tension. Based on simple relationship between pressure and volume $P = -K\frac{\Delta V}{V_0}$, and assuming isotropic cell deformation (i.e., $\frac{\Delta V}{V_0} = \frac{3}{2}\frac{\Delta A}{A_0}$), the cell area change during compression and tension can be used to estimate the cell bulk modulus under compression and tension, respectively, see Table 4.1. A rough estimation using the maximum pressure and cell area change indicates that the cell bulk modulus for compression is in the order of GPa while that for tension is in the order of tens MPa. However, it is important to note that the calculation is done under a hydrostatic condition. A numerical model characterising the mechanical properties of the cell is discussed in Chapter 5.

As a circle changes in radius from an initial radius r_0 to a different radius r_t, the area and perimeter are given by:

$$\begin{aligned} \frac{\Delta A}{A_0} &= \frac{2\pi\left(r_t^2 - r_0^2\right)}{2\pi r_0^2} \simeq \frac{4\pi r_0 \Delta r}{2\pi r_0^2} = \frac{2\Delta r}{r_0} \\ \frac{\Delta P}{P_0} &= \frac{2\pi\left(r_t - r_0\right)}{2\pi r_0} = \frac{\Delta r}{r_0} \end{aligned} \tag{4.1}$$

The ratio of the area change to perimeter change would therefore be a factor of two. The area change of the HRE cells showed a similar pattern as the perimeter change but with a factor of two, see Figure 4.2, indicating that the perimeter change is strongly influenced by the area change.

The segmentation variability and imaging variability due to image quality, cell movement and acoustic-optical effects were analysed as in Chapter 3, which were found not to mask the cell deformation under shock waves.

4.3 Comparison of shock wave interactions in different cell lines

The experiments were repeated with the virus-transformed immortalised kidney cells, HK-2, and kidney cancer cells, CAKI-2. Figure 4.3 (a)(c)(e) show the area change for the HK-2 cells at the three shock wave energy levels and Figure 4.3 (b)(d)(f) show the data for CAKI-2 cells.

It can be seen that both the immortalised cells and cancer cells exhibit the same qualitative behaviour as the healthy cells (a larger response to the tensile phase of the shock wave than to the compressive phase).

Further the cell area change increases with the shock wave energy level setting and the difference in the maximum area increase among the three cell types also becomes more distinguishable, see Figure 4.4: at energy level 4, the area increase in all three cell lines was found to be between 3.3% and 4.1%; at shock wave energy level 6, the area increase was between 6.3% and 8.5%; and at energy level 8, the maximum area increase was 17% in the HK-2 cells, 13% in HRE and 9% in CAKI-2. The difference was statistically significant for HK-2 and CAKI-2 cells with a p-value of less than 5% in the Mann-Whitney U test. The much larger area increase found in HRE and HK-2 cells only occurred at shock wave energy level 8, indicating that there may be a stress threshold governing the large deformation of them. However, a definitive conclusion can only be drawn after testing the cell response at intermediate shock wave energy levels.

Furthermore, the area expansion duration of HRE and HK-2 cells were around 1.5 µs, while that of CAKI-2 cells was around 1.8 µs. The duration of the tensile deformation of all three cell types was slightly shorter than the 2.1 µs duration of the shock wave tensile phase which suggests there may be a hysteresis effect presented in the transition between compression and expansion.

As shown in Figure 4.5, for all cell types, a constant factor around two was found between the area change and the perimeter change $\left(\text{i.e., } \frac{dA}{A_0} \simeq 2\frac{dP}{P_0}\right)$, show-

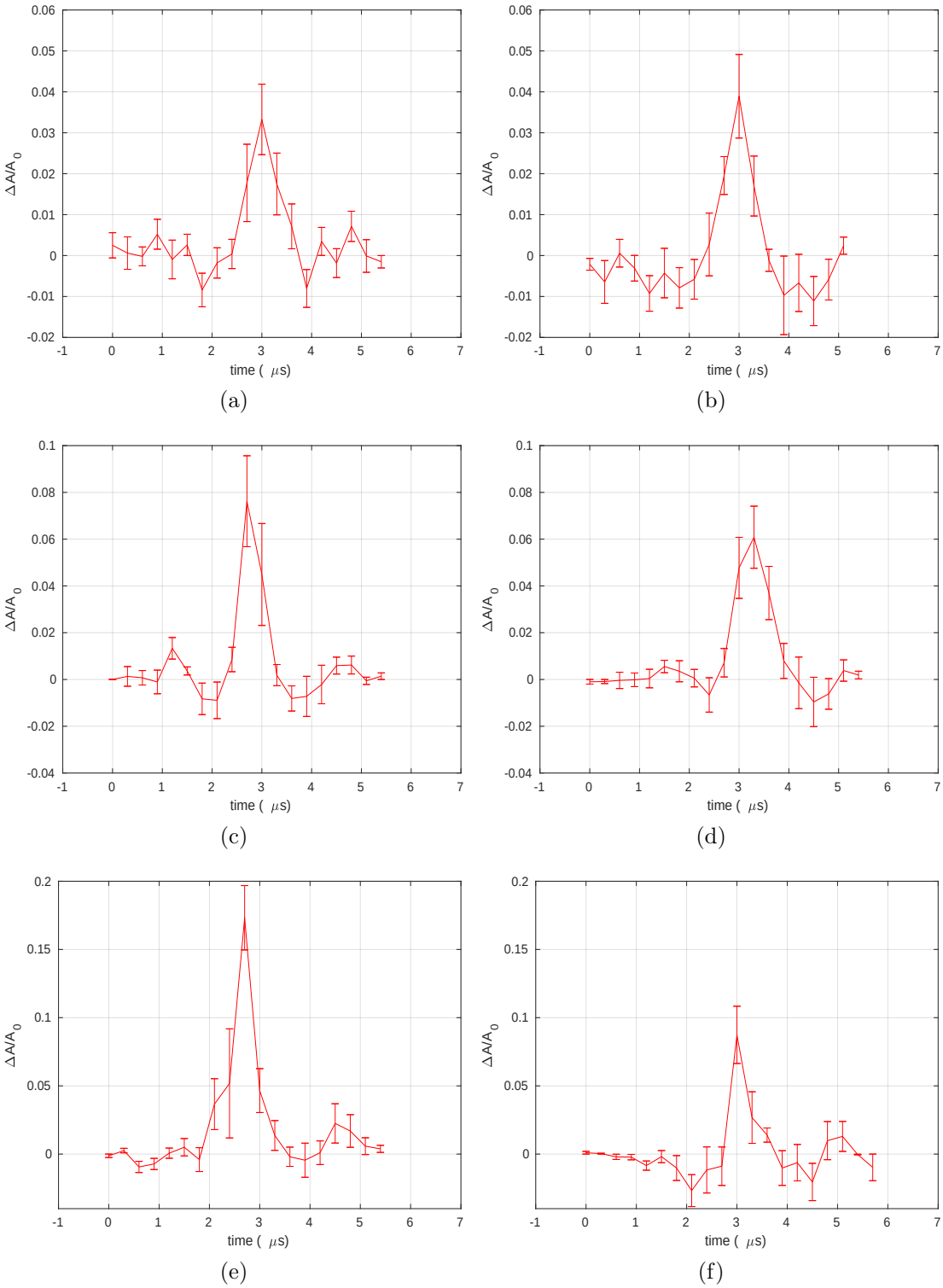

Figure 4.3: Cell area change of HK-2 and CAKI-2 cells at shock wave energy level 4, level 6 and level 8 for: HK-2 cells ((a)(c)(e)) and CAKI-2 cells ((b)(d)(f)).

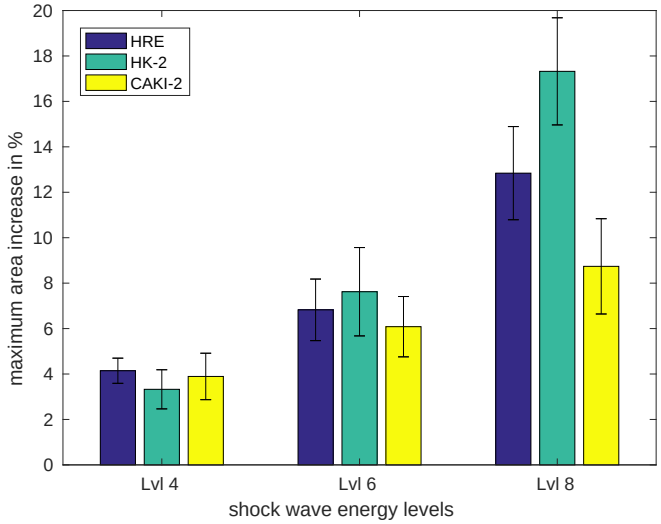

Figure 4.4: The maximum area increase for the three cell types at three shock wave energy levels: (blue) HRE cells; (green) HK-2 cells and (yellow) CAKI-2 cells.

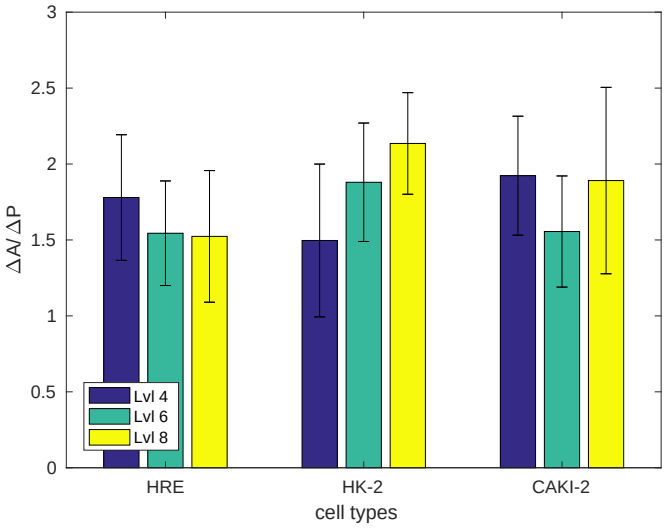

Figure 4.5: The ratio between area change and perimeter change of single cell deformation in response to shock waves. HRE, HK-2 and CAKI-2 cell lines are respectively studied.

ing that the shearing effect was insignificant compared to the volumetric effect for all cell types. The measured shear perimeter change as in Equation (3.10), see Figure 4.6, which excludes the influence of area change on perimeter change, was found to remain less than 0.5%, further confirming a small shearing effect in the experiment.

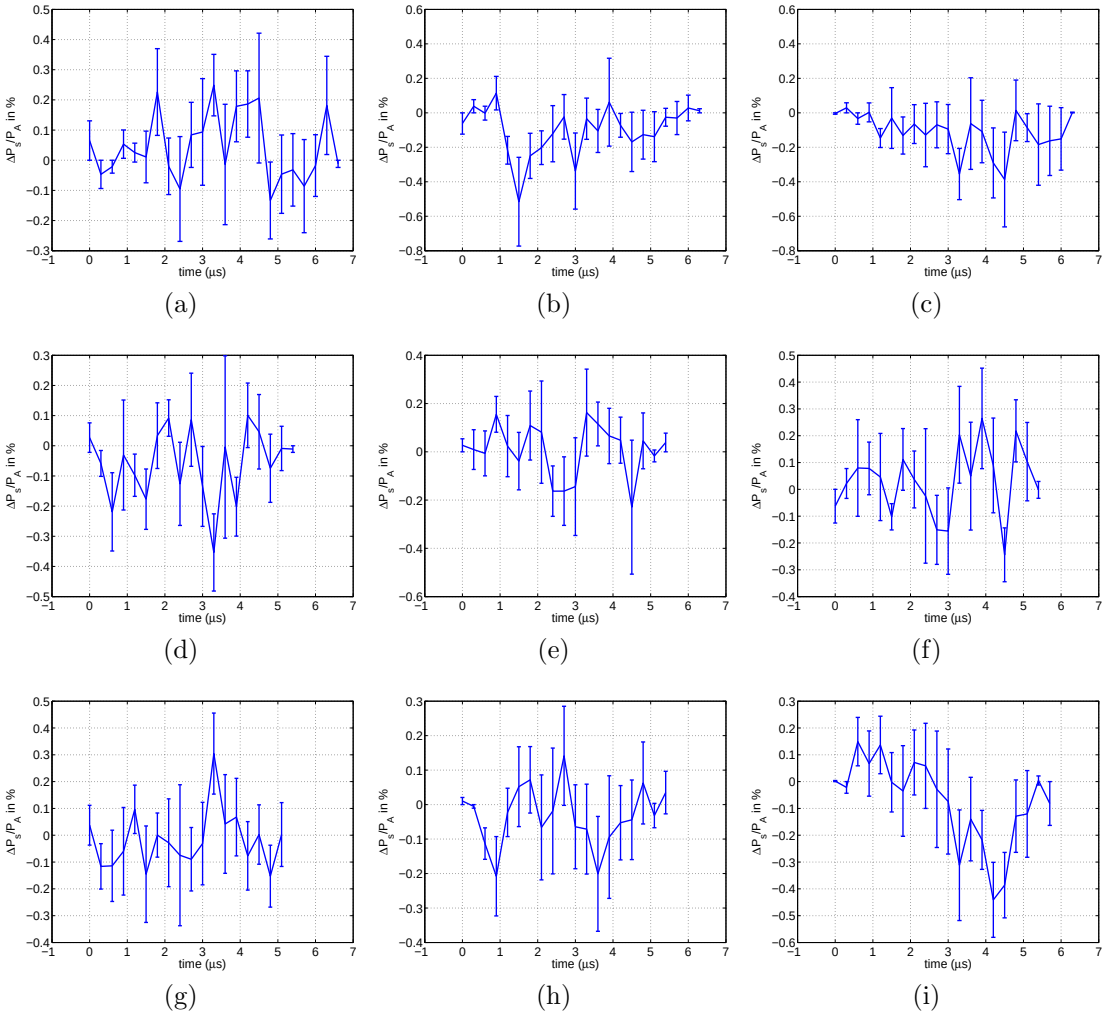

Figure 4.6: Shear perimeter change for the three cell types: (a)-(c) HRE cells, (d)-(f) HK-2 cells, (g)-(i) CAKI-2 cells, at shock wave energy levels 4-8 respectively.

4.4 Discussion

The experimental data showed a consistent trend in single cell deformation at all three shock wave energy levels. The results showed that cells were stiff under compression (the compressional deformation were less than 2%) but could be largely stretched under tension (the maximum tensile deformation were in the order of 10%) even though the compressional phase of the shock wave was comparable in magnitude and strain rate to the tensile phase. This indicates that the mechanical behaviour of the cells under shock waves has different characteristics in response to compression and tension.

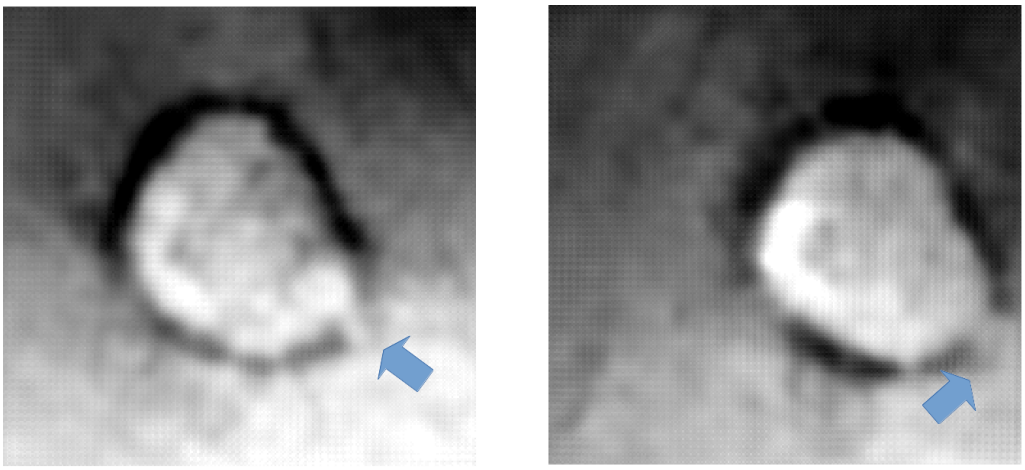

Figure 4.7: Two examples of blebbing effects captured during the experiments. Arrows point to the blebs

For the shock wave interactions studied here the deformation of the cells is consistent with the concept that under compression the presence of water in the cells results in a bulk modulus similar to water (i.e., incompressible). Under tension the decrease in bulk modulus suggests that some combination of mechanical structure failure or fluid cavitation occurs within the cell. In the data shown in Figure 4.3 no macroscopic failure or cavitation was observed. Possible mechanisms for micro-rupture include: intracellular cavitation in the cytoplasm (Brujan, 2010), intramembrane cavitation where rupture occurs between the layers of the lipids that make up the cell membrane (Krasovitski et al., 2011), or phase transition of the lipids in the cell membrane from a gel state to a fluid state (Lewis and McElhaney, 2012). In a few cases ($\sim$10%) blebbing effects (i.e., the protrusion of the cell membrane due to disruption at the cell membrane cortex) were observed (Figure 4.7 shows two examples), which is consistent with the hypotheses of rupture or phase transition of the cell membrane.

The experiments demonstrated that the projected cell area expansion reached 13% in HRE, 17% in HK-2 and 8.5% in CAKI cells at the highest shock wave energy level. The large deformation under tension indicates that both cell damage and increased membrane permeability are likely to occur during this stage of the shock loading. The scale factor of two between area and perimeter changes and the small shear perimeter change indicate that the cell deformation is mainly governed by its volumetric response.

CHAPTER 5

Numerical methods

A shock wave-cell model is developed to study the biophysical mechanisms of shock wave interactions with cells. The material properties used in the proposed model are calibrated against the experimental observations illustrated in Chapter 4, by adjusting the material parameters in the model until an agreement of cell response is achieved between the simulation results and experimental observations.

5.1 Model geometry

Figure 5.1 shows the proposed 3D Finite Element (FE) model, which consists of a tissue model describing the surrounding extracellular matrix and an embedded cell model with a diameter of 20 µm. The shock waves at three energy levels measured in the experiment were applied at the top surface of the model and assumed to propagate as a plane wave in a small volume of medium. Hence, in the simulation, the lateral boundaries were prohibited from moving laterally, and the bottom was clamped. The cell was positioned 50 µm from the top surface to minimise losses in the propagation of the incident wave, and the overall model length was taken to be 5 mm to ensure that wave reflections from the bottom boundary occurred only after the shock wave tail fully crossed the cell.

The geometry was meshed with 236120 linear tetrahedron elements (C3D4) and the numerical model was implemented in an explicit solver with the time scale factor of 0.5.

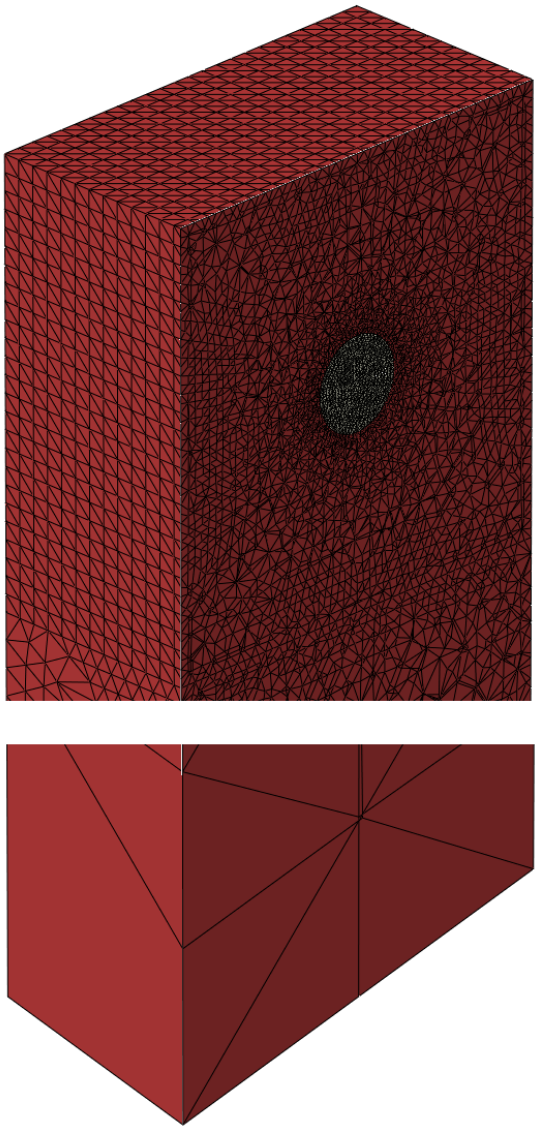

Figure 5.1: Cross-sectional view from the mid-plane of the FE model: tissue with an embedded cell. The tissue is 100 µm×100 µm×5 mm in dimension with non-linear meshing.

5.2 Constitutive frameworks

Recalling from Equations (2.3)-(2.5), for viscoelastic materials, the second Piola-Kirchhoff stress $\mathbf{S}$ can be defined by a combination of elastic response $\mathbf{S}^{\circ}$ and viscous response $\mathbf{S}_{vis}$ (Simo and Hughes, 2008):

$$\mathbf{S} = \mathbf{S}^{\circ} + \mathbf{S}_{vis} \tag{5.1}$$

where the elastic stress $\mathbf{S}^{\circ}$ can be further decomposed to its volumetric stress, $\mathbf{S}^{\circ}_{vol}$, and isochoric (deviatoric) stress, $\mathbf{S}^{\circ}_{iso}$, which can be derived from the elastic strain energy (Holzapfel, 2000):

$$\mathbf{S}^{\circ} = \mathbf{S}^{\circ}_{vol} + \mathbf{S}^{\circ}_{iso} \tag{5.2}$$

The volumetric response ($\mathbf{S}^{\circ}_{vol}$) of the cell model was presented by a modified acoustic Equation of State (EoS), which takes into account of the difference of cell response under compression and tension as observed in the experiment (Chapters 3 and 4). The viscoelastic deviatoric response ($\mathbf{S}_{iso} = \mathbf{S}^{\circ}_{iso} + \mathbf{S}_{vis}$) of the model is taken from the first order-generalised Maxwell viscoelasticity model. The surrounding extracellular matrix was modelled by non-linear elasticity in combination with a linear acoustic EoS with the water bulk modulus. In the following material description, the Kirchhoff stress ($\boldsymbol{\tau} = \mathbf{FSF}^{T}$) will be used for the convenience of mathematical operations.

5.2.1 Acoustic Equation of State

To consider the experimental finding in which cells responded significantly differently to compression and tension, the first approach was to modify a linear EoS by employing a bilinear bulk property for compression and tension respectively (see Figure 5.2).

With the proposed EoS, when the pressure is below the transition pressure threshold during the tensile phase, the pressure is linearly related to the density change with the bulk modulus for compression K_C. On the other hand, when the pressure exceeds the transition pressure threshold, a tensile bulk modulus, K_T,

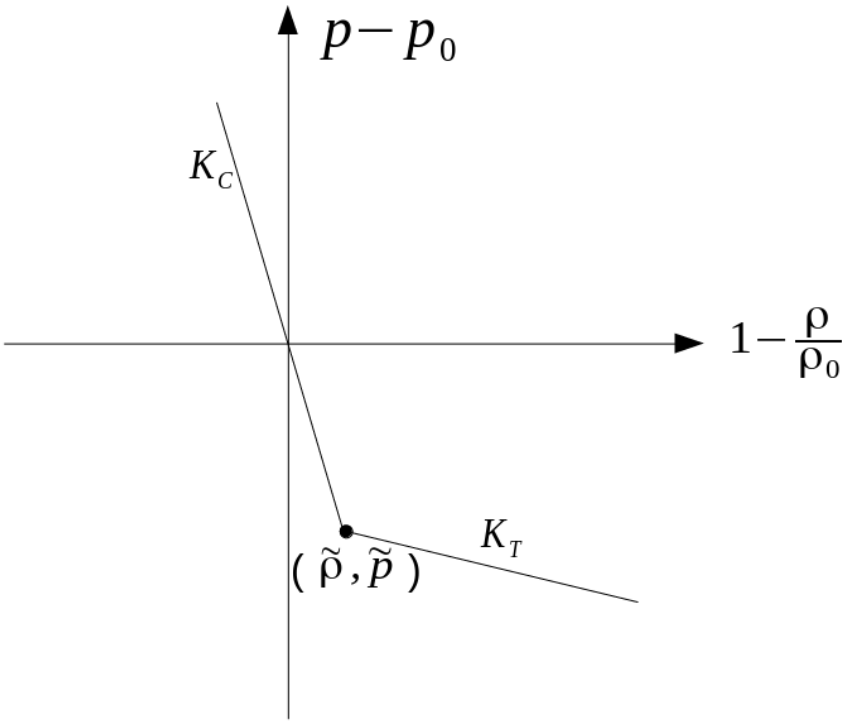

Figure 5.2: Schematic of the modified EoS to account for the different bulk moduli for compression and tension phases of shock waves.

is applied with a pressure shift at the transition, Δp:

$$p = \mathrm{H}(\widetilde{p} - p)\left(K_T \frac{\rho - \rho_0}{\rho_0} + \Delta p\right) + \mathrm{H}(p - \widetilde{p})\left(K_C \frac{\rho - \rho_0}{\rho_0}\right) - K_C \frac{\widetilde{\rho} - \rho_0}{\rho_0} \tag{5.3}$$

where H is the Heaviside function, K_C and K_T are the bulk moduli corresponding to compression and tension respectively, $\Delta p = (K_C - K_T)(\widetilde{\rho} - \rho_0)/\rho_0$ is the pressure shift at the transition, and $\widetilde{p}$ and $\widetilde{\rho}$ are the transition pressure and density, respectively. ρ_0 is the density at initial state.

The surrounding tissue-mimicking phantom was also described by a linear EoS with the water bulk modulus ($K_C = 2$GPa):

$$p = K_C \frac{\rho - \rho_0}{\rho_0} \tag{5.4}$$

The volumetric kirchhoff stress $\boldsymbol{\tau}^{\circ}_{vol}$ is thus represented as:

$$\boldsymbol{\tau}^{\circ}_{vol} = Jp\mathbf{I} \tag{5.5}$$

5.2.2 Viscoelasticity

The deviatoric response of the model is described by a viscoelasticity framework (Simo and Hughes, 2008), where the second Piola-Kirchhoff stress $\mathbf{S}$ of the viscoelastic system (see Figure 5.3) depends on the initial elastic response $\mathbf{S}^\circ$ and the evolution of the stress-like viscous internal variables $\mathbf{Q}_i$ (recall from Equation (2.5)):

$$\mathbf{S}(t) = \mathbf{S}^\circ(t) \underbrace{- J^{-\frac{2}{3}} \mathrm{DEV}[\sum_{i=1}^{N} \mathbf{Q}_i(t)]}_{\mathbf{S}_{vis}} \tag{5.6}$$

The initial elastic stress is the derivative of the elastic stored energy function W with respect to the right Cauchy-Green tensor $\mathbf{C}$ and can be defined by the volumetric and volume-preserving (deviatoric) constributions (Simo and Hughes, 2008):

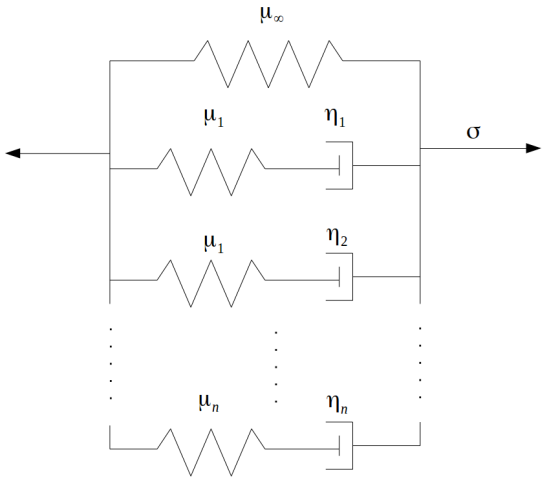

Figure 5.3: Schematic of the viscoelasticity material framework in small deformation, on which non-linear viscoelasticity is built (Simo and Hughes, 2008).

$$\begin{aligned} \mathbf{S}^\circ(t) &:= 2\partial_{\mathbf{C}} W(\mathbf{C}) \\ &= JU^{\circ\prime}(J)\mathbf{C}(t)^{-1} + J^{-\frac{2}{3}} \mathrm{DEV}\{2\partial_{\bar{\mathbf{C}}} \bar{W}^\circ[\bar{\mathbf{C}}(t)]\} \end{aligned} \tag{5.7}$$

where U° and $\bar{W}^\circ$ define the volumetric and volume-preserving contributions to the elastic stored-energy function.

The evolution of the internal variables is extended from the linear (small deformation) viscoelasticity case:

$$\begin{cases} \dot{\mathbf{Q}}_i(t) + \dfrac{1}{\tau_i}\mathbf{Q}_i(t) = \dfrac{\gamma_i}{\tau_i}\mathrm{DEV}\{2\partial_{\bar{\mathbf{C}}}\bar{W}^{\circ}[\bar{\mathbf{C}}(t)]\} \\ \lim\limits_{t\to\infty}\mathbf{Q}_i = \mathbf{0} \end{cases} \tag{5.8}$$

where τ_i is the relaxation time of each viscoelastic component, which is the ratio between viscosity and shear modulus (i.e. $\tau_i = \eta_i/\mu_i$) and γ_i is the proportion of the shear modulus of each viscous component to the instantaneous shear modulus (i.e. $\gamma_i = \mu_i/\mu_0$).

Therefore the second Piola-Kirchhoff stress can be explicitly expressed as:

$$\begin{aligned} \mathbf{S}(t) = & JU^{\circ'}(\Theta)\mathbf{C}(t)^{-1} \\ & + J^{-\frac{2}{3}}\gamma_\infty\mathrm{DEV}\{2\partial_{\bar{\mathbf{C}}}W^{\circ}[\bar{\mathbf{C}}(t)]\} \\ & + J^{-\frac{2}{3}}\sum_{i=1}^{N}\gamma_i\mathrm{DEV}\{\int_{-\infty}^{t}\exp[-(t-s)/\tau_i] \\ & \frac{d}{ds}\mathrm{DEV}\{2\partial_{\bar{\mathbf{C}}}\bar{W}^{\circ}[\bar{\mathbf{C}}(s)]\}ds\} \end{aligned} \tag{5.9}$$

More details on the derivation of the generalised Maxwell visoelasticity are presented in Appendix B. The Kirchhoff stress ($\boldsymbol{\tau} = \mathbf{F}\mathbf{S}\mathbf{F}^T$) is then given by:

$$\begin{aligned} \boldsymbol{\tau}(t) = & JU^{\circ'}(\Theta)\mathbf{1} + \gamma_\infty\mathrm{dev}\{2\partial_{\bar{\mathbf{C}}}W^{\circ}[\bar{\mathbf{C}}(t)]\} \\ & + \sum_{i=1}^{N}\gamma_i\mathrm{dev}\{\bar{\mathbf{F}}(t)\int_{-\infty}^{t}\exp[-(t-s)/\tau_i]\frac{d}{ds} \\ & \bar{\mathbf{F}}(s)^{-1}\mathrm{dev}\{2\partial_{\bar{\mathbf{C}}}\bar{W}^{\circ}[\bar{\mathbf{C}}(s)]\bar{\mathbf{F}}(s)^{-T}\}ds\bar{\mathbf{F}}(t)^T\} \end{aligned} \tag{5.10}$$

where "dev" is the deviator operator in terms of identity matrix $\mathbf{I}$: $\mathrm{dev}[\bullet] = (\bullet) - \frac{1}{3}[(\bullet) : \mathbf{I}]\mathbf{I}$.

Therefore, the deviatoric response, $\boldsymbol{\tau}_{iso} = \boldsymbol{\tau}^{\circ}_{iso} + \boldsymbol{\tau}_{vis}$, of the model is represented as:

$$\begin{aligned} \boldsymbol{\tau}_{iso} = & \gamma_\infty\mathrm{dev}\{2\partial_{\bar{\mathbf{C}}}W^{\circ}[\bar{\mathbf{C}}(t)]\} + \\ & \sum_{i=1}^{N}\gamma_i\mathrm{dev}\{\bar{\mathbf{F}}(t)\int_{-\infty}^{t}\exp[-(t-s)/\tau_i]\frac{d}{ds} \\ & \bar{\mathbf{F}}(s)^{-1}\mathrm{dev}\{2\partial_{\bar{\mathbf{C}}}\bar{W}^{\circ}[\bar{\mathbf{C}}(s)]\bar{\mathbf{F}}(s)^{-T}\}ds\bar{\mathbf{F}}(t)^T\} \end{aligned} \tag{5.11}$$

Combining the volumetric and deviatoric response, the Kirchhoff stress for the cell response is thus defined as:

$$\begin{cases} \boldsymbol{\tau}(t) = Jp\mathbf{I} + \gamma_\infty \mathrm{dev}\{2\partial_{\bar{\mathbf{C}}}\bar{W}^\circ[\bar{\mathbf{C}}(t)]\} \\ + \sum_{i=1}^{N} \gamma_i \mathrm{dev}\{\bar{\mathbf{F}}(t)\int_{-\infty}^{t} \exp[-(t-s)/\tau_i]\frac{d}{ds} \\ \bar{\mathbf{F}}(s)^{-1}\mathrm{dev}\{2\partial_{\bar{\mathbf{C}}}\bar{W}^\circ[\bar{\mathbf{C}}(s)]\bar{\mathbf{F}}(s)^{-T}\}ds\bar{\mathbf{F}}(t)^T\} \\ \\ p = \mathrm{H}(\widetilde{p}-p)\left(K_T\frac{\rho-\rho_0}{\rho_0}+\Delta p\right) \\ + \mathrm{H}(p-\widetilde{p})\left(K_C\frac{\rho-\rho_0}{\rho_0}\right) - K_C\frac{\widetilde{\rho}-\rho_0}{\rho_0} \end{cases} \tag{5.12}$$

which can be discretised as :

$$\begin{aligned} \boldsymbol{\tau}_{n+1} = J_{n+1}p_{n+1}\mathbf{I} + \sum_{i=1}^{N}\gamma_i \mathrm{dev}[\bar{\mathbf{F}}_{n+1}\tilde{\mathbf{H}}_n^{(i)}\bar{\mathbf{F}}_{n+1}^T] \\ + (\gamma_\infty + \sum_{i=1}^{N}\gamma_i \exp(-\Delta t_n/2\tau_i))\bar{\boldsymbol{\tau}}_{n+1}^\circ \end{aligned} \tag{5.13}$$

where

$$\begin{cases} p_{n+1} = \mathrm{H}(\widetilde{p}-p_{n+1})\left(K_T\frac{\rho_{n+1}-\rho_0}{\rho_0}+\Delta p\right) \\ + \mathrm{H}(p_{n+1}-\widetilde{p})\left(K_C\frac{\rho_{n+1}-\rho_0}{\rho_0}\right) - K_C\frac{\widetilde{\rho}-\rho_0}{\rho_0} \\ \rho_{n+1} = \frac{\rho_0}{J_{n+1}} \\ \tilde{\mathbf{H}}_n^{(i)} = \exp(-\Delta t_n/\tau_i)\mathbf{H}_n^{(i)} - \exp(-\Delta t_n/2\tau_i)\tilde{\mathbf{S}}_n^\circ \\ \mathbf{H}_{n+1}^{(i)} = \tilde{\mathbf{H}}_n^{(i)} + \exp(-\Delta t_n/2\tau_i)\tilde{\mathbf{S}}_{n+1}^\circ \\ \bar{\boldsymbol{\tau}}_{n+1}^\circ = \mathrm{dev}[2\bar{\mathbf{F}}_{n+1}\partial_{\bar{\mathbf{C}}}\bar{W}^\circ(\bar{\mathbf{C}}_{n+1})\bar{\mathbf{F}}_{n+1}^T] \\ \tilde{\mathbf{S}}_{n+1}^\circ = \bar{\mathbf{F}}_{n+1}^{-1}\bar{\boldsymbol{\tau}}_{n+1}^\circ\bar{\mathbf{F}}_{n+1}^{-T} \\ \tilde{\mathbf{S}}_n^\circ = \bar{\mathbf{F}}_n^{-1}\bar{\boldsymbol{\tau}}_n^\circ\bar{\mathbf{F}}_n^{-T} \end{cases} \tag{5.14}$$

The major steps and approximations involved in the discretisation process are illustrated in Appendix B.

For the surrounding tissue, the deviatoric material response was governed by the Neo-Hookean elasticity:

$$\bar{W}(\bar{\mathbf{C}}) = C_1(\bar{I}_1 - 3) \tag{5.15}$$

where, $C_1 = 2\mu$ is the Neo-Hookean deviatoric material coefficient. Thus the deviatoric Kirchhoff stress of the surrounding tissue can be expressed as:

$$\boldsymbol{\tau}^{\circ}_{iso} = 2C_1 \text{dev}(\bar{\mathbf{F}}\bar{\mathbf{F}}^T) \tag{5.16}$$

Therefore, the Kirchhoff stress for the surrounding tissue is:

$$\boldsymbol{\tau} = JK_C \frac{\rho - \rho_0}{\rho_0}\mathbf{I} + 2C_1 \text{dev}(\bar{\mathbf{F}}\bar{\mathbf{F}}^T) \tag{5.17}$$

5.2.3 Artificial viscosity

In a discretised scheme, such as in the FE method, artificial viscosity is necessary to spread the shock front over several elements so that the simulation of shock fronts (with length scale less than the mesh size) can be captured without introducing spurious oscillations. The spurious oscillation was eliminated by subtracting a certain amount of pressure p_{av} from the original pressure loading (Abaqus, 2012), where p_{av} is expressed as:

$$p_{av} = \rho l_e \dot{\epsilon_v}(b_1 c_d + l_e {b_2}^2 \dot{\epsilon_v}) \tag{5.18}$$

b_1 and b_2 are the linear and quadratic damping coefficients respectively, l_e is the characteristic element size, $\dot{\epsilon_v}$ is the volumetric strain rate and c_d is the longitudinal wave (p-wave) speed related with p-wave modulus which can be calculated from bulk modulus K and shear modulus $\mu_{eff} = \mu_\infty + \sum_{i=1}^{N} \mu_i$.

$$c_d = \sqrt{\frac{K + \frac{4}{3}\mu_{eff}}{\rho}} \tag{5.19}$$

CHAPTER 6

Simulation results

The mechanical properties of cells subject to shock waves are calibrated and validated against the experimental observations. The numerical model is applied to the three different cell lines to obtain their respective mechanical properties under shock waves. The stress and strain evolution of the cells are analysed to study the cell response in 3D. The differences in the mechanical properties of different cell lines are utilised to differentiate the resultant cell response between cancer cells and normal cells in order to achieve cancer cell-specific shock wave treatment.

6.1 Numerical model calibration and validation

The numerical model described in Chapter 5 was calibrated against the experimental observations on the area and perimeter change of the cell contour projection on the axial plane in order to find the appropriate mechanical properties of the cells under shock waves. Based on the asymmetrical deformation under compression and tension, a new EoS was proposed to model the volumetric change of a single cell subject to shock waves. This EoS captures the distinct cell response in compression and tension using two different bulk moduli and a transition pressure threshold which governs the transition between them.

The compressive bulk modulus was assumed to be 2 GPa due to the small cell deformation under compression and water content of the cell. The other two material parameters (i.e., tensile bulk modulus K_T and transition pressure threshold $\tilde{p}$) were calibrated against the experimental data by finding the least

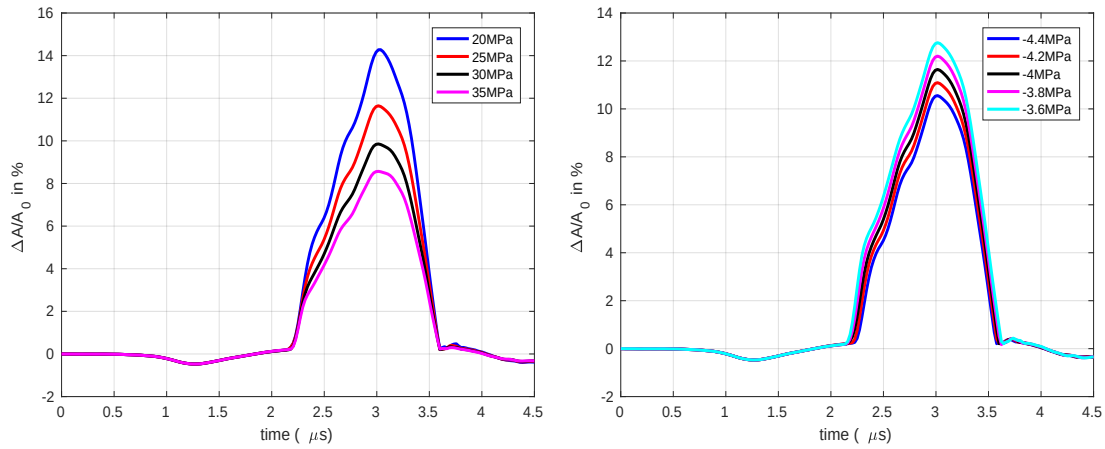

(a) (b)

Figure 6.1: (a) the influence of tensile bulk modulus on the tensile area change; the transition pressure threshold is -4 MPa for all cases; (b) the influence of the transition pressure threshold; the tensile bulk modulus is 25 MPa for all cases.

square error between the simulation and experimental results in terms of the area change for all the three shock loading conditions. It was shown that the tensile bulk modulus determines the amplitude of the tensile area change while the transition pressure threshold has an influence on both the amplitude and the duration of the tensile area change, see Figure 6.1. The calibration process was cross-validated by determining the optimal values for only two of the energy level settings at a time and testing for the "left out" (untrained) energy setting by analysing the difference between its simulation and experimental results using the previously calibrated values.

Table 6.1 lists the cross-validation results for each cell line, including different training combinations, resultant calibration values and error between simulation and experimental results in the untrained data set. It is shown that the calibration process of the numerical model presents a mean error around 12% for all cell types, which is acceptable considering the small compressive deformation and the experimental variation, see Figure 4.3. This discrepancy between simulation and experimental results may influence the difference between CAKI-2 and HK-2 or HRE cells observed in the experiment (Figure 4.4). However, the pattern of the maximum area change of the simulation results among different cell lines at three shock wave energy levels remained similar to the experimental results, see Figure 6.2.

Table 6.1: Cross-validation of the numerical model for the three cell lines.

Cell type	Trained settings	Optimal K_T	properties $\tilde{p}$	Untrained setting	error	mean error
HRE	Lvl 4 & Lvl 6	20 MPa	-4.6 MPa	Lvl 8	6.8%	
	Lvl 4 & Lvl 8	25 MPa	-4.4 MPa	Lvl 6	17.9%	
	Lvl 6 & Lvl 8	20 MPa	-5.2 MPa	Lvl 4	12.4%	12.4%
HK	Lvl 4 & Lvl 6	20 MPa	-4.6 MPa	Lvl 8	7.7%	
	Lvl 4 & Lvl 8	20 MPa	-4.6 MPa	Lvl 6	9.5%	
	Lvl 6 & Lvl 8	19 MPa	-4.4 MPa	Lvl 4	19.8%	12.3%
CAKI	Lvl 4 & Lvl 6	22 MPa	-4.4 MPa	Lvl 8	13.7%	
	Lvl 4 & Lvl 8	35 MPa	-4 MPa	Lvl 6	8.1%	
	Lvl 6 & Lvl 8	35 MPa	-3.8 MPa	Lvl 4	14.1%	12.0%

Table 6.2: Material properties of three different cell lines.

volumatric properties	cell type	compressive bulk modulus K_C	tensile bulk modulus K_T	transition pressure $\tilde{p}$
	CAKI-2	2 GPa	34 MPa	-4 MPa
	HK-2	2 GPa	20 MPa	-4.6 MPa
	HRE	2 GPa	25 MPa	-4.6 MPa
deviatoric properties		long-term shear modulus μ_∞	viscoelastic shear modulus μ_1	viscosity η_1
Rebelo et al. (2013) Jérusalem and Dao (2012)		3.1 kPa	0.34 kPa	69.6 Pa.s

During the calibration process, the influence of deviatoric material properties (shear moduli and viscosity) on the cell response (i.e., area and perimeter change) was found insignificant (a factor change of 10^6 in the deviatoric properties resulted in <0.01% of area or perimeter change). This further confirms that the cell response is dominated by the volumetric change which is consistent with the experimental findings. The volumetric mechanical properties for each cell line were computed by simultaneously calibrating them across the three shock wave energy levels and the deviatoric material properties were obtained from the literature (Jérusalem and Dao, 2012; Rebelo et al., 2013), see Table 6.2. The bulk modulus of the surrounding extracellular matrix was assumed to be similar to water ($K = 2$ GPa) and the shear modulus was obtained from the literature (Leclerc et al., 2012), $\mu = 3.45$ kPa.

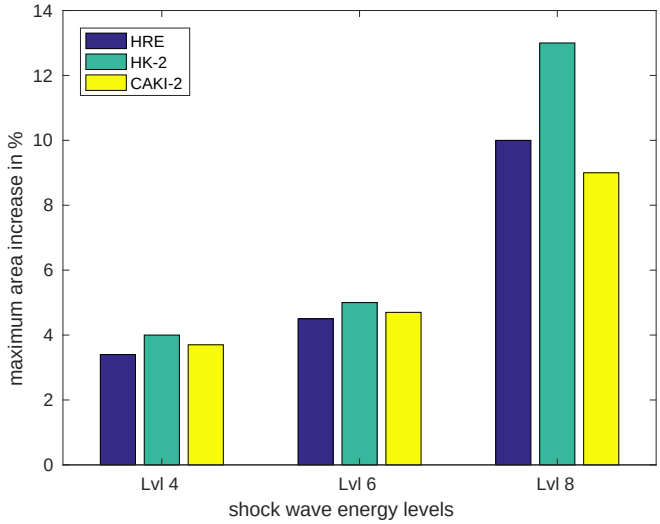

Figure 6.2: The maximum area increase for the three cell types at three shock wave energy levels: (blue) HRE cells; (green) HK-2 cells and (yellow) CAKI-2 cells.

The comparison between the validated simulation results and experimental observations on area and perimeter change for each cell line are respectively presented in Figures 6.3 and 6.4. It can be seen that the simulation results and experimental measurements are in good agreement (∼12% error). However, this discrepancy between experimental and simulation results does not mask the difference between cell lines observed in the experiment (both the maximum area increase and tensile duration).

The bulk moduli and transition pressure between HK-2 and HRE cells were similar while a relatively large difference was found from CAKI-2 cells. The resulting mechanical properties also demonstrate that even though the cancer cells have the largest bulk modulus, the lower transition pressure threshold make them the first to deform largely during tension.

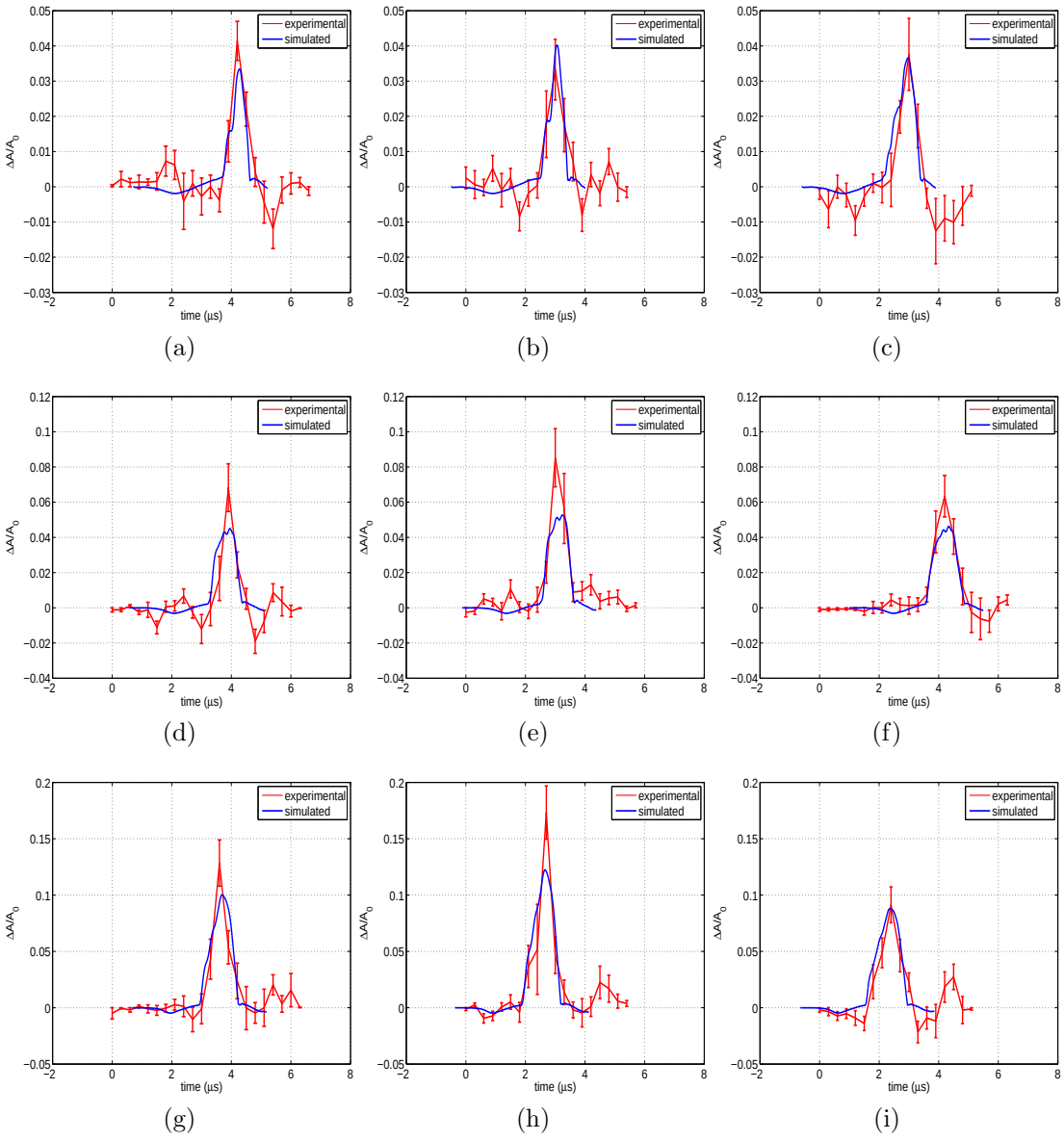

Figure 6.3: Experimental (red) and simulation (blue) results of cell area change in response to shock waves. The cell deformation at shock wave energy levels: (a)-(c) level 4, (d)-(f) level 6, (g)-(i) level 8 for HRE, HK-2 and CAKI-2 cells respectively.

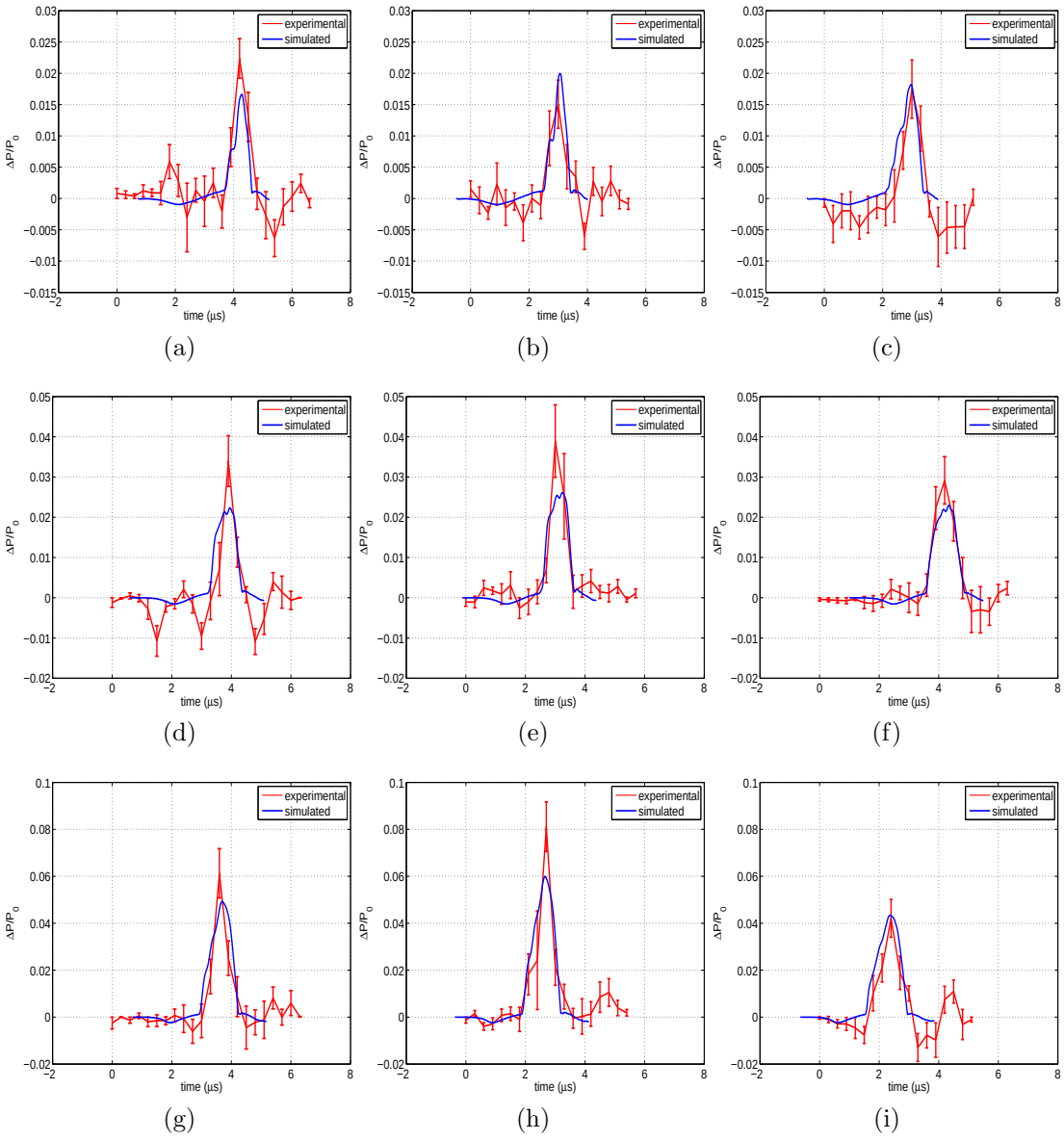

Figure 6.4: Experimental (red) and simulation (blue) results of cell perimeter change in response to shock waves. The cell deformation at shock wave energy levels: (a)-(c) level 4, (d)-(f) level 6, (g)-(i) level 8 for HRE, HK-2 and CAKI-2 cells respectively.

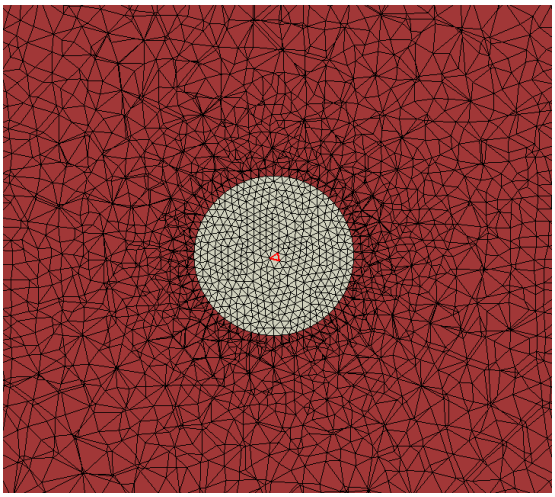

Figure 6.5: Pressure measurement location at the centre of the cell model.

6.1.1 Quantification of stress and strain evolution of cells

With the numerical model, cell response can be quantified in terms of stress and strain evolution in 3D which helps to better study the shock wave interactions with cells. Figure 6.6 shows the comparison of the pressure waveforms obtained at the centre of each cell models (as shown in Figure 6.5) at the three shock wave energy levels.

The pressure profile among the three cell lines were found to be similar (the variation was less than 7% at energy level 4, 3% at energy level 6 and 5% at energy level 8). This shows that the shock wave pressure is not strongly influenced by the difference in the mechanical properties of the cells. The von Mises stress, which quantifies the amount of shearing in the model, was found to be in the order of 100 Pa using the deviatoric mechanical properties from the literature.

The overall cell membrane strain, which describes the area change of the cell membrane, was also analysed as an indicator of cell membrane permeability. The membrane strain was calculated from the change of the surface area during and before shock wave loading. The surface area at any time point was estimated as the sum of the triangular area A_i formed by the three nodes of the vertex of an

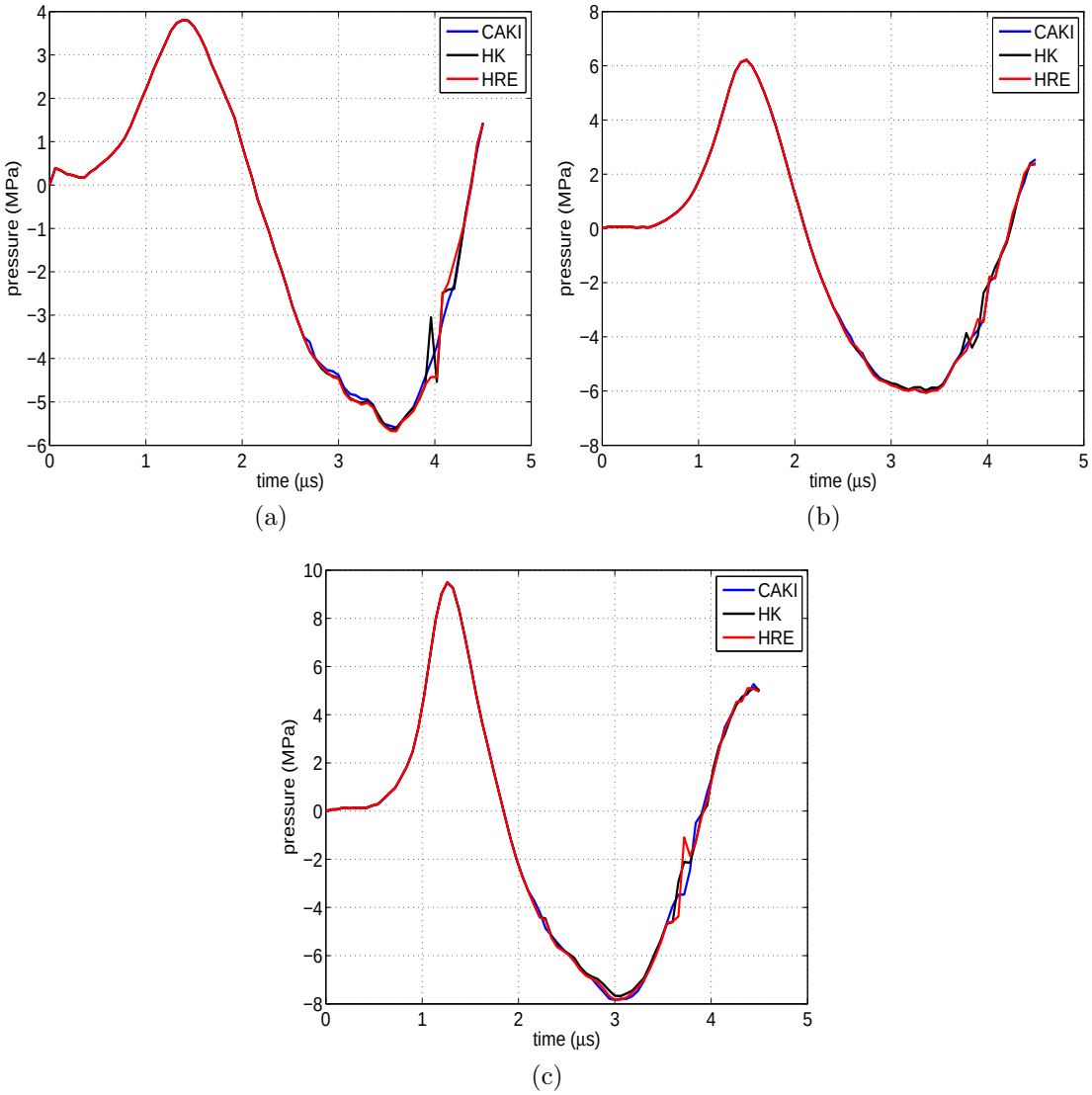

Figure 6.6: Comparison of the pressure measured in the centre of the cell model of the three cell lines at shock wave energy levels: (a) level 4; (b) level 6; (c) level 8. Three colours represent three cells lines: CAKI-2 cells (blue); HK-2 (black) and HRE (red).

element i on the cell membrane.

$$\frac{\Delta S}{S_0} = \frac{\sum_{i=1}^{N} (A_i(t) - A_i(0))}{\sum_{i=1}^{N} A_i(0)} \tag{6.1}$$

The membrane strain in each cell line at different shock wave energy levels are

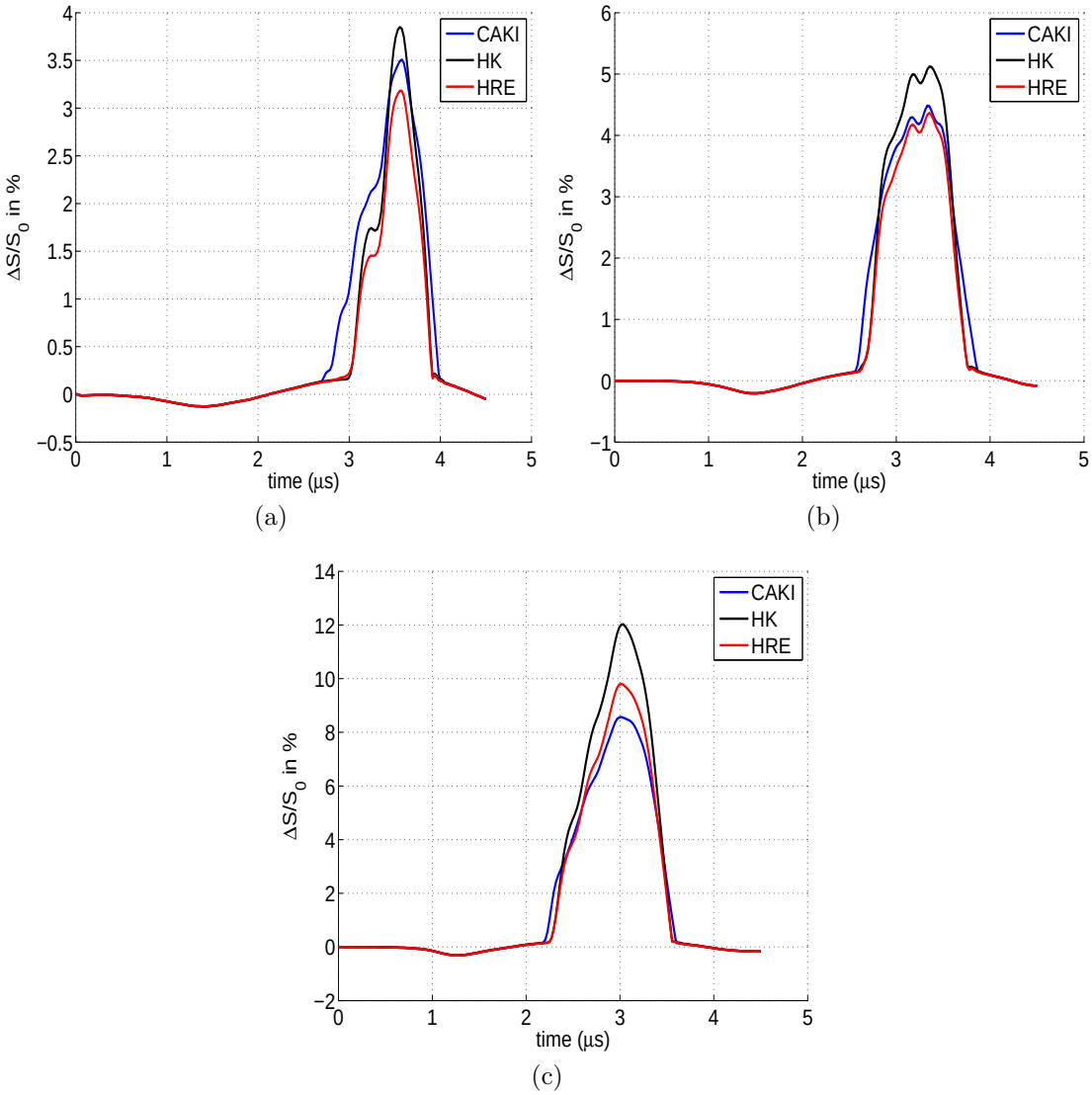

Figure 6.7: The overall cell membrane strain of the three cell lines at shock wave energy levels: (a) level 4; (b) level 6; (c) level 8; CAKI-2 cells (blue); HK-2 (black) and HRE (red).

compared in Figure 6.7. The results showed greater variation than the pressure waveforms. The maximum membrane area expansion under tension reached up to 10% in HRE, 12% in HK-2 and 8.5% in CAKI-2 cells at shock wave energy level 8.

6.1.2 Optimisation of shock wave loading

The validated numerical model allows for designing shock wave profiles to elicit a specific cell response. For example, by utilising the difference of the transition pressure thresholds between cell types, a shock wave with a tensile stress that is on the order of 4.5 MPa will exceed the transition threshold of cancer cells but not healthy cells and therefore could sonoporate or even rupture cancer cells without damaging normal cells. Figure 6.8 presents the proposed shock wave profile with a peak negative pressure of 4.59 MPa and the predicted membrane strain of the three cell types. It can be seen that the difference in the transition pressure threshold for CAKI-2 and HRE (HK-2) cells resulted in a 1.1% of membrane strain in CAKI-2 cells at the peak negative pressure while that of HK-2 and HRE cells remained less than 0.2%. The rupture strain threshold for cancer cells have been reported between 3% and 5% (Weiss, 1992; Weiss et al., 1985), therefore with 1.1% of tensile membrane strain, increased cell membrane permeability may be expected on cancer cells even though permanent damage may not be achieved. On the other hand, the influence on the normal cells is negligible.

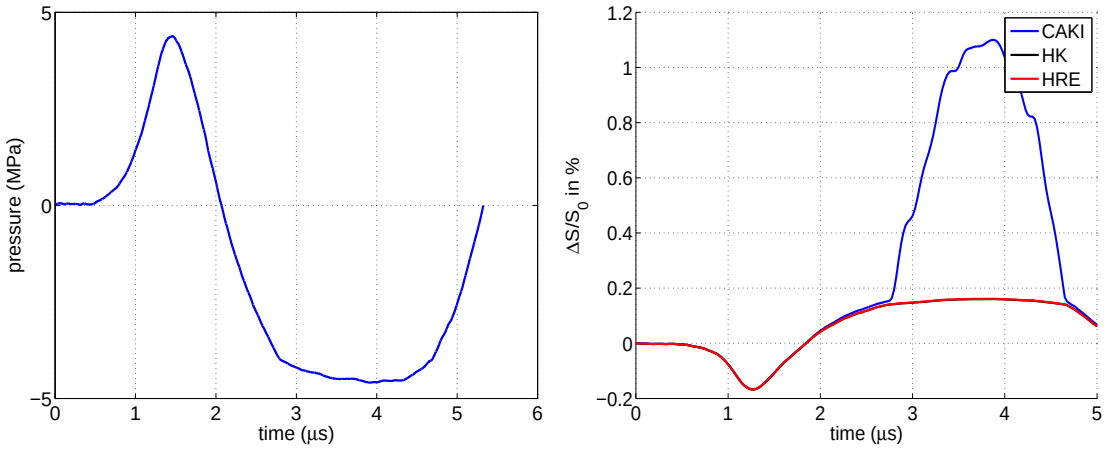

(a) (b)

Figure 6.8: (a) Proposed shock loading waveform with a maximum tensile pressure of 4.59 MPa which is larger than the transition pressure threshold of CAKI-2 cells but not HK-2 or HRE cells; (b) comparison of the resulting cell membrane strain in different cell models. Three colours represent three cells lines: CAKI-2 cells (blue); HK-2 (black) and HRE (red). A difference in cell membrane area change during shock waves can be distinguished between CAKI-2 and the other cell lines.

Research studies have also shown that the rupture strain threshold is 40% or

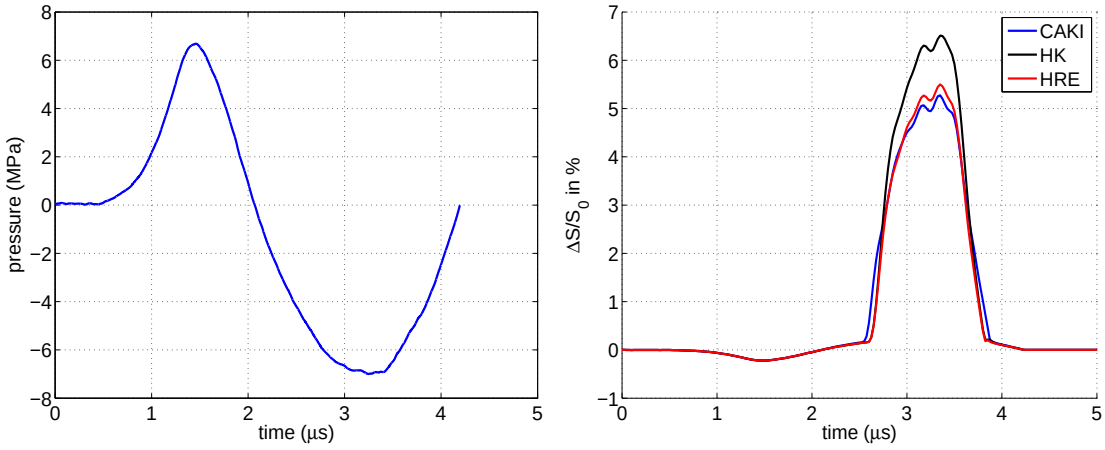

(a) (b)

Figure 6.9: (a) Proposed shock loading waveform with a maximum tensile pressure of 7 MPa which is expected to result in cancer cell rupture (>5% of surface area increase); (b) comparison of the resulting cell membrane strain in different cell models. Three colours represent three cells lines: CAKI-2 cells (blue); HK-2 (black) and HRE (red). The cell membrane area change are found similar in all the cell type (5-6%), which is higher than cancer cell rupture strain (3-5%) but lower than that of normal cells (∼40%).

higher for normal cells (Li et al., 2013; Shigematsu et al., 2015). Therefore another shock loading with the peak negative pressure of 7 MPa was proposed, see Figure 6.9(a), which is expected to result in rupture of cancer cells (>5% membrane area increase). In this case, the non-cancerous cells (HK-2 and HRE cells) showed relatively large deformation during tension (∼5.5% and 6.5% respectively) which, however, are still well below the reported rupture threshold for normal cells. In addition the expansion in cancer cell was longer in duration compared to their non-cancerous counterparts (HK-2 and HRE cells), which may lead to higher energy deposition for damaging cancer cells.

6.2 Discussion

The experimental observation showed that the cells responded differently to compression and tension, therefore a modified acoustic EoS was proposed to describe this behaviour using a bilinear bulk modulus governed by a transition pressure threshold. It is also shown that the transition pressure threshold is similar to the cavitation threshold in tissue, which is often reported at several MPa (Krasovitski et al., 2011; Child et al., 1990). The numerical model showed that the influence of deviatoric material properties in the simulation was insignificant for all cell types, suggesting that under the current boundary conditions (i.e., a single cell held within a 3D matrix and subject to a shock wave) the volumetric deformation overwhelms the shearing effects of the shock wave.

The difference in the mechanical properties for different cell types was found not to strongly influence the shock wave propagation, but may differentiate the resultant membrane strain. *In silico* optimisation of shock wave profiles was performed to differentiate the tensile response between invasive cancer cells (CAKI-2 cells) and their noncancerous counterparts (HK-2 and HRE cells) in order to achieve cancer-specific bioeffects (sonoporation or cell damage). A designed shock wave loading was proposed to result in potential permeabilisation of cancer cells while its effects on noncancerous cells remained minimal. Another proposed artificial shock loading led to cancer cell damage with a resultant membrane strain larger than the rupture strain threshold of cancer cells, however, the resultant membrane strain of noncancerous cells was still well below their rupture threshold.

CHAPTER 7

Influence of cell size, shape, orientation and neighbouring cluster on single cell response to shock waves

Numerical studies are performed to analyse the influence of cell size, shape, orientation and neighbouring cells on the single cell response to shock waves. The cell models are built based on the statistics of cell morphology obtained from both bright field and fluorescent microscopic images. It is shown that the cell size, shape and orientation do not have significant impact on the single cell deformation under shock waves, whilst clusters of connected cells increase the shock wave effects.

In Chapters 3-6, the shock wave interaction with a single cell embedded in a tissue-mimicking phantom was analysed and modelled. However, the representative cell used in the model had an ideal spherical shape which will not be the case *in vitro* or *in vivo*. There are two goals for this Chapter. The first one is to study how realistic cell geometries affect the cell response to shock waves. The second goal is to understand how cell response differs if it is placed within a cell cluster rather than an isolated cell.

7.1 Influence of intrinsic cell characteristics

7.1.1 Experimental and numerical setup

The HK-2 cell line, described in Section 3.1.1, was used in this study. The cells were cultured in a sterile-out environment (Ryan et al., 1994). The tissue-mimicking phantom was made of a mixture of 0.6% purified agarose solution and DMEM cell media. The tissue phantom was held in a 12-well plate with a thickness of less than 5mm for imaging purpose. Bright field imaging was used to study cell size distribution and multiphoton microscopy (MPM) was used to obtain the detailed real cell geometries in 3D.

7.1.1.1 Bright field imaging

An inverted optical microscope (Nikon, Eclipse Ti) was used with a 40× microscopic objective to image individual HK-2 cells embedded in the tissue phantom in order to study the cell size distribution. Trypan blue solution (Sigma-Aldrich Ltd.) was used to identify dead cells which were selectively coloured by the assay, see Figure 7.1. This was to ensure that only live cells were analysed.

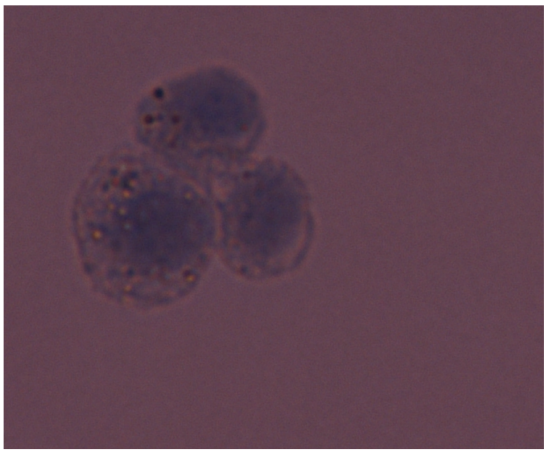

Figure 7.1: Dead cells labelled by trypan blue.

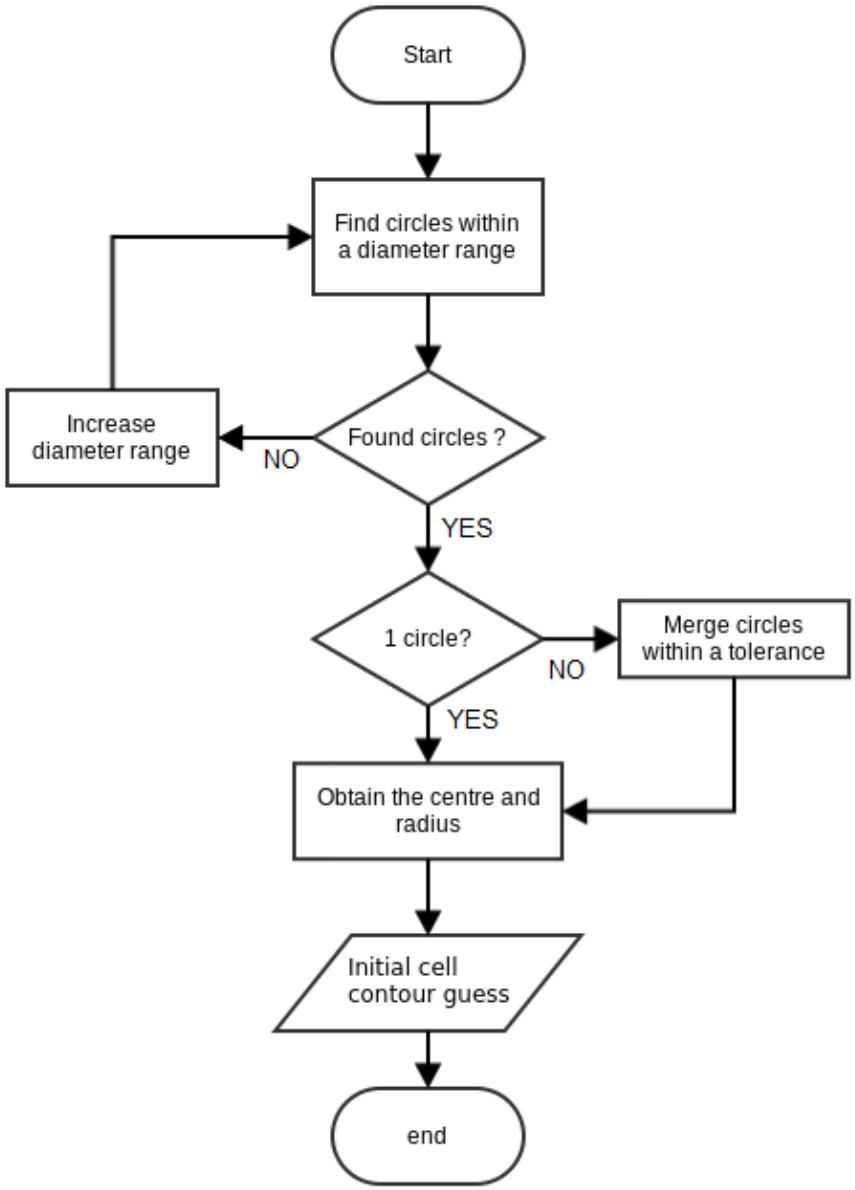

Figure 7.2: Main procedures to obtain the initial guess of cell contours based on circle detection algorithm.

7.1.1.2 Cell contour analysis

The cell contour was analysed with an automatic cell detection algorithm based on circle detection and active segmentation algorithms. The detection algorithm is adapted from a MATLAB circle detection algorithm (MathWorks) which detects any shape similar to a circle. Small circles detected close to the cell contour due to image quality were merged together. The working principle of the detection

algorithm is presented in Figure 7.2. The algorithm estimates the initial guess of the cell contour as an input fed into the active contour segmentation algorithm (see Section 3.2). An example of a segmented cell is shown in Figure 7.3.

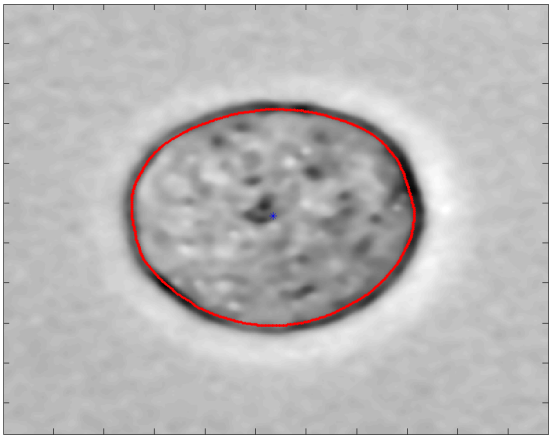

Figure 7.3: Segmented contour of a cell image taken in bright field (40× magnification).

7.1.1.3 Multiphoton microscopy

MPM uses two or more low-energy photons excitation to cause higher energy electronic transition in a fluorescent molecule, which allows for high resolution and high contrast fluorescent images in thick samples (Svoboda and Yasuda, 2006). In a focussed laser, fluorophores are excited almost exclusively in a small diffraction-limited focal volume. By scanning over the specimen, a stack of fluorescent images is generated.

A nuclear acid stain (Hoechst 33342, Life Technologies) and a plasma membrane stain (Cellmask, Life Technologies) were used to label the cell nucleus and cortex membrane, respectively. Each tissue sample in the 12-well plate was submerged with the diluted Cellmask solution with 1.5× concentration in the incubator for 30 minutes to allow the staining solution to diffuse through the gel matrix. The staining solution was then replaced with the Hoechst staining solution with concentration of 0.2 µg/mL after washing the sample three times with a physiologically relevant buffer. The samples were then incubated for another 30 minutes for the cell nucleus to be labelled.

In the experiment I took stacks of 512×512 pixels images of three different HK-2 cells embedded in the tissue phantom with an image slice interval of 300

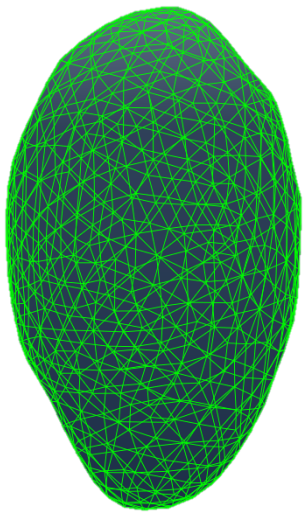

Figure 7.4: Cell model based on a real HK-2 cell geometry.

nm in each stack.

7.1.1.4 Numerical models

For each MPM fluorescent slice, the cell membrane was semi-automatically segmented based on the intensity threshold using Amira (Ami, 2014), a commercial 3D software for visualisation and meshing. The 3D volume of the cell was thus rendered and meshed in Amira. An example of a constructed cell model based on real cell fluorescent images is shown in Figure 7.4.

The extracellular environment was generated to surround the cells by reorganising the associated nodes in the mesh using Abaqus (FE software) and automatic scripts in Python and MATLAB (see Figure 7.5).

Shock wave profiles (see Figure 7.6) applied to the top surface of each cell models were the single shock measured using a FOPH inside the agarose tissue phantom at three different shock wave energy levels in Figure 4.1.

Cell size variability: To study the effect of cell size, three spherical cell models with different radii were constructed to compare their resultant cell responses. The cell model sizes were selected based on the cell size distribution analysis: the smallest and largest radii as well as the mean value of the measured data were used to represent the three distinctive cases in the distribution.

Cell shape variability: The influence of the cell shape was studied by

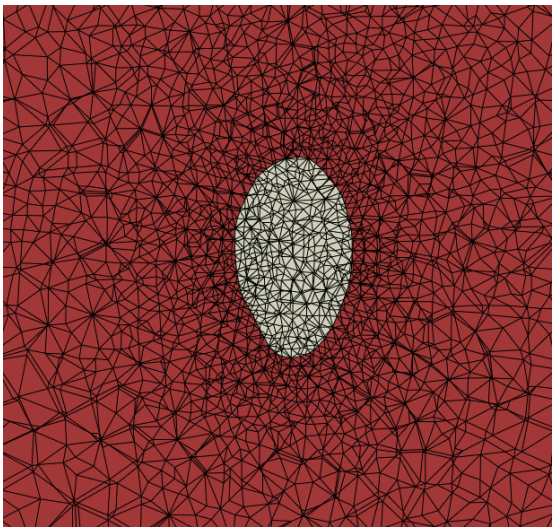

Figure 7.5: Cross-section of a single cell finite element model based on real cell geometry.

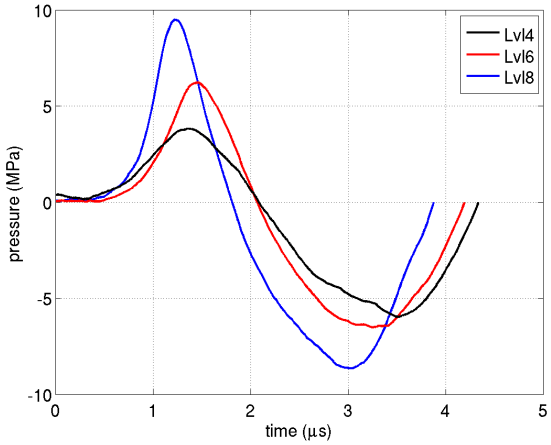

Figure 7.6: Shock wave pressure profiles measured inside agarose tissue phantom using a FOPH. Different colors represent the pressure profile at different shock wave energy levels.

reconstructing the cell models from the MPM images of the three different individual cells. The cell response from different cell models were compared with each other and with that of the spherical model with an averaged radius. The three cell models constructed from real cell geometries are presented in Figure 7.7.

Cell orientation variability: In order to study the influence of the cell orientation, one of the reconstructed cell models (cell sample 2) was rotated by

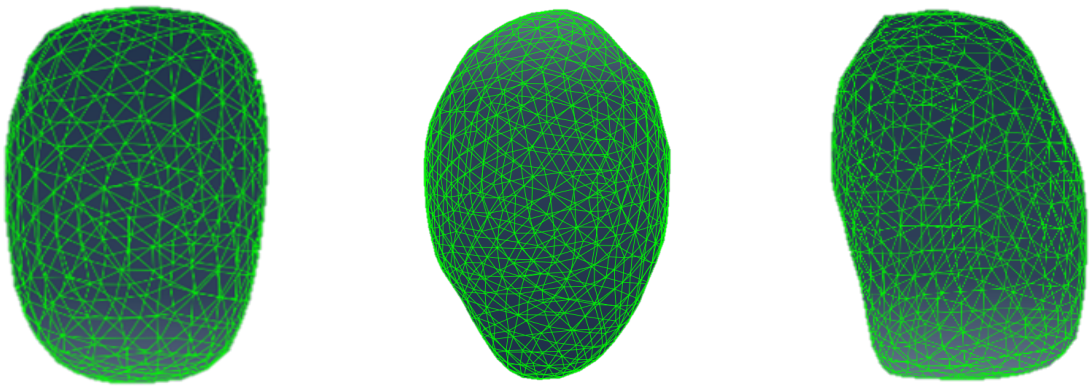

(a) (b) (c)

Figure 7.7: Cell models constructed from real HK-2 cell geometries. (a) sample 1; (b) sample 2; (c) sample 3

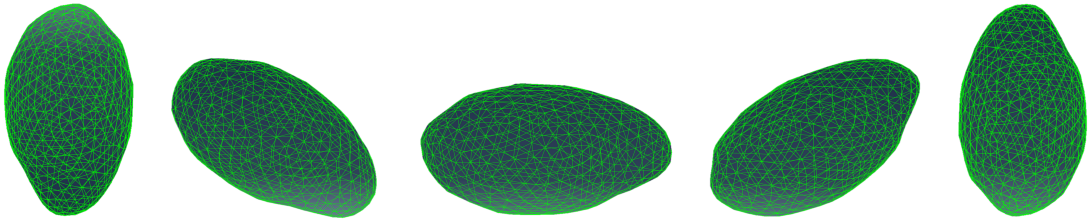

(a) (b) (c) (d) (e)

Figure 7.8: Cell model constructed from sample 2 with varying orientations: (a) 0°, (b) 45°, (c) 90°, (d) 135° and (e) 180°

45°, 90°, 135° and 180° (see Figure 7.8).

The same material framework (i.e., nonlinear viscoelasticity for the deviatoric response and EoS using bilinear bulk moduli for compression and tension for the volumetric response) and model boundary conditions used in Chapter 5 were applied here as the goal of this Chapter is only to assess the geometrical influence on the cell response to shock waves.

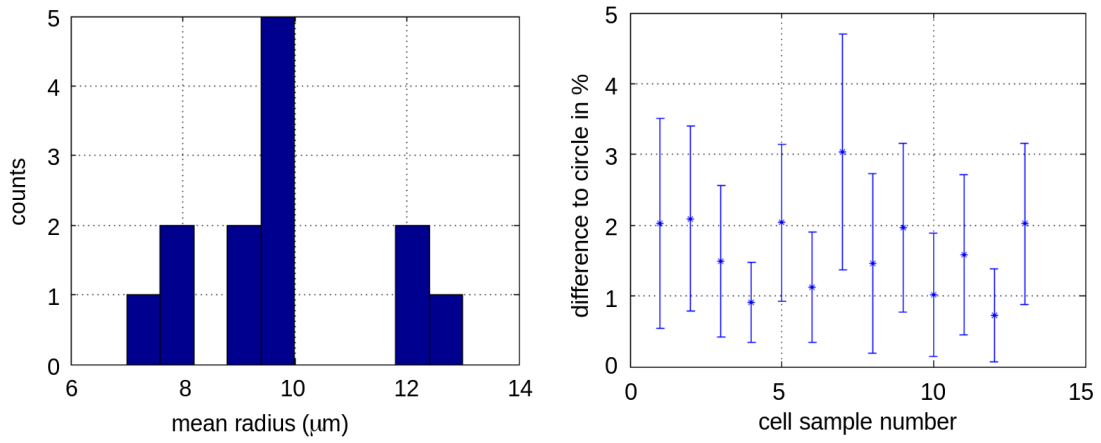

(a) (b)

Figure 7.9: (a) the histogram of cell size distribution; (b) approximation error of cell contour to a circle.

7.1.2 Experimental and simulation results

7.1.2.1 Influence of cell size

The cell radius is defined as the mean distance between all the points on the cell contour and the centre of mass in each bright field cell image. As shown in Figure 7.9(a), cell sizes ranged from 7.5 µm to 13 µm with the median value around 10 µm.

The deviation of the cell radius was also analysed to define the similarity of the cell contour to a circle in each sample. The deviation is defined by comparing measured cell radius of each point on the contour, r_i, to the radius of a circle with the same cell area, $r_c = \sqrt{\frac{A}{\pi}}$. Figure 7.9(b) shows that the maximum approximation difference of the measured cell contour to a circle is less than 5%, indicating a spherical or ellipsoidal shape of cells in agarose gel.

Three spherical cell models were thus constructed using the smallest (7.5 µm), largest (13 µm) and the median (10 µm) mean radii measured in the experiment (Figure 7.9(a)).

Figures 7.10-7.12 show the comparison of the cell response due to different cell sizes at the three shock wave energy levels. The cell response was analysed in terms of pressure propagation for volumetric response, von Mises stress for shearing evaluation and membrane strain for therapeutic applications. The pres-

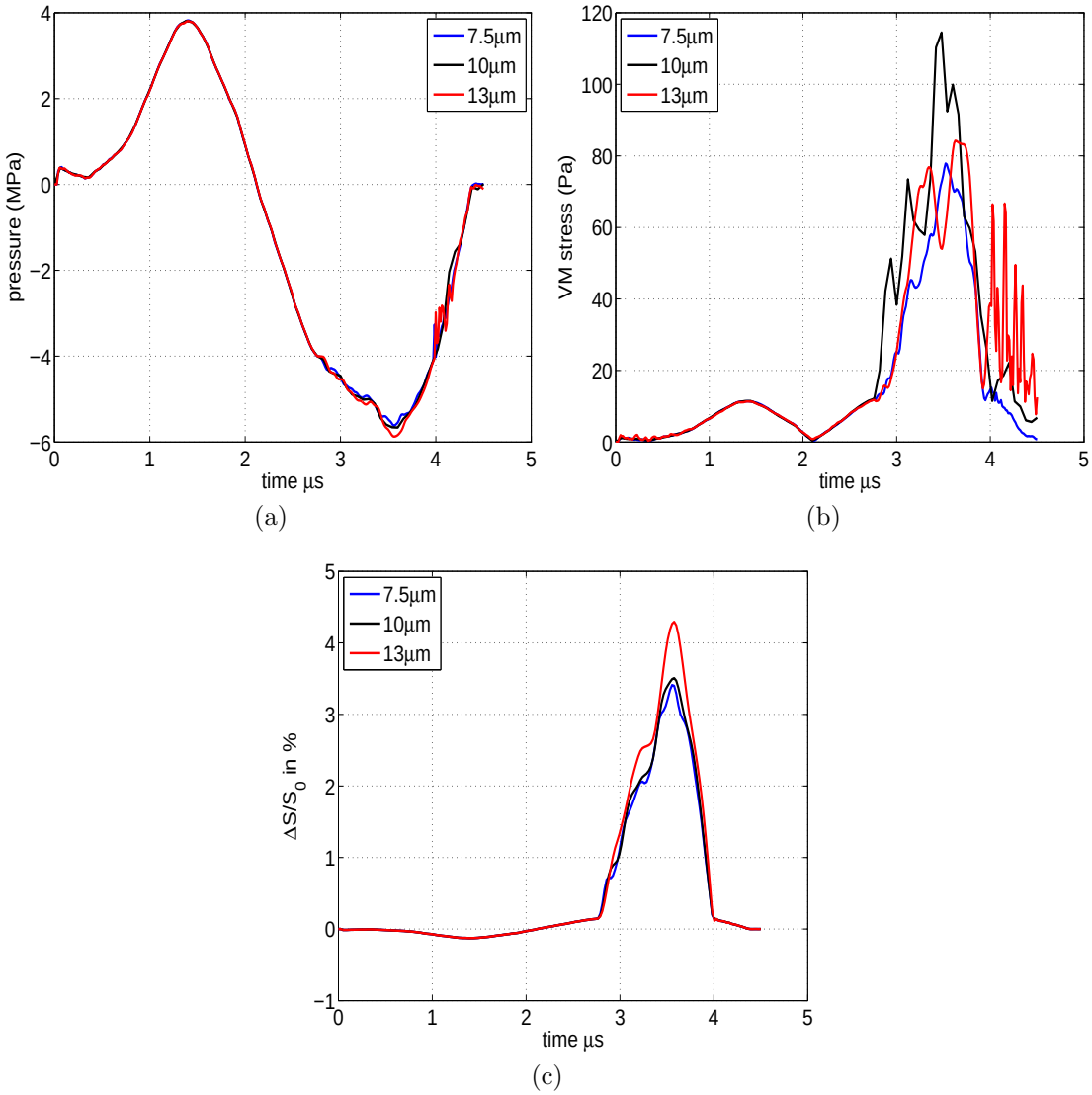

Figure 7.10: At shock wave energy level 4, cell response for different cell sizes. (a) pressure waveform measured at the cell model centre; (b) von Mises stress measured at the distal part of the cell; and (c) membrane strain.

sure was measured at the centre of the cell model and the von Mises stress was measured at the cell membrane equator where the maximum von Mises stress was found. The membrane strain was defined as the change of membrane area over time.

In general, the increased shock wave energy levels resulted in higher stress and strain in cells, revealing a maximum tensile membrane strain of 4% in the 13 µm cell model at shock wave energy levels 4, 5% at level 6 and 10% at level

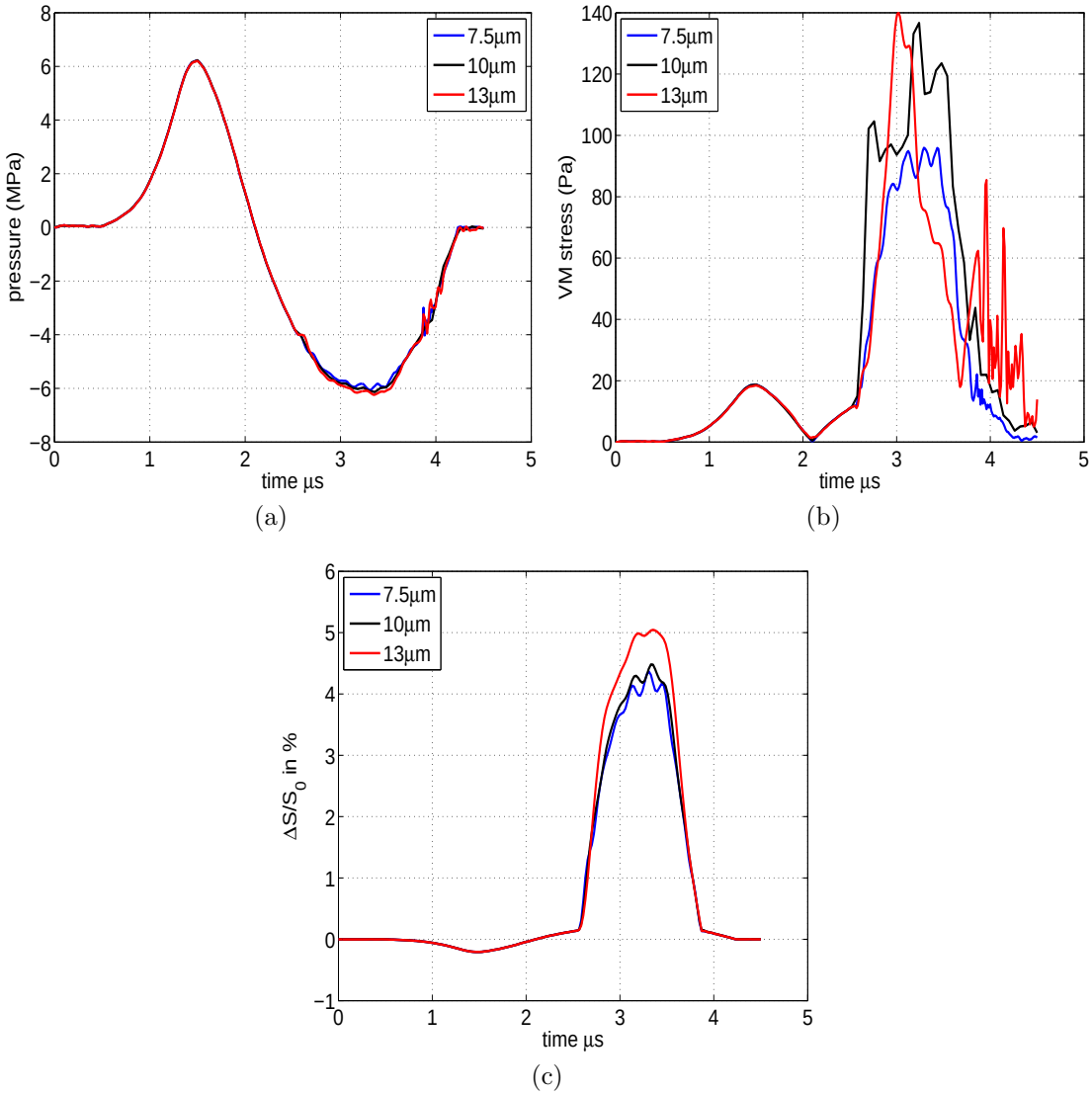

Figure 7.11: At shock wave energy level 6, cell response for different cell sizes. (a) pressure waveform measured at the cell model centre; (b) von Mises stress measured at the distal part of the cell; and (c) membrane strain.

8. However, the difference found in the cell response due to cell sizes was not significant, and the difference was not strongly influenced by the shock wave settings: at all shock wave energy levels, the maximum variation among the three cell models in tensile pressure and membrane strain increase were around 5% and 15% respectively. The von Mises stress in each cell models was found to be in the order of 100 Pa with variations less than 25%.

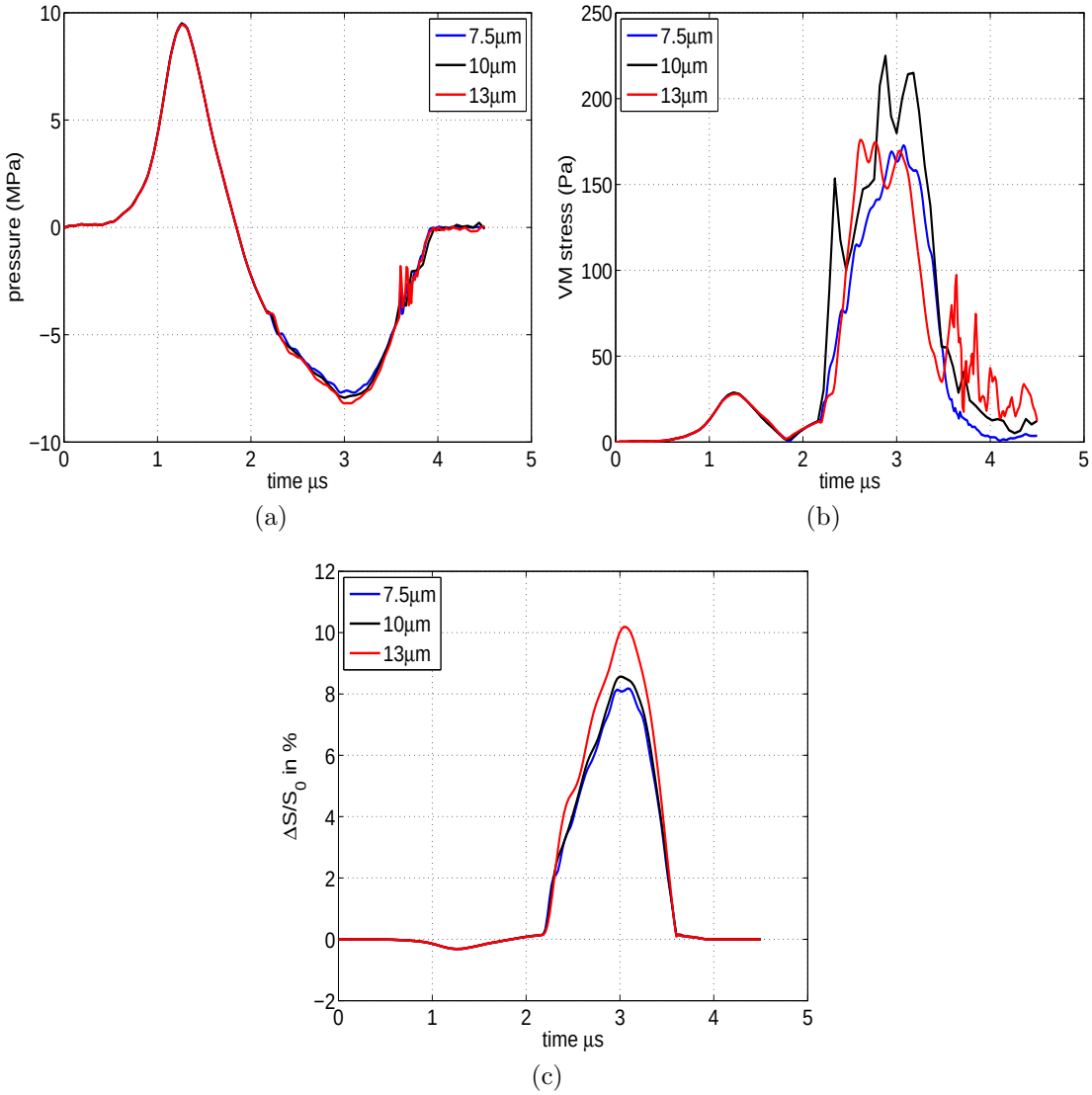

Figure 7.12: At shock wave energy level 8, cell response for different cell sizes. (a) pressure waveform measured at the cell model centre; (b) von Mises stress measured at the distal part of the cell; and (c) membrane strain.

7.1.2.2 Influence of cell shape

Four cell models representing three different real cell shapes and a spherical shape were used to study the effect of cell shapes on cell response to shock waves. Similar to the influence of cell sizes, the cell shape variability showed similar influence on cell response at different shock wave energy levels. Therefore, only the cell response at shock wave energy level 6 (medium level) is presented to illustrate the influence of cell shape on cell response. The cell response was also analysed in

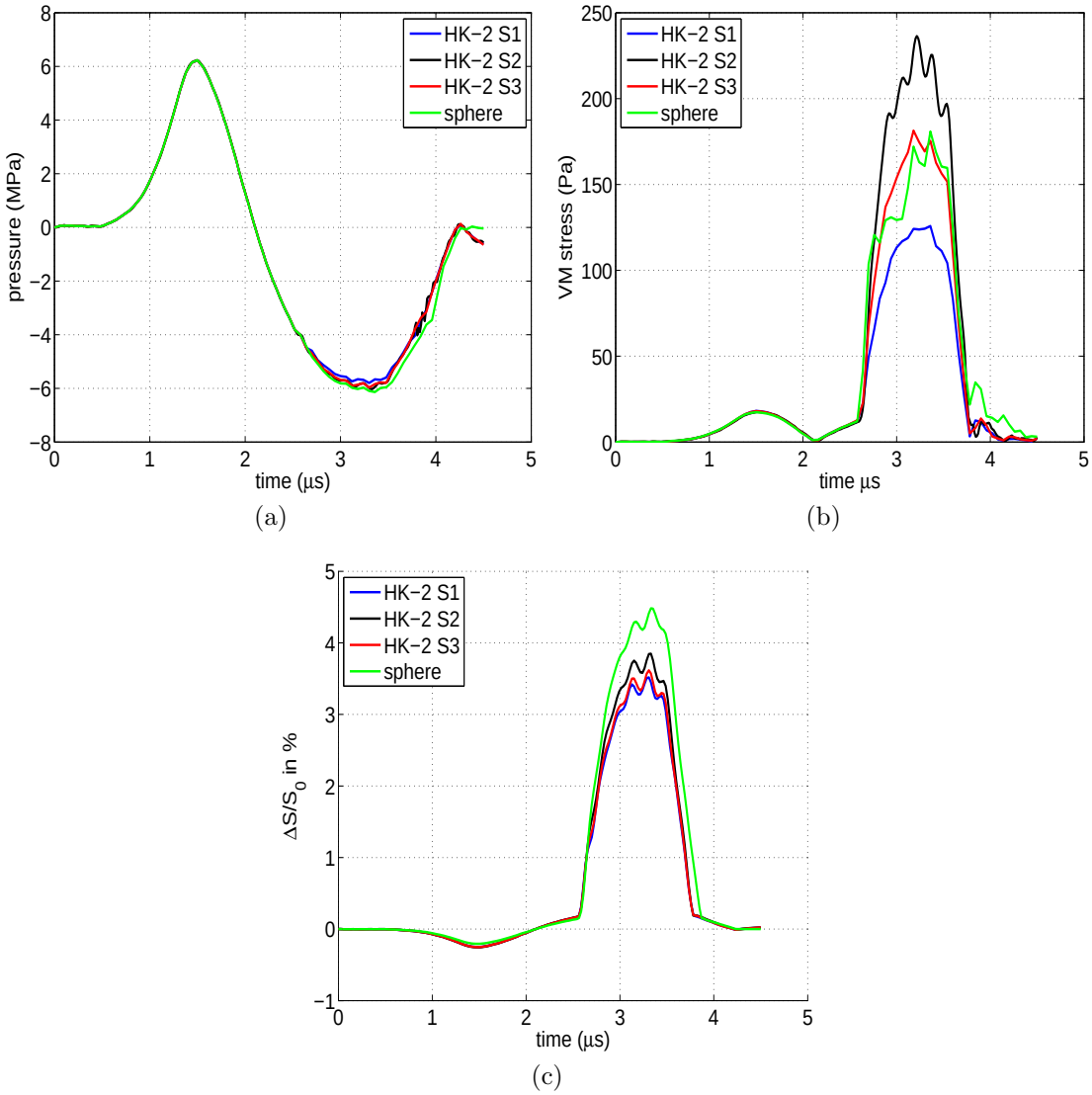

Figure 7.13: Cell response due to the influence of cell shapes. (a) pressure waveform measured at the cell model centre; (b) von Mises stress measured at the distal part of the cell; and (c) membrane strain.

terms of pressure propagation, von Mises stress and overall cell membrane strain.

Figure 7.13(a) compares the pressure profiles measured at the cell centre in each cell geometry. No significant difference (maximum of ∼7%) was found in the pressure waveforms between each cases. The comparison of von Mises stress at the distal part of each cell model (away from the shock wave source) where the shape changes most dramatically is presented in Figure 7.13(b). The difference of von Mises stress observed during the tensile phase in each cell model may be due to the

cell curvature at the cell bottom as the highest von Mises stress was found in the HK-2 cell sample 2 which has the smallest curvature radius (see Figure 7.7(b)). Additionally, the HK-2 cell sample 1 exhibiting the flattest bottom showed the lowest value of the von Mises stress. Figure 7.13(c) shows similar membrane strain in different real cell models: the membrane strain found in the real cell models (i.e., HK-2 cell sample 1-3) was around 3.5% with a variation of less than 5%. The spherical model showed a larger surface strain (∼4.5%) which deviated from the mean surface strain of real cell models by 15%.

7.1.2.3 Influence of cell orientation

The influence of the cell orientation was studied by comparing the cell response in different cell models with a range of angular orientations. The pressure profiles at the cell centre, the von Mises stresses at the cell bottom and the cell membrane strain measured at shock wave energy level 6 are shown in Figure 7.14. The cell response was consistent with the findings in the cell shape analysis: the von Mises stresses were related to the model curvature at the measurement point, therefore the cell model rotated by 90° showed the smallest value of von Mises stress while the largest value was found in the nonrotated state. The pressure propagation and surface strain showed variations of less than 1% and 2%, respectively, indicating no significant difference under the effect of model orientations.

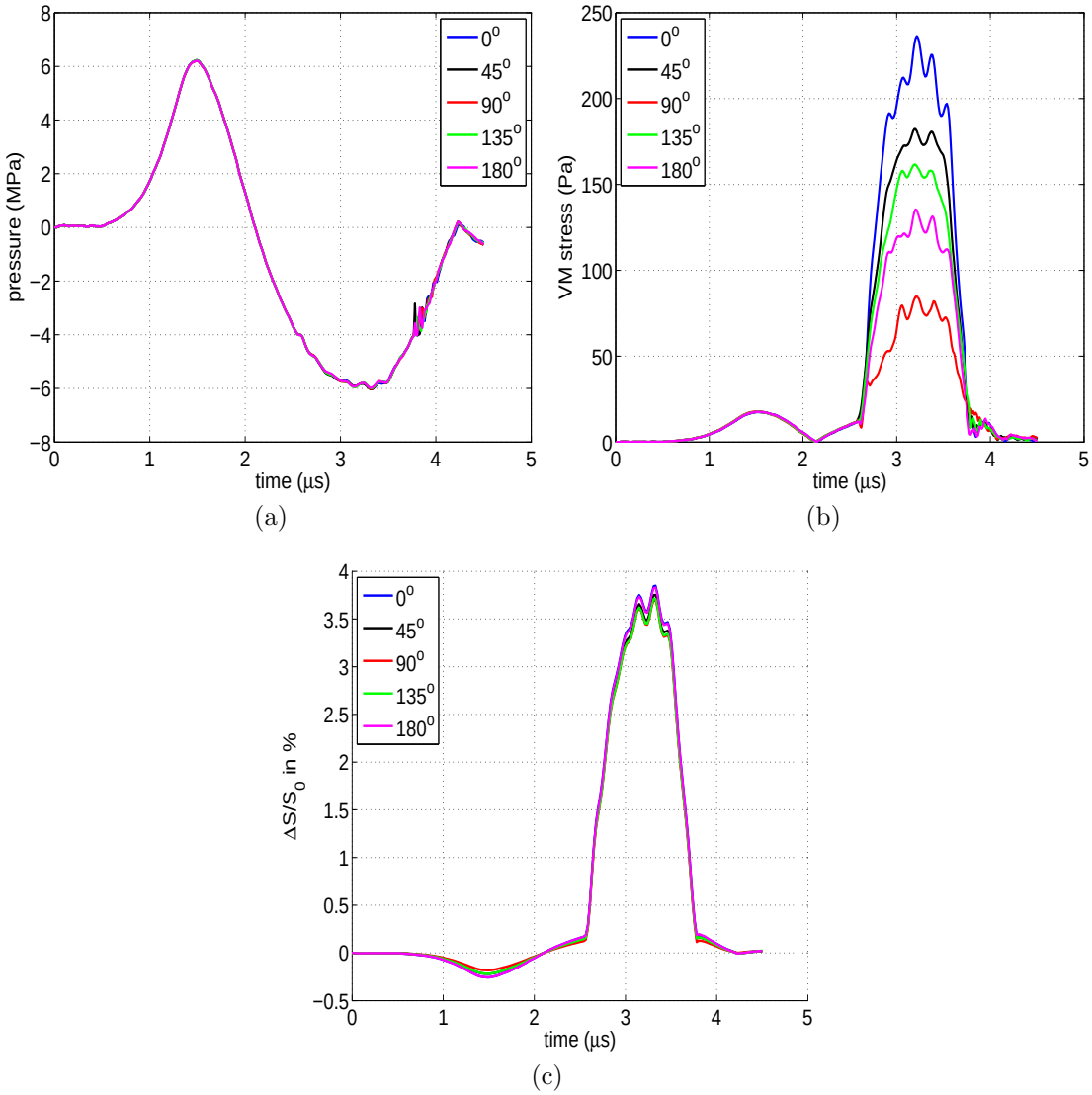

Figure 7.14: Cell response in each orientation model. (a) pressure waveform measured at the cell model centre; (b) von Mises stress measured at the distal part of the cell; and (c) membrane strain.

7.2 Influence of neighbouring cell cluster

Individual cells embedded in the tissue-mimicking phantom may not realistically represent those inside tissue or tumour. Therefore 3D cell culture has been progressively used as *in vitro* systems to study tumour biology as such system better preserves the specific biochemical and morphological features of the corresponding tissue *in vivo* (Kunz-Schughart et al., 2002). Therefore, it is important to evaluate the cell response to shock waves inside a 3D cell culture system (i.e., a

cell cluster) and compare it to that directly inside a tissue-mimicking phantom.

7.2.1 Model construction

The creation of the cluster model was inspired by the generation of polycrystalline structures in superalloys (Cruzado et al., 2015). An open source program, Neper (R. Quey, 2011) was used to generate a Voronoi tessellation assembling for the cell cluster in a spherical domain of a diameter of 250 µm. Figure 7.15 shows the spheroid model with each embedded cell coloured. The comparison of the cell morphology and structure between a cell monolayer and the cross-sectional view of the spheroid model is presented in Figure 7.16. The spheroid model was tuned to preserve the nonspherical cell shape and the variations in cell sizes.

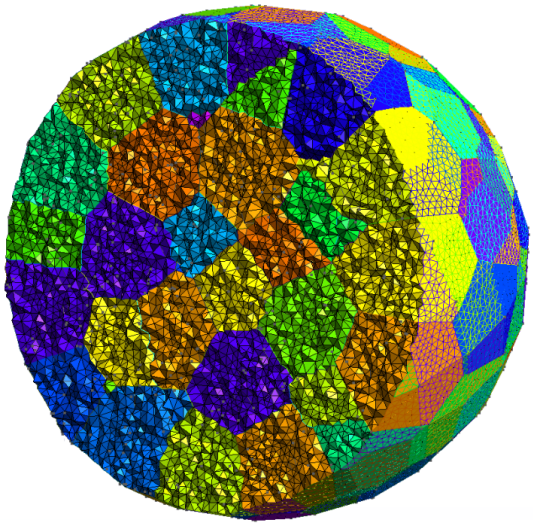

Figure 7.15: A cut view of the spheroid model. Each coloured domain represents a cell.

The spheroid model was split into a number of submodels constructed layer by layer around the central single cell in order to study the effect of each layer of neighbouring cells on the centre cell response, see Figure 7.17. In the full cluster model (Figure 7.17(f)), a representative cell in each ring layer was selected to study the cell response distribution at different parts of the cluster model, see Figure 7.18.

A model mimics a tumour environment was built by modelling the most outer 2-3 layers with the mechanical properties of normal healthy (HRE) cells while

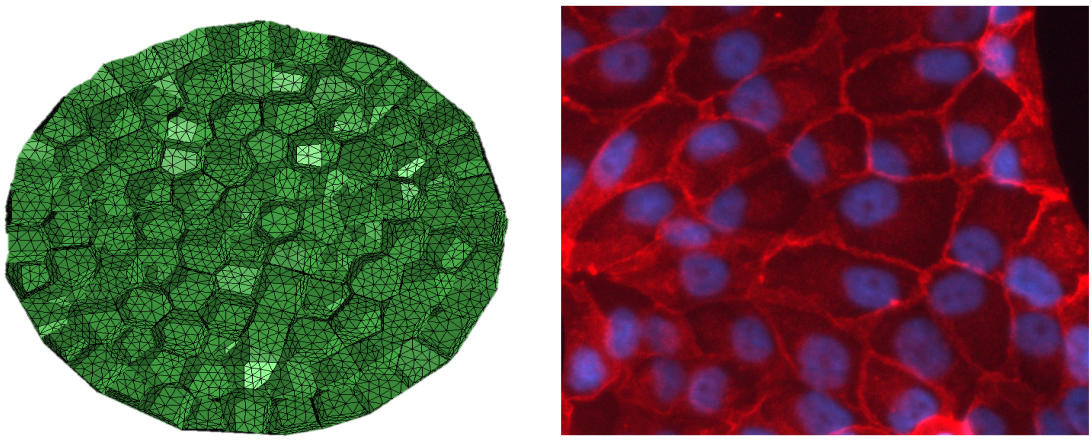

(a) (b)

Figure 7.16: Comparison of the spheroid model structure to the monolayer cluster fluorescent image. (a) cross-sectional view of the spheroid model; (b) a fluorescent image of the monolayer cluster.

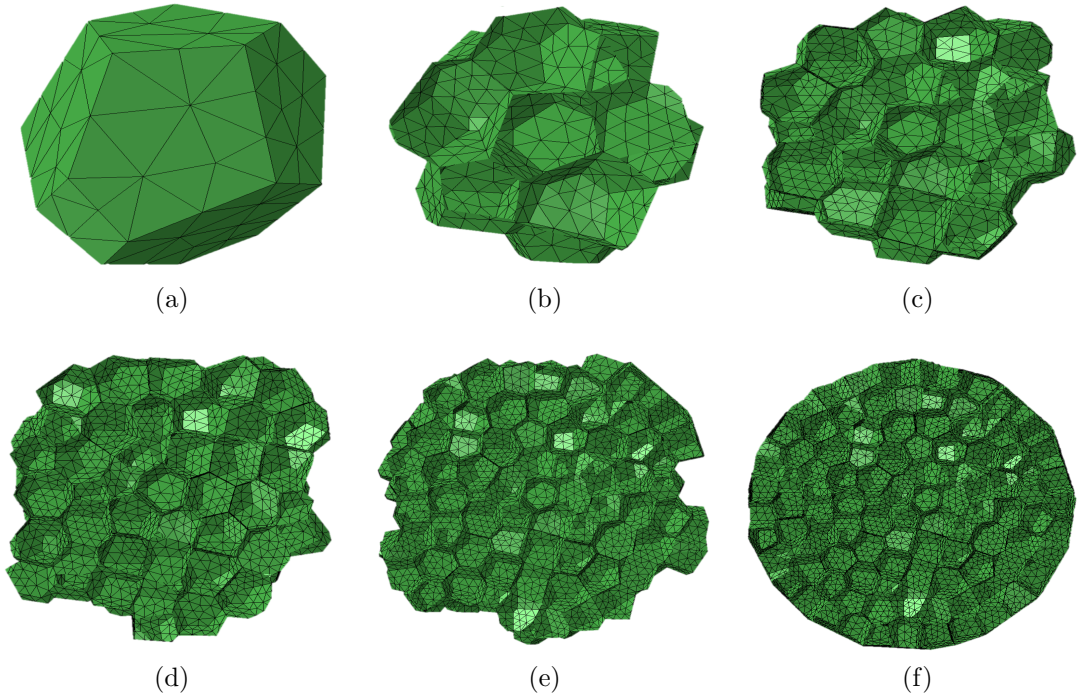

(a) (b) (c)

(d) (e) (f)

Figure 7.17: Spheroid models by layers. (a) no surrounding layers; (b) with one surrounding layer; (c) with two surrounding layers; (d) with three surrounding layers; (e) with four surrounding layers; (f) full spheroid model (with 5-6 surrounding layers).

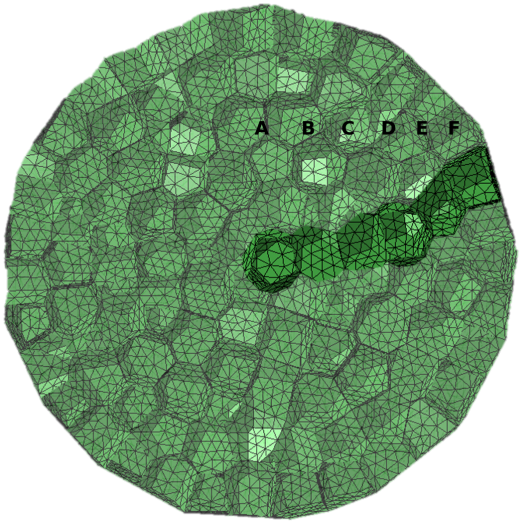

Figure 7.18: The full spheroid model with the representative cell for each surrounding layers highlighted. From A to F: centre cell to the representative cell at layer five.

the inner spheroid was represented by cancer (CAKI-2) cells (see Figure 7.19). As shown in Chapter 6, two shock wave profiles were designed to achieve cancer cell specific bioeffects by utilising the difference in mechanical properties between individual cancer cells and their noncancerous counterparts, see Figures 6.8 and 6.9. It is also important to extend the study of designing shock wave profiles for cancer cell-specific effects into a multicellular spheroid environment.

7.2.2 Simulation results

7.2.2.1 The response of the central cell

The central cell response simulated at shock wave energy level 6 with the presence of each ring layer of neighbouring cells (Figure 7.17) is presented in Figure 7.20. Pressure peaks (up to 35 MPa) were observed with the presence of neighbouring layers during the shock wave tensile phase. Due to the bilinear bulk properties of the cells in the cluster, the cells changed from soft to stiff states during the late part of the tensile wave where the pressure passed the transition pressure threshold again before returning to zero. The sudden increase of bulk stiffness may thus result in a high acceleration of the cell wall deformation which then generated a secondary shock wave (i.e., pressure peaks observed). The detailed

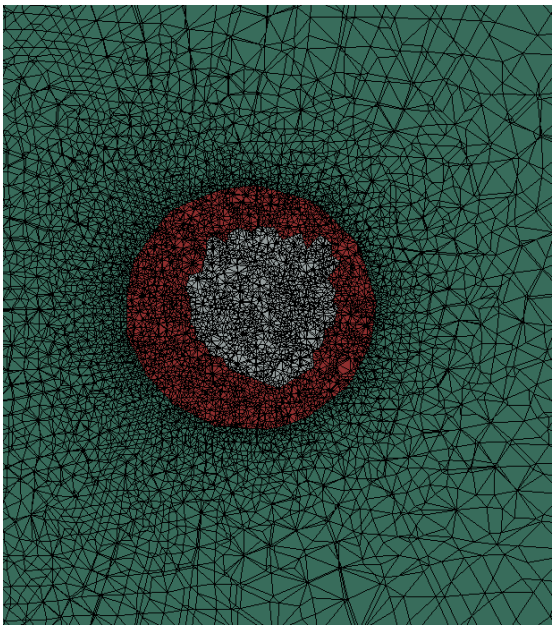

Figure 7.19: A spheroid model with differentiated inner cluster of cancer cells (white) and the surrounding normal cells (red). The spheroid is embedded in the surrounding 3D matrix (green).

explanation is provided in Section 7.2.2.4.

The presence of neighbouring cell layers also resulted in an increase of von Mises stress and membrane strain in comparison to that of an isolated cell embedded in the tissue phantom. A convergence was found in the change of membrane strain with more than three surrounding layers, revealing around 8% membrane strain increase compared to 2.5% in the no-surrounding layers case. The large pressure spikes did not influence the major membrane area change (membrane area expansion to $\sim$8%) but led to a small membrane area decrease ($\sim$0.5%) after it.

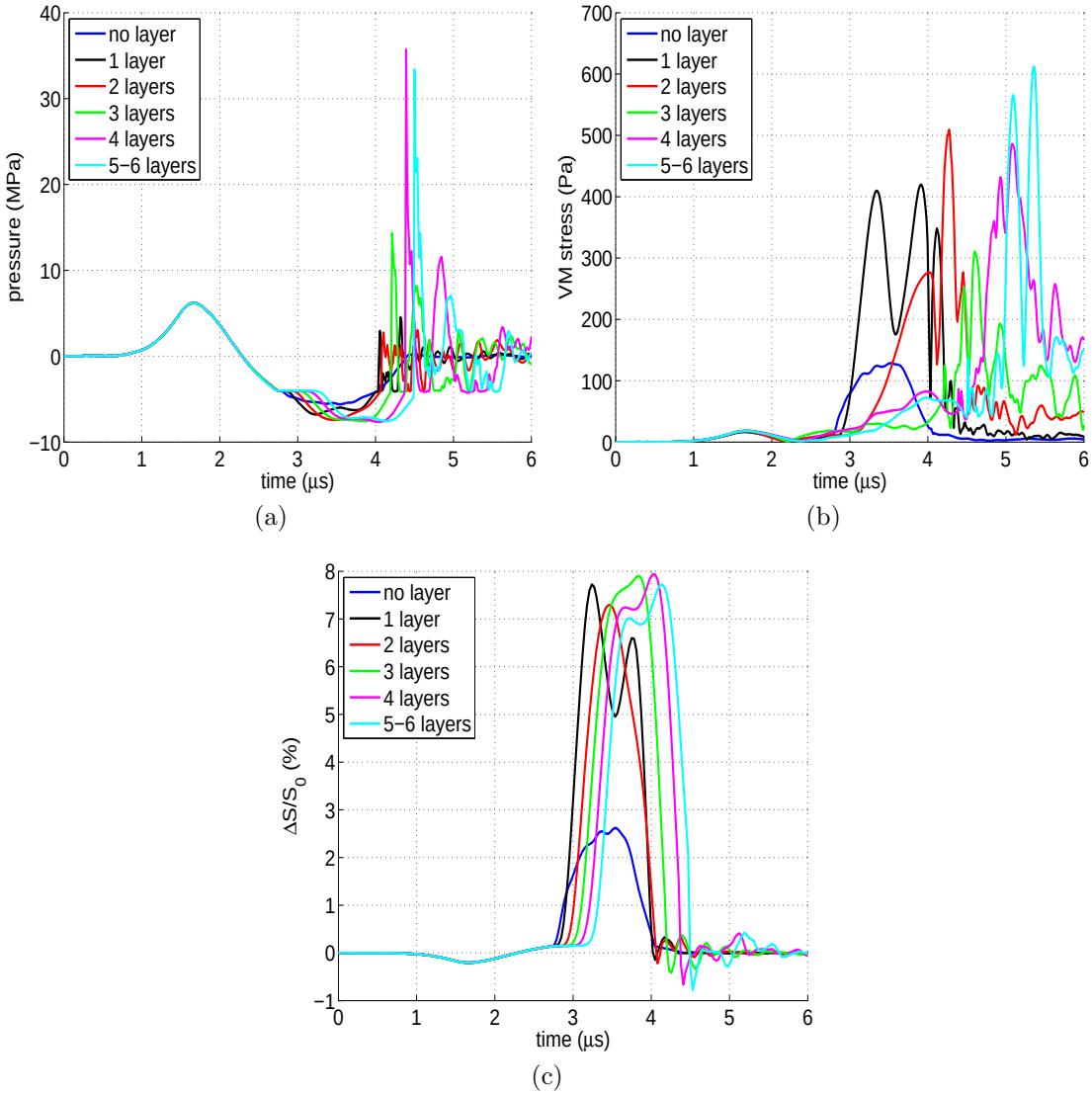

Figure 7.20: Central cell response for different cluster sizes. (a) pressure waveform measured at the cell model centre; (b) von Mises stress measured at the distal part of the cell; (c) overall membrane strain.

7.2.2.2 The response of the representative cell of each ring layer

Figure 7.21 shows the cell response of the representative cell of each ring layers in the full spheroid model (Figure 7.18). Both pressure propagation and membrane strain showed relatively homogeneous distribution in the spheroid as the measured waveforms were similar in different representative cells. A higher value of von Mises stress (∼600 Pa) was found in the spheroid centre compared to the surrounding layers (∼200 Pa). This may be caused by not only the geometrical

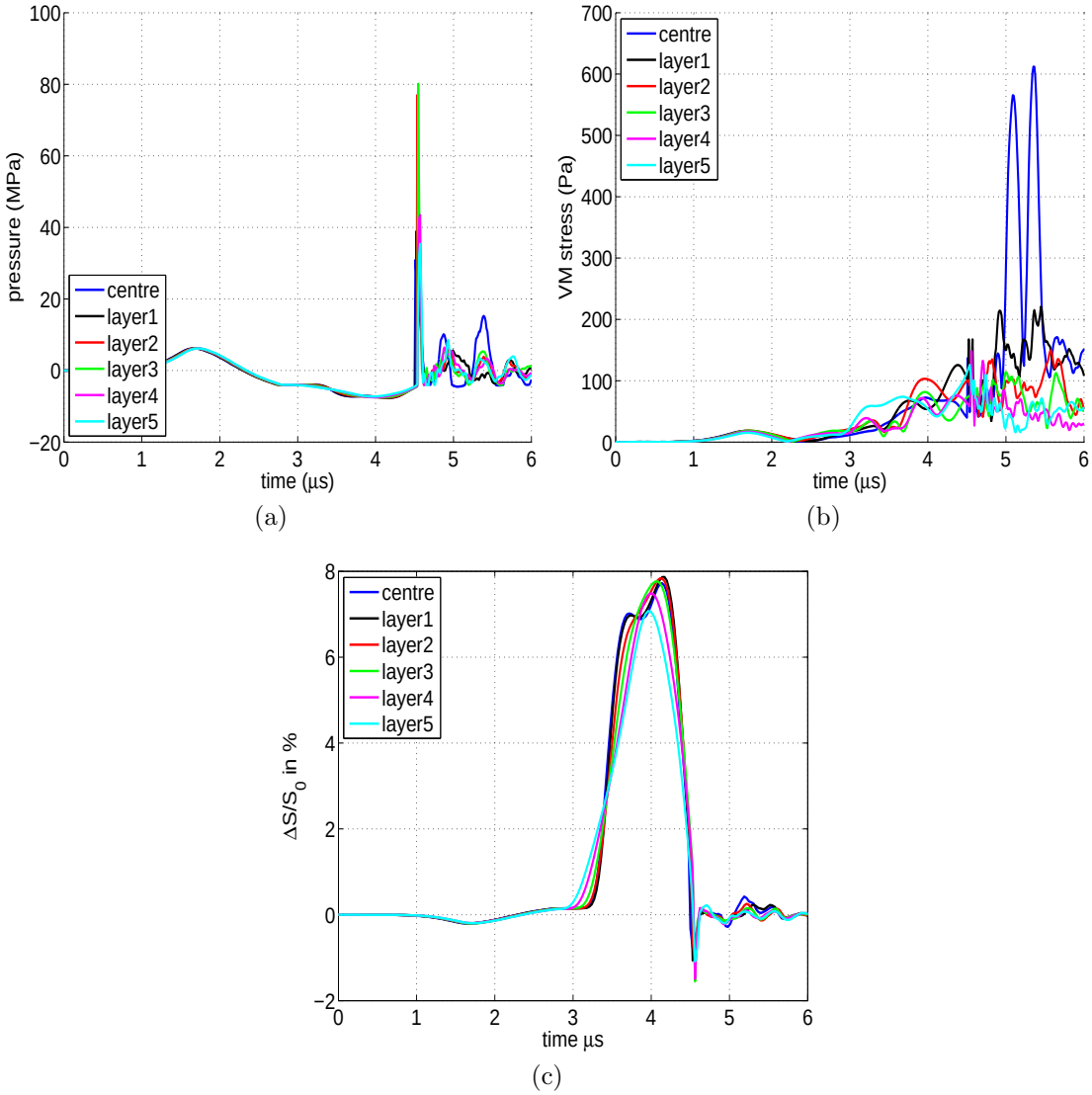

Figure 7.21: Cell response simulated at the representative cell in each surrounding ring layer. (a) pressure waveform measured at the cell model centre; (b) von Mises stress measured at the distal part of the cell; (c) overall membrane strain.

effect but also the accumulative interference of stress waves propagating in the spheroid.

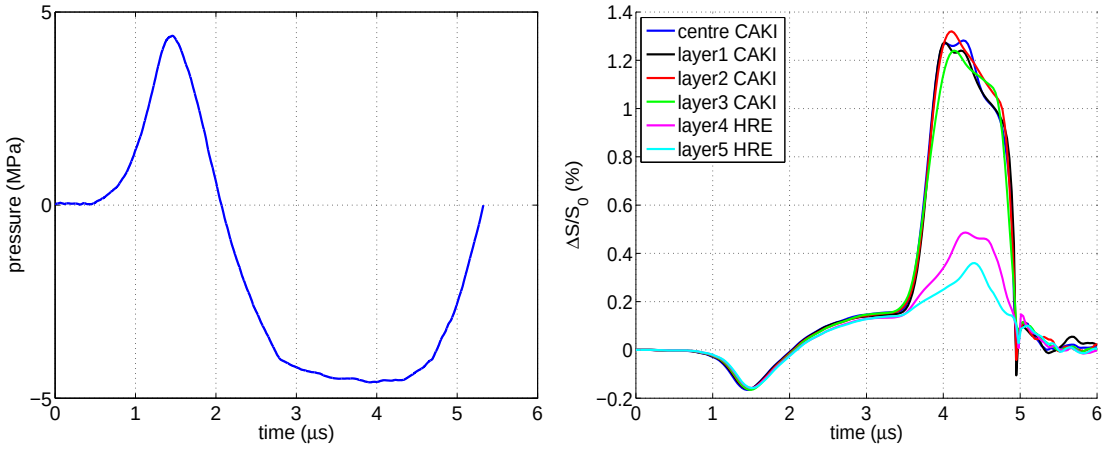

(a) (b)

Figure 7.22: (a) Applied artificial shock wave profile. (b) membrane strain measured at each representative cells in the spheroid model.

7.2.2.3 Multicellular spheroid response

Figure 7.22 shows the first shock wave profile shown in Section 6.1.2 and its resultant membrane strain at each layer of the multicellular spheroid. Compared to the response of individual cancer cells (CAKI-2 cells) and normal healthy cells (HRE cells) in the agarose tissue phantom (Figure 6.8(b)), the multicellular spheroid model results showed an increase of the membrane strain in both CAKI-2 (from 1.1% to 1.3%) and HRE cells (from <0.2% to ∼0.4%). The difference between the cancerous and non-cancerous cells was still preserved.

The second shock wave profile which aims at resulting in more than 5% of membrane strain in individual cancer cells was also tested in the multicellular spheroid model. The results are shown in Figure 7.23(b). The cell cluster showed an increased membrane strain compared to the single cell case: the measured maximum membrane area change was around 9% in the cell cluster while that in the single cell model was around 5-6%. The resultant membrane strain may still lead to cancer cell rupture without damaging the surrounding normal cells as it exceeds the rupture strain threshold of cancer cells (3-5%) but not that of normal cells (∼40%).

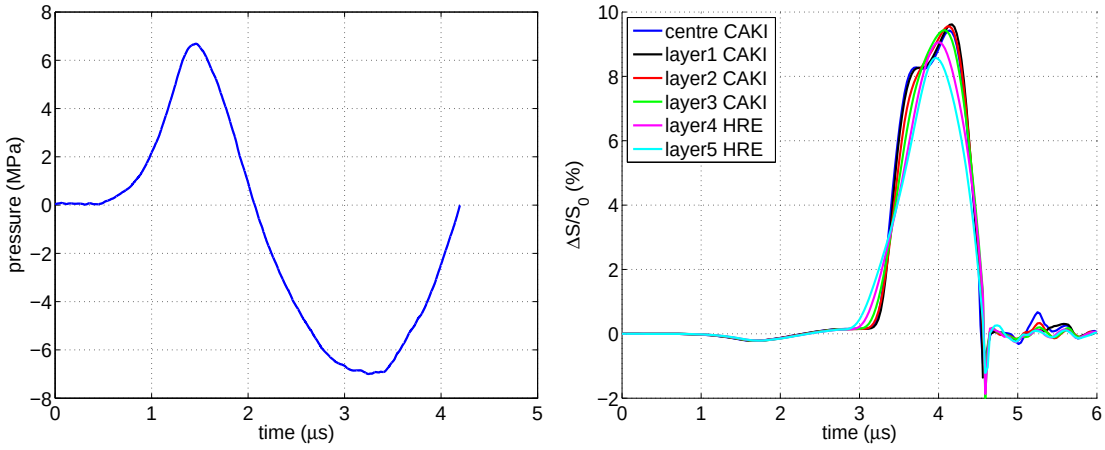

(a) (b)

Figure 7.23: (a) Applied artificial shock wave profile. (b) membrane strain measured at each representative cells in the spheroid model.

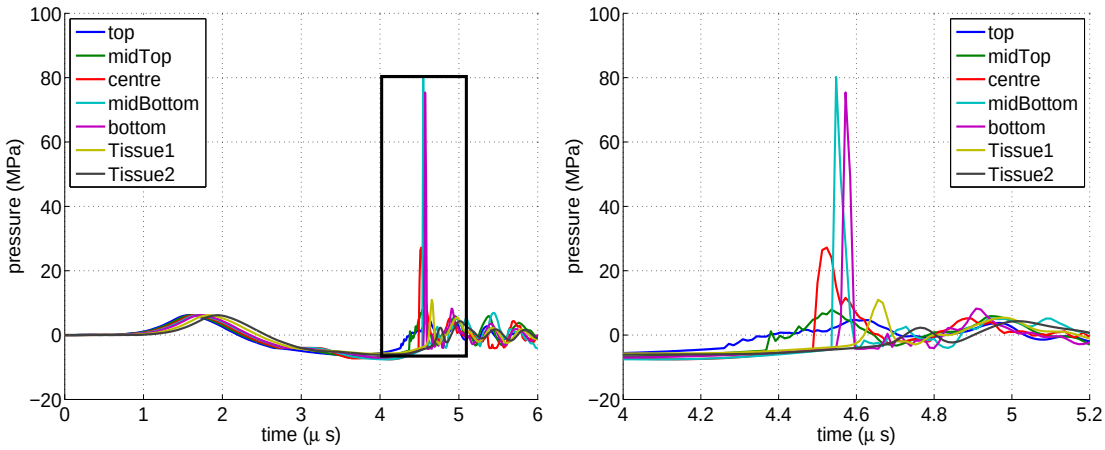

(a) (b)

Figure 7.24: (a) Pressure waveforms measured at the sampling points in Figure 7.25. (b) A zoom-in view on the occurrence of the pressure peaks.

7.2.2.4 Explanation of the observed secondary shock waves

Figure 7.24 (a) shows the build-up and dissipation of the shock wave pressure measured at the sampling points indicated in Figure 7.25. A zoomed view of the pressure waveforms are depicted in Figure 7.24 (b). The formation of the pressure spikes are discussed below.

As shown in Figure 7.26, there are two transitions of bulk modulus in cells during the tensile phase of the shock wave. During the second transition of the

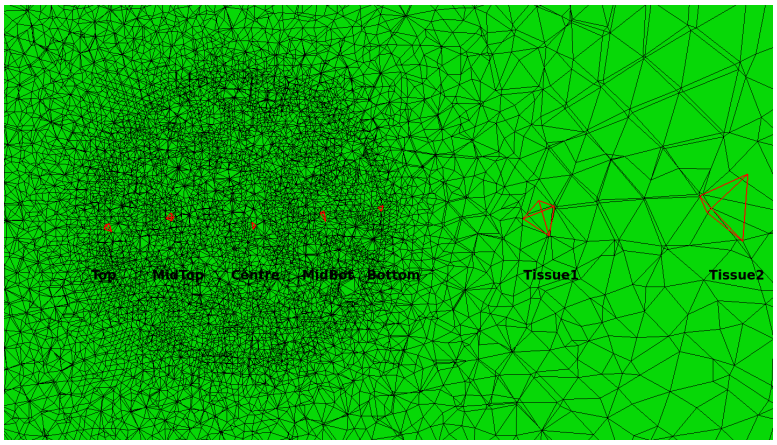

Figure 7.25: Sampling points in the model for pressure waveform measurements. The shock wave propagations from left to right.

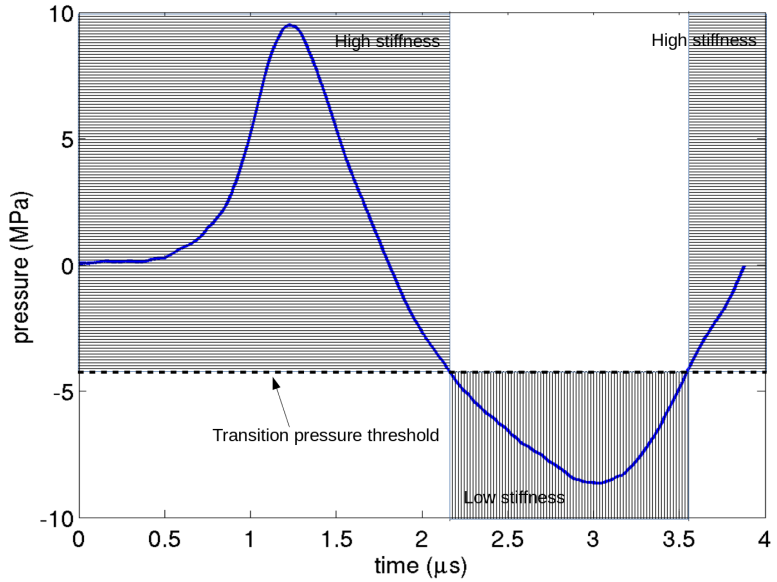

Figure 7.26: Bilinear bulk properties corresponding to the shock wave profile. The presented shock wave is at the shock wave energy level 8.

bulk modulus (from low stiffness K_T to high stiffness K_C), the sudden stiffening of bulk resistance caused an accelerated cell deformation which led to the generation of a secondary shock wave.

Figure 7.27 shows the distance of the central cell membrane relative to its centre (i.e., equivalent cell radius), the corresponding velocity of the membrane, and the acceleration of the membrane. It can be seen that the cell membrane contracts (1-3 µs) during the compressive phase of the shock wave, and expands

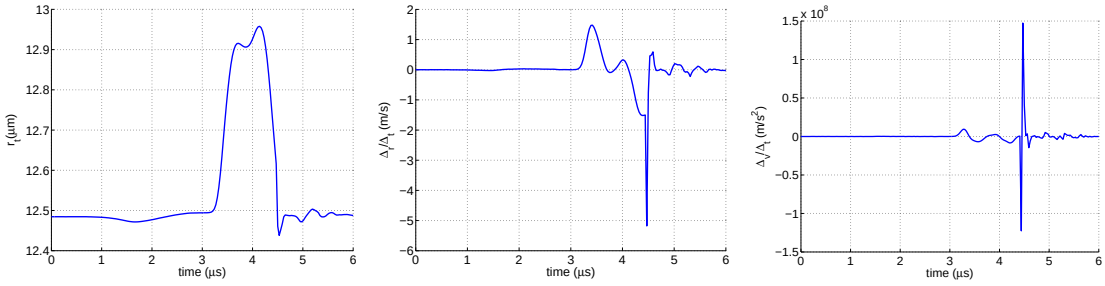

(a) (b) (c)

Figure 7.27: (a) The radius of the membrane of the innermost cell relative to the cell centre as function of time. (b) The velocity of the membrane relative to the centre, showing a sharp transition at 4.5 µs which corresponds to the transition from soft to stiff moduli. (c) The acceleration of the membrane.

during tension (3-5 µs). An abrupt change of velocity was found around 4.5 µs, see Figure 7.27 (b), which also resulted in a sudden increase in the acceleration of the cell membrane in Figure 7.27 (c). The farfield pressure is related to acceleration hence the peak in acceleration should result in the highest radiated pressure (secondary shock waves). The timing is consistent with the occurrence of the pressure spikes in Figure 7.24 as well as the transition from soft to stiff moduli.

Figure 7.24 also shows that the pressure peaks were further enhanced to ∼80 MPa in the distal part of the cluster. This phenomenon is similar to the generation of pressure pulses from bubble cloud cavitation (Wang and Brennen, 1995): the initiation of the pressure peaks induced by the cells in cluster surface further promotes the acceleration of neighbouring cell deformation, resulting in strengthened shock waves during propagation. The change of pressure fields over time corresponding to the waveforms are visualised in Figure 7.28. It can be seen that secondary shock wave pressure was generated at the surface of the cell cluster when the pressure passed the transition pressure threshold again before returning to zero (Figure 7.28(b)). As the pressure propagated, the secondary shock wave was strengthened by the acceleration induced in the neighbouring cells, forming a larger pressure pulse in the central and distal part of the cluster (Figures 7.28(c)-(e)). Such focussed pressure gradually diminished as the wave propagated (Figure 7.28(f)).

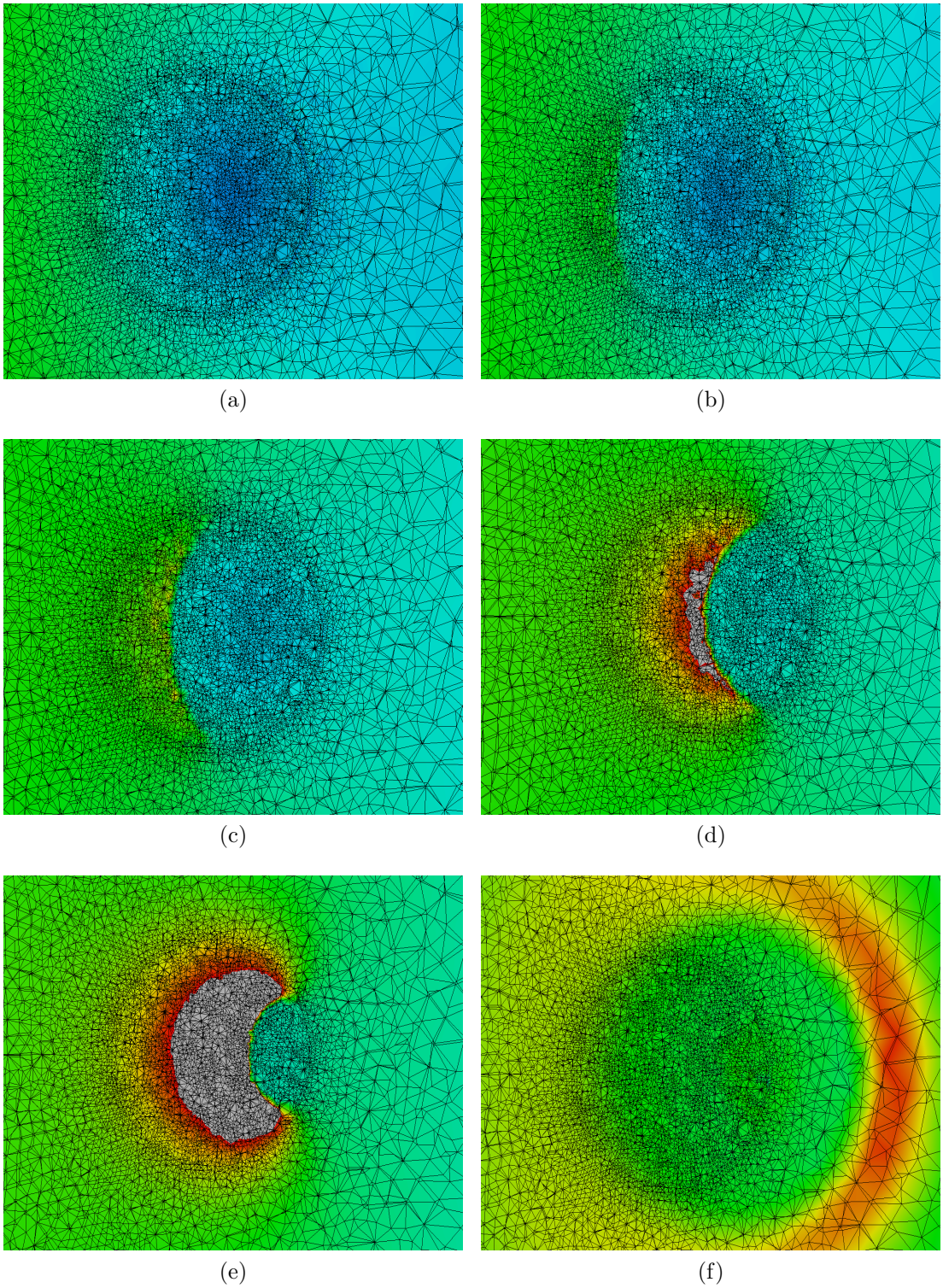

(a) (b) (c) (d) (e) (f)

Figure 7.28: Visualisation of the progression of pressure fields (within 400ns). (a) The shock wave arriving at the cluster. (b)-(e) The evolution of secondary shock wave across the cell cluster. (f) Dissipation of the pressure peaks.

7.3 Discussion and conclusion

This work aims to extend the study of single cell interaction with shock waves into a more biophysically realistic environment. It analyses factors on the single cell response which are important for *in vitro* studies, such as cell size, shape and orientation. The results showed that for a single cell embedded in the extracellular environment, the cell size, shape and orientation did not make a significant difference in pressure propagation and membrane strain. However the von Mises stress was influenced by cell shape and orientation. This may be related to the model curvature as a smaller curvature radius resulted in a higher von Mises stress. However, the maximum von Mises stress still remained in the order of 100 Pa. Hence, the simulation results showed that a spherical cell model can be used to model the single cell response in a 3D extracellular matrix as the influence of cell size, shape and orientation are not significant.

The presence of neighbouring cells was found to induce a strong effect on the cell response to shock waves. The surrounding layers resulted in a focussed pressure on the central cell of the cluster mainly due to the two bulk moduli during the tensile phase of the shock waves, leading to a sudden increase of acceleration of cell deformation at the transition which generated a secondary shock wave. Furthermore, both the von Mises stress and membrane strain were amplified by roughly four-fold with the presence of surrounding layers compared to without. The membrane strain response of the central cell converged with more than three surrounding layers. This indicates that cell response was only influenced locally by the neighbouring cells, even though the von Mises stress may be more sensitive to a wider range of neighbouring cells. Homogeneous distribution of the membrane strain was found within the cluster even though small changes in waveform shapes were identified in the representative cells at different layers due to the influence of stress interference between the cell cluster and the environment. A more heterogeneous distribution was found in the von Mises stress evolution showing a concentrated von Mises stress in the cluster centre of $\sim$600 Pa. The results showed that with more than three layers of surrounding cells, most of the relevant mechanical measures converged, indicating a localised effects of neighbouring cells. Therefore, the proposed model can be representative for cell cluster studies.

The response of multicellular spheroid made of CAKI-2 and HRE cells was

also analysed in order to study the differentiation between cancer cells and their noncancerous counterparts in a more biophysically realistic (e.g., tumour mimicking) environment. This study used the same artificial shock wave profiles as in the previous single cell study. The cell membrane strain was found to increase in both cancer and normal cells due to the effects of neighbouring cells. A significant difference in cell response to shock waves between the cancer and normal cells was discovered. This phenomenon indicates that in a 3D multicellular environment, cancer cells can also be targeted with minimal interference on the surrounding normal and healthy cells.

In conclusion, this work extends the single cell study to more realistic scenarios by modelling the cell interaction with shock waves under the influence of the intrinsic cell characteristics (i.e., size, shape and orientation) and neighbouring cells. The intrinsic cell characteristics were found not to strongly influence the cell response, whilst the presence of surrounding neighbouring cells was found to enhance the single cell response to shock waves, which suggests that environment is critical and single cell experiments may not be representative for more complex environments. This work also showed a preliminary indication of the effects of neighbouring cells, revealing that a cluster model with three surrounding layers should be sufficient to represent cells embedded in tissue. The study also confirmed that the shock wave profiles proposed in Chapter 6 also differentiated cancer cell and normal healthy cells in the multicellular spheroid environment.

CHAPTER 8

Cell model to account for damage contribution

An alternative Equation of State which accounts for "microtrauma" in the cells during large stretch is presented in this chapter. Numerical studies on single cell and cluster cells using the proposed EoS are discussed here.

8.1 Improved EoS with damage

In the EoS employed in Chapter 5, a bilinear model was used with the different bulk moduli of cells (K_C and K_T) to account for the difference in cell deformation during the compressional and tensile phases of the shock wave observed in the experiment. An elastic hysteresis behaviour is observed in materials such as rubber. The reduced stiffness is associated with energy loss to internal friction that breaks the internal structure. When the material is unloaded it does not typically return along the same path but along the one with less energy. We propose that a similar process occurs in tissue where microdamage occurs under tension during shock wave loading. Further the previous damage sustains and the EoS therefore evolves over time. The microdamage induced and accumulated in multiple consecutive shock waves may explain the noncavitational damage observed in experiments (Williams Jr et al., 1999; Evan et al., 2002; McAteer et al., 2007).

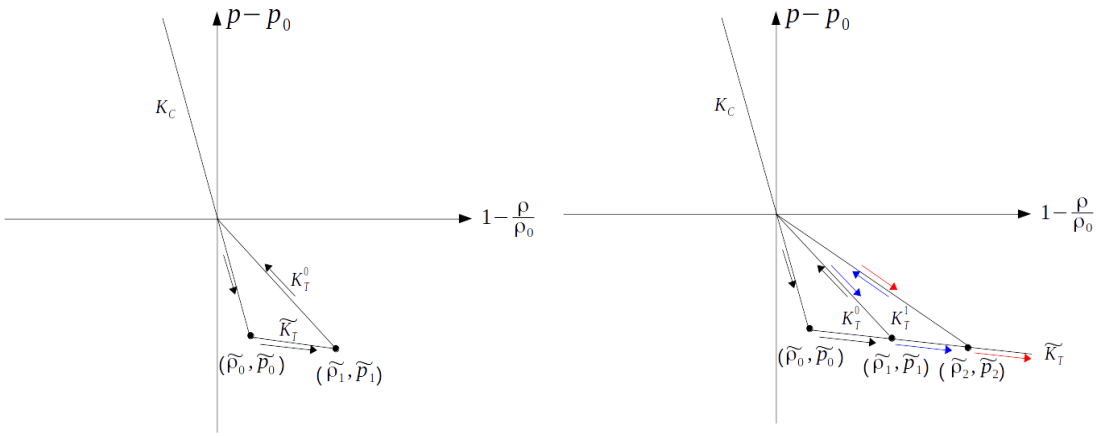

(a) (b)

Figure 8.1: Schematics of the improved EoS (a) reversible damage model; (b) progressive damage model based on irreversible cohesive zone model.

Research studies have found that the shock wave loading rate is strongly correlated to tissue damage during shock wave treatments (McAteer et al., 2007), indicating that the cell membrane may or may not recover depending on the loading rate. Therefore, a new EoS is considered to include a dynamically evolving damage mechanism depending on the recovery time and shock wave loading rate. Here two cases are developed: a reversible damage model and a progressive damage model. The reversible damage model assumes that the microtrauma is induced during each shock loading but the membrane lipids recover during the interval between the consecutive shock waves, see Figure 8.1(a). Hence, after microdamage is induced during the large stretch of the cell ($\widetilde{K_T}$), a different tensile bulk modulus (K_T^0) is presented during the unloading phase. The cell repeats its response to the subsequent shock waves as the cell is assumed to recover before the next shock wave arrives.

The progressive damage model, on the other hand, considers the case where subsequent shock waves arrive on a time scale much shorter than the cell recovery time. Thus damage from the contribution of each shock wave is progressively accumulated, inspired by the principles of the irreversible cohesive zone model (Ortiz and Pandolfi, 1999), see Figure 8.1(b). The irreversible cohesive zone model is often used for modelling progressive material deterioration in crack growth. This approach is adapted here by considering a progressively softer bulk stiffness under tension for each loading cycle.

In each shock loading, $i = 0, 1, 2, ..., N$, the cell transits to a softer state ($\widetilde{K_T}$) after the transition pressure threshold ($\tilde{p}_i$) either because of filaments deactivation and activation, or because of creation of cavities (see discussions in Section 4.4). The large stretch may introduce microdamage which results in a change of bulk stiffness during unloading (K_T^i). During the subsequent reloading phase, $i+1$, as the damage remains, the cell is initially stretched in the same path as the previous unloading process ($K_T^{i+1} = K_T^i$) until the tension further damages the cell. Assuming the damage mechanism remains the same, further stretch results in a bulk stiffness of $\widetilde{K_T}$ in the cell, followed by unloading and reloading cycles:

$$p = \begin{cases} \mathrm{H}(p)\left\{K_C \frac{\rho-\rho_0}{\rho_0}\right\} \\ +\mathrm{H}(-p)\left\{\mathrm{H}(p-\widetilde{p}_i)\left(K_T^i \frac{\rho-\rho_0}{\rho_0}\right)\right\} \\ +\mathrm{H}(-p)\left\{\mathrm{H}(\widetilde{p}_i-p)\left(\widetilde{K_T}\frac{\rho-\rho_0}{\rho_0}+\Delta p_i\right)\right\}, & \text{if } dP>0 \\ \\ \mathrm{H}(p)\left\{K_C \frac{\rho-\rho_0}{\rho_0}\right\} \\ +\mathrm{H}(-p)\left\{K_T^i \frac{\rho-\rho_0}{\rho_0}\right\}, & \text{otherwise} \end{cases}$$

where, $i = 0, 1, 2..., N$ refers to the shock waves cycles which are coloured differently in Figure 8.1(b), and $\tilde{p}_i$ is the transition pressure threshold in each loading. Note that the reversible damage is the first order of the progressive damage model. It is also important to note that this study only accounts for the change of bulk stiffness as a manifest of the presence of microdamage instead of including a plasticity model through plastic deformation.

$$\begin{aligned} \Delta p_i &= (K_T^i - \widetilde{K_T})\frac{\tilde{\rho}_i - \rho_0}{\rho_0} \\ K_T^i &= p_{max}^- \frac{\rho_0}{\rho_{min} - \rho_0} \\ K_T^{i+1} &= K_T^i \end{aligned} \tag{8.1}$$

where K_T^i is the tensile bulk modulus during unloading and K_T^{i+1} is the bulk modulus during reloading, p_{max}^- is the maximum tensile pressure in each shock wave loading and ρ_{min} is the corresponding density.

Furthermore, in the reloading phase, the transition from compressive bulk modulus K_C to tensile bulk modulus K_T^{i+1}, is at the zero-crossing, as opposed to in the first shock loading where the cell bulk stiffness remains the same as in the compressive phase until the transition pressure threshold is reached in the

early stage of tension. This may be explained by the presence of microdamage induced by the shock waves, which lowers the resistance from the filament network responsible for the initial higher stiffness to tension in the first shock loading.

8.2 Single cell studies

The reversible damage model, the progressive damage model and the bilinear bulk moduli model (see Chapter 5) are compared for the single cell FE model described in Chapter 5, which is submitted to three consecutive shock waves at energy level 6 here, see Figure 8.2. CAKI-2 cells were selected here and their

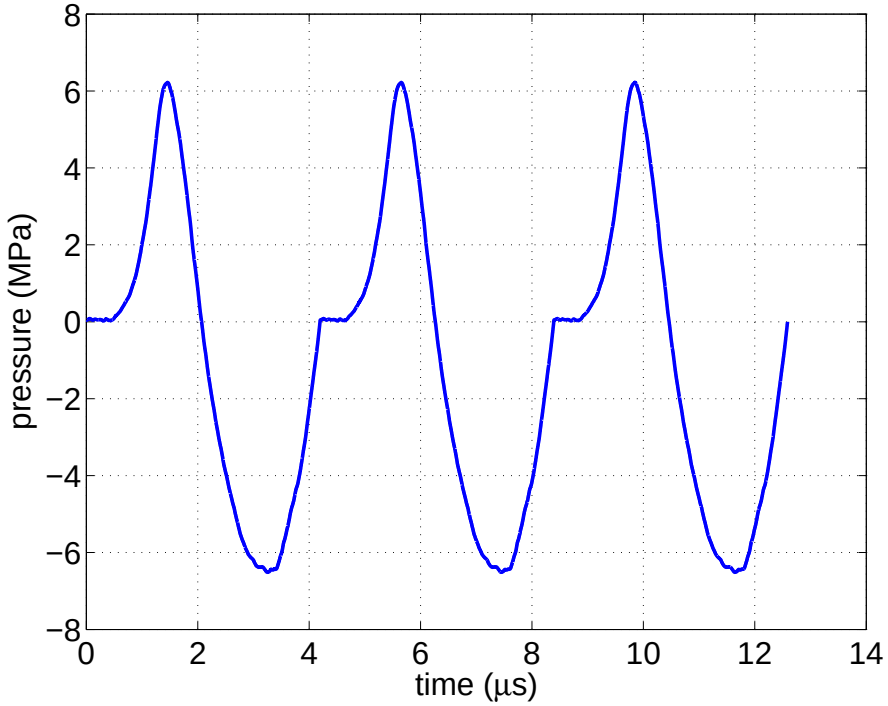

Figure 8.2: Three consecutive shock waves at shock wave energy level 6.

volumetric mechanical properties in the bilinear bulk model are listed in Table 8.1. These material parameter values are also applied to the reversible and progressive damage model. Other damage model parameter values (K_T^0 and $\tilde{p}_1$ for reversible damage model; K_T^i, $\tilde{p}_{i+1}$ and K_T^{i+1} for progressive damage model) were dynamically calculated based on the shock wave input. Their estimated values are listed in Table 8.1.

The overall membrane strain of the single cell and its pressure waveform mea-

Table 8.1: Material properties of the CAKI-2 cells in the three models. The parameters with estimated values are dynamically calculated in the models.

bilinear bulk model	compressive bulk modulus K_C	tensile bulk modulus K_T	transition pressure $\tilde{p}$			
	2 GPa	34 MPa	-4 MPa			
reversible damage model	compressive bulk modulus K_C	soft state bulk modulus $\widetilde{K_T}$	initial transition pressure $\tilde{p}_0$	unloading bulk modulus K_T^0	unloading pressure $\tilde{p}_1$	
	2 GPa	34 MPa	-4MPa	∼100 MPa	∼-7 MPa	
progressive damage model	compressive bulk modulus K_C	soft state bulk modulus $\widetilde{K_T}$	initial transition pressure $\tilde{p}_0$	unloading bulk modulus K_T^i	unloading pressure $\tilde{p}_{i+1}$	reloading bulk modulus K_T^{i+1}
	2 GPa	34 MPa	-4 MPa	∼100 MPa	∼-7 MPa	∼100 MPa

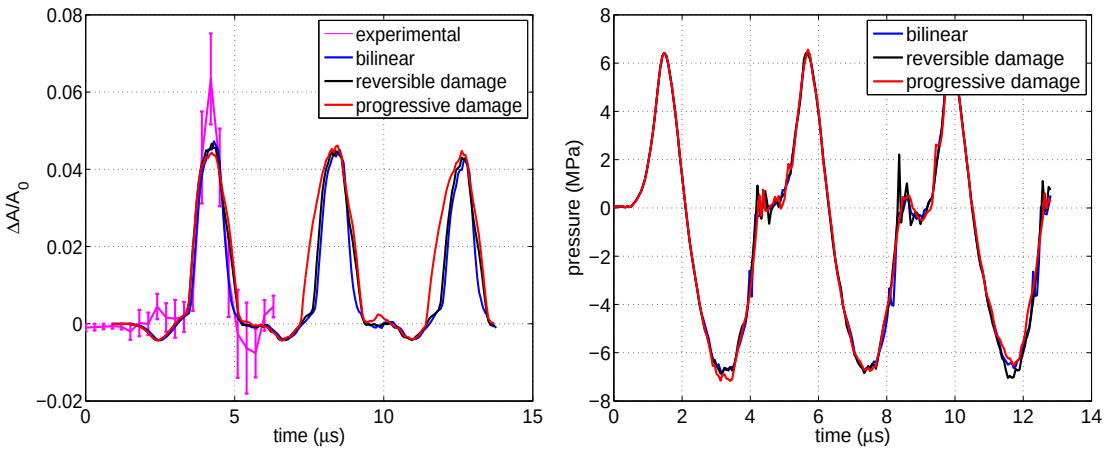

(a) (b)

Figure 8.3: Single cell response using bilinear bulk moduli model (blue), reversible damage model (black) and progressive damage model (red): (a) membrane strain, previous experimental data for one shock loading (magenta); (b) pressure waveform measured at the cell centre.

sured at the cell centre using the three models are presented in Figure 8.3. Under the first shock cycle, the simulation results of the two cell damage models retained a good agreement with the experimental observations in Chapter 4 (Figure 8.3 magenta) and the results showed no significant difference to the bilinear bulk

moduli model except in the unloading phase. During the unloading phase, the membrane strain from the damage models showed a different gradient from that of the bilinear bulk moduli model due to the irreversible bulk stiffness used in the unloading phase.

In the subsequent shock loading, the progressive damage model showed an increased gradient of the membrane strain during the tensile wave loading phase, which was caused by the progressive decrease of tensile bulk modulus during each shock wave loading. Furthermore, in the subsequent shock loading, the transition to large cell deformation occurred earlier in the progressive damage model (from the transition pressure threshold to zero-crossing), which led to a longer duration of the large stretch of the cell during the tensile wave. This in turn may result in further damage accumulation.

The pressure measurement for all cell models showed a similar waveform as the input profile. However, higher frequency oscillations were found in the interval between the consecutive shock waves, which may be caused by the change of bulk modulus at the zero-crossing from K_T^i to K_C. Overall, for a single shock loading, the damage models did not significantly alter the original results obtained from the bilinear bulk moduli model.

8.3 Cell cluster study

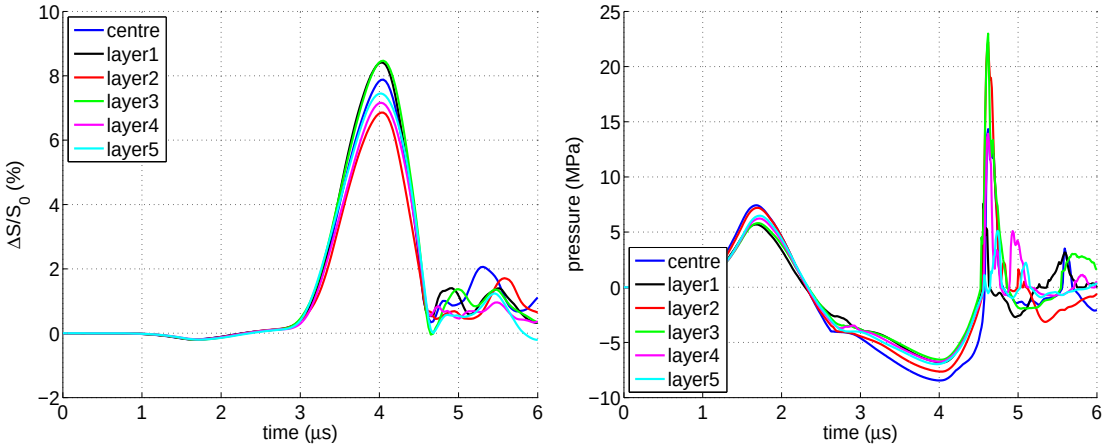

(a) (b)

Figure 8.4: (a) Cell membrane strain and (b) pressure profiles simulated at the representative cell in each surrounding ring layer.

The effect of the reversible damage model on the response of the cell cluster under a single shock cycle was compared to that using the bilinear bulk moduli model shown in Chapter 7. The progressive damage model is not presented here as its response is shown to be the same as the reversible damage model in single shock condition (Section 8.2).

For the full cell cluster (see Figure 7.21), the membrane strain and the pressure evaluation of each representative cell in the cluster are presented in Figure 8.4. The membrane strain was similar to that using the bilinear EoS, revealing a maximum value of 7-9%. A difference was found in the pressure waveforms between the progressive damage model and the bilinear bulk model: pressure spikes were found after zero-crossing (as opposed to the transition point) with a much smaller magnitude (~25 MPa as opposed to ~80 MPa). This may be caused by the change of bulk modulus (from K_T^i to K_C) shifting from the transition threshold to the zero-crossing. Since the pressure spikes appeared after the applied shock wave returned to its equilibrium, the transition of bulk stiffness at zero-crossing caused by the presence of positive pressure may be initiated by either the shock wave oscillation after reaching equilibrium or the pressure interference due to the mismatch of bulk moduli between the cluster and surrounding environment. Similarly to the bilinear bulk moduli model, as explained in Section 7.2.2.4, the positive pressure peaks were further enhanced by the neighbouring

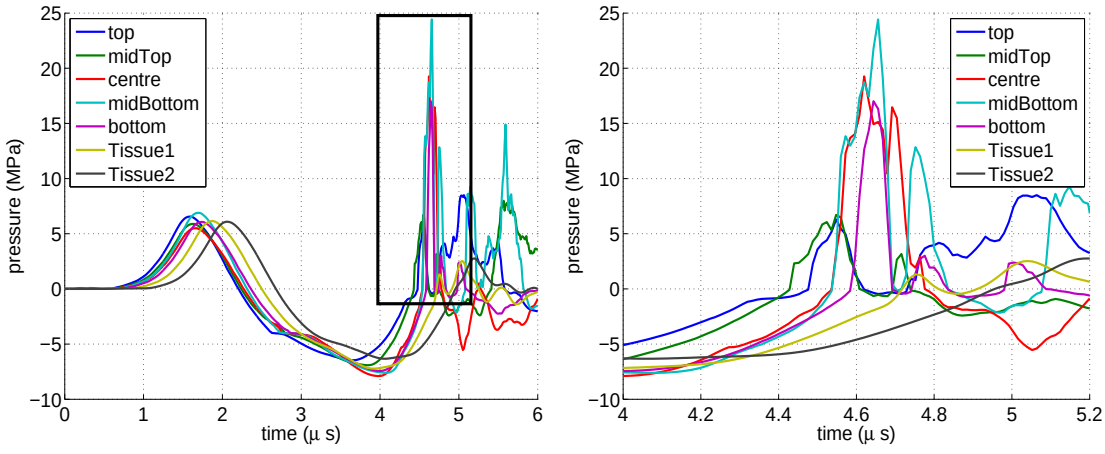

Figure 8.5: (a) Pressure waveforms measured along the central shock wave propagation path; (b) a zoomed view of the spikes observed in the pressure waveforms with the progressive damage model (labelled).

cells during propagation, resulting in strong secondary shock waves. The pressure waveforms measured at different sampling points along the central line of the shock wave propagation path (Figure 7.25) are shown in Figure 8.5.

The change of pressure field over time is also presented in Figure 8.6, showing that the positive pressure was formed after the original shock wave reached equilibrium and gradually concentrated in the centre of the cluster to generate the secondary shock waves, which was further enhanced during the propagation before dissipation.

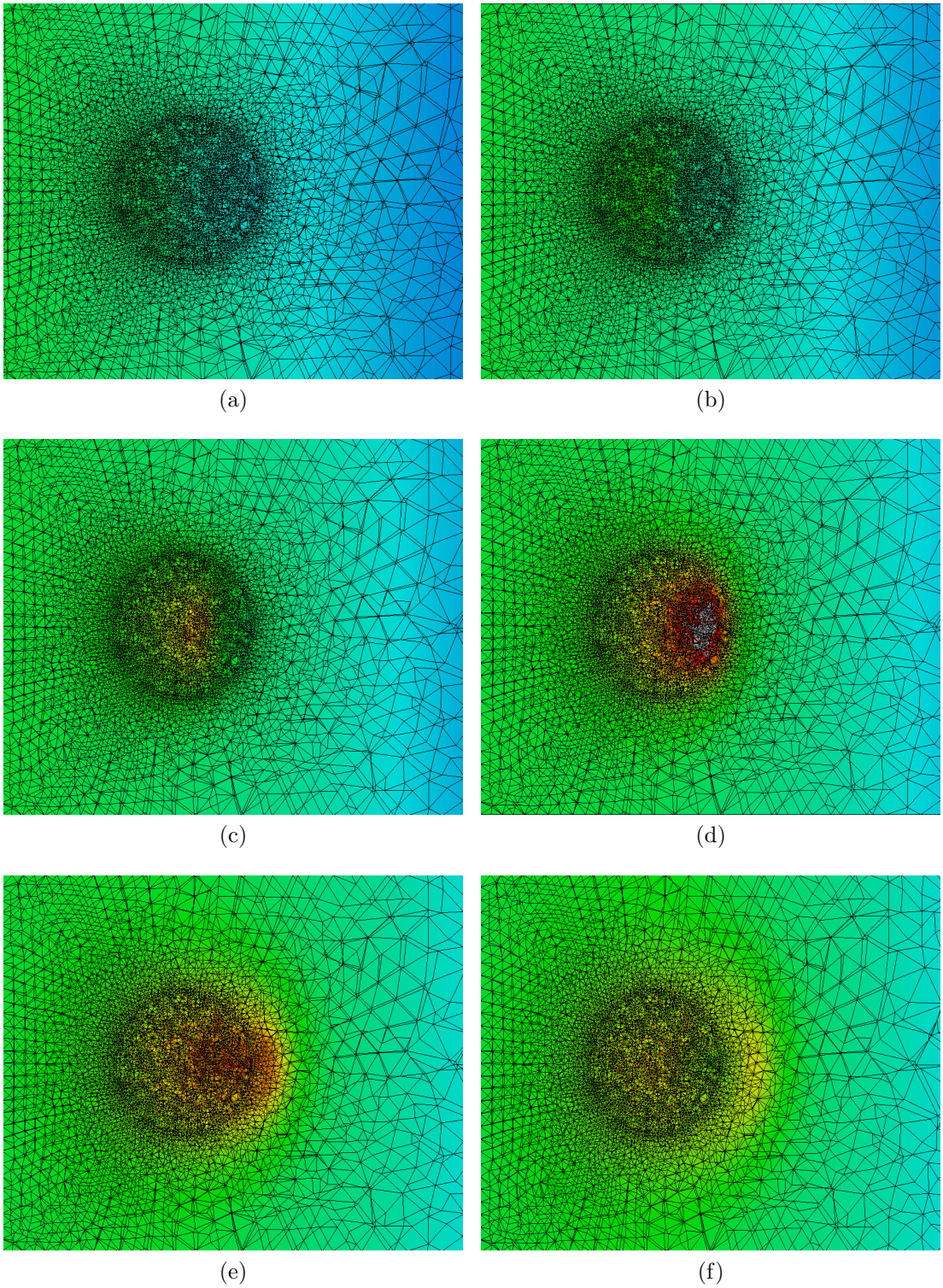

(a) (b) (c) (d) (e) (f)

Figure 8.6: Visualisation of the progression of pressure fields over time. (a) The shock wave arriving at the cluster. (b)-(d) The evolution of secondary shock wave across the cell cluster. (e)-(f) Dissipation of the pressure peaks.

8.4 Discussion and conclusion

Two cases of EoS were proposed to capture the potential microdamage mechanisms in the cell response to shock waves by including the change in bulk stiffness during the unloading and subsequent loading cycles. The reversible damage model assumes that the cell recovers to its original state while the progressive damage model assumes that the damage is not recovered but may be further accumulated in each shock loading. This is determined by the relation between the shock wave loading rate and the cell recovery time: if the shock loading is slower than the cell recovery time, the cell recovers to its original state before the subsequent shock wave arrives; however, if the loading is much faster than the cell recovery, there is no enough time for cells to recover, hence the microdamage will accumulate. In reality, it will be the combination of the two, i.e., the cell may be able to recover at the beginning and gradually lose its recovery ability under multiple shock waves.

The response of a single cell under multiple shock waves using the two damage models were compared to that using the bilinear bulk moduli model (i.e., assuming no damage). The results showed no significant difference in the first shock loading even though the two damage models showed a different gradient of the cell membrane strain during the unloading phase, which is due to the irreversible bulk modulus used in the damage model for the unloading cycle. Both the reversible damage and bilinear bulk moduli models showed the same cell response to the subsequent shock waves as to the first shock loading, while the progressive damage model showed an increased gradient in each loading phases due to the progressive change of the bulk modulus for the loading cycles, which also leads to an increased duration of the tensile area expansion in each subsequent shock loading, which may result in more damage on the cells compared to the reversible damage or nondamage models.

The progressive damage model was also applied to the cell cluster and was compared to the bilinear bulk moduli model under a single shock loading condition. The simulation results revealed an occurrence of secondary pressure spikes with much smaller magnitude at the zero-crossing, which may be initiated by either the pressure interference between the cluster and the surrounding matrix or the pressure oscillation after equilibrium, and enhanced and accumulated by the neighbouring cells in the cluster. However, the pressure spikes did not result

in significant change on the membrane strain of the cells.

In conclusion, this work provides further insight to the possible microdamage mechanisms of cell interaction with shock waves. Tissue damage effects were found to be rate dependant, for example, tissue damage at ∼2Hz shock wave exposure is greater than that using 0.5Hz. The proposed reversible damage model may explain the reversible sonoporation effects while the progressive damage model adapted from the irreversible cohesive zone model may explain the accumulated damage resulted from repetitive direct stress. However, it is also important to note that due to the absence of experimental data on the development of consecutive shock wave-induced cell or cluster damage (which may not be straightforward due to the difficulty in isolating cavitation effect and in visualising the progression of cell or cluster damage under a controlled amount of shock loading), we have not yet been able to validate this model. However, the models are speculated based on some experimental studies on cell membrane interaction with shock waves and some biophysical mechanisms at molecular levels.

CHAPTER 9

Conclusions

A numerical and experimental study has been conducted to investigate the response of a single cell subject to an incident shock wave. Experimentally, ultra-high speed imaging is employed to observe the single cell deformation in response to shock waves. The experimental measurement shows that cells present much lower bulk stiffness to tension than to compression. A finite element model was developed to numerically simulate the interaction between shock waves and a single cell embedded in the extracellular matrix, which allows for quantitative analysis of cell membrane strain, providing indications for cell membrane permeability which is important for shock wave mediated therapy. In order to model the shock wave interactions with cells more realistically, the influence of cell size, shape, orientation and neighbouring cells are also analysed. Furthermore, two new Equation of State are proposed to account for potential damage induced during shock loading.

9.1 Executive summary

Shock waves have been applied medically for decades, for indications such as kidney stones and musculoskeletal pain. Research studies have been identifying new avenues for shock wave mediated therapies such as histotripsy and drug or gene delivery for cancer treatment. However, one of the key issues for shock wave mediated treatments is the low therapeutic efficacy due to side-effects associated. For instance, tissue haemorrhage is often observed during kidney stone breakage. Experimental studies have focussed on improving the therapeutic efficacy of acoustic wave mediated drug delivery by testing different combinations of acoustic parameters and molecules. However, the research studies are limited by experi-

mental resources. Therefore, the aim of this work was to study the mechanisms of shock wave interactions with individual cells in order to understand the shock wave induced bioeffects such as cell damage and sonoporation effects. Different cell lines representing invasive cancer cells (CAKI-2 cells) and their noncancerous counterparts (HK-2 and HRE cells) were employed to measure their mechanical properties in response to shock waves in order to explore the possibility of cancer cell-specific shock wave treatment.

Ultra-high speed imaging was employed to observe single cell deformation in response to shock waves (as described in Chapter 3). In the experiment, individual cells were positioned in the intersecting focii of the shock wave pressure field and the high speed imaging field in order to visualise the cell deformation in response to a focussed shock wave. Three different shock wave energy levels were used in order to study the cell response to shock waves at different stress amplitudes and stress rates. The ultra-high speed camera respectively took 16 image frames with 3.3Mfps frame rate before and during shock wave exposure in order to exclude channel-to-channel difference while analysing cell deformation under shock waves.

The cell deformation was extracted from the images using a semi-automatic image processing algorithm, including a denoising filter (nonlocal means filter), initial contour guess, active contour segmentation, and a feature extraction algorithm. The nonlocal means filter reconstructed the noisy high speed images based on the intensity similarity of each pixels across the image, therefore the noise and artefacts in the image were filtered out without interfering with the main feature (i.e., cell contour) in the image. The contour estimation algorithm estimated the initial cell contour in terms of location and shape, which was further refined by the active segmentation algorithm to produce a more precise cell contour segmentation based on the intensity gradient of the region of interest. The cell response was analysed with respect to area and perimeter change during shock loading at each imaging time point. By analysing the area change and the relationship between area and perimeter change, the volumetric and deviatoric response were studied, indicating that the cell deformation under shock waves is mainly governed by its volumetric change. The study also included the analysis of imaging and segmentation variabilities due to the object movement, acoustic-optical effects and image quality.

The experimental results were presented in Chapter 4. At the highest shock wave energy level (level 8), cells were found to undergo small area decrease (less than 2%) in response to the compressive phase of the shock wave, followed by large cell expansion (order of 10%) under the tensile phase of the shock wave. However, this asymmetrical change of cell area was not consistent with the relationship between the compression and tensile phases of the shock wave. This indicates that cells behave differently under compression and tension. The duration of the cell expansion was between 1.5-1.8 µs which was slightly shorter than the duration of the shock wave tensile phase (2.1 µs), showing a hysteresis effect of the cell responding to tension. Furthermore, a factor of two was found between the area change and the perimeter change of the cells in all shock wave energy levels, this was consistent with the relationship between the area and perimeter change for a circle, revealing that the observed cell deformation was mainly volumetric without much shape change.

The main differences of the cell response among different cell lines were found in the amplitude and duration of the cell expansion in response to the tensile phase of the shock wave. At shock wave energy level 8, CAKI-2 cells showed a mean maximum area increase of 9% during tension and a tensile duration of 1.8 µs, while HK-2 and HRE cells presented a tensile duration of ∼1.5 µs with the mean maximum area increase of 17% and 13% respectively. The p-value less than 5% in the Mann-Whitney U test indicated that the maximum cell area increase was statistically different between CAKI-2 and HK-2 cells at shock wave energy level 8. The difference in cell response among the three cell lines reduced as the shock wave energy level decreased.

The experimental observations were captured with a numerical model simulating a single cell embedded in the surrounding extracellular matrix while subject to shock waves measured in the experiment, see Chapter 5. The volumetric response of the cell was modelled with a bilinear acoustic EoS to account for different cell stiffness in response to compression and tension with a pressure threshold to determine the transition between them. For compression and mild tension, the cell exhibited a high stiffness, but once the tensile stress exceeded the transition pressure threshold, the stiffness was reduced. The deviatoric response of the model was described by a first order generalised viscoelasticity framework with the material coefficients obtained from the literature and was not dependant on the state

of tension.

Calibration and cross-validation of the numerical model, as shown in Chapter 6, were used to determine material parameters for the models. For compression, the bulk modulus was set to 2 GPa. For tension, the parameters varied by cell type. For CAKI-2 cells, the transition pressure threshold was found to be -4 MPa and the tensile bulk modulus was 34 MPa; for HK-2 cells, the transition threshold was -4.6 MPa and the tensile bulk modulus was 20 MPa; and for HRE cells, the transition threshold was also -4.6 MPa and the tensile bulk modulus was 25 MPa. The results indicate that with the same amount of tensile pressure applied, cancer cells should be the first to undergo large deformation. It was also found that the cell deformation was not strongly affected by the change of deviatoric material coefficients, confirming the insignificant contribution of deviatoric response in the problem of interest.

The calibrated and validated mechanical properties of different cell lines allowed for quantitative evaluation of stress and strain evolution of the cells in response to shock waves. It was found that the pressure propagation wasn't strongly influenced by the difference in the mechanical properties between different cell types. The von Mises stress which estimates the amount of shearing in the model, was found to be in the order of 100 Pa due to small contribution of the deviatoric effects. The maximum membrane strain was found to be 8.5% in CAKI-2, 12% in HK-2 and 10% in HRE cells at shock wave energy level 8.

The model was used to "design" shock wave profiles that exploit the difference in the mechanical response between cancer cells and normal cells, by mainly exploiting the transition pressure threshold margin between them. One shock wave profile resulted in a maximum membrane strain of 1.1% in cancer cells (CAKI-2 cells) while that of the noncancerous cells (HK-2 and HRE cells) was less than 0.2%. This difference may lead to cancer cell specific sonoporation for drug delivery purpose. Furthermore, it has been reported that the rupture strain of cancer cells is 3-5% while that of normal cells is around 40%. Hence, a second shock wave profile was designed to result in more than 5% membrane strain in CAKI-2 cells to rupture them. In this case, the membrane strain of HK-2 and HRE cells were also found to be 5-6%, which, however, are well below their rupture strain. Therefore, a cancer cell specific rupture may be achieved with this shock wave profile.

In Chapter 7, the influence of cell size, shape, orientation and neighbouring cells were studied. The cell size, shape and orientation did not show significant change in pressure propagation and membrane strain (less than 15% variation). The von Mises stress was found to be largely influenced by the cell shape and orientation, which was due to the model curvature concentrating the stress. However, the von Mises stress was still found to be in the order of 100 Pa, which was much smaller in magnitude compared to the volumetric stress (pressure). When modelling a cluster of cells rather than an isolated cell, it was found that the presence of neighbouring cells had a significant effect on cell response. At the centre of the cluster, a focussed pressure wave (secondary shock) was observed with high amplitude (>10 MPa) and short duration (several hundreds nanoseconds), which was caused by the sudden stiffening of the cell bulk modulus at the transition. Furthermore, the von Mises stress and membrane strain of the central cell were largely increased with the presence of surrounding layers by roughly 4 folds, resulting in a maximum von Mises stress and membrane strain of ∼600 Pa and 8%, respectively at shock wave energy level 6. By analysing the cell response of the representative cell in each surrounding layers, the distribution of stress and strain evolution in the cluster was studied. A homogeneous distribution of cell response was found in the cluster, except for a higher von Mises stress concentrated in the cluster centre due to accumulative interference of stress waves.

In Chapter 7, the two designed shock wave profiles proposed in Chapter 6, which differentiate cancer and normal cells in the single cell case, were also studied to account for the influence of neighbouring cells. In general, the membrane strain in response to both shock waves increased in the cluster environment compared to individually in the agarose tissue phantom. In the first shock wave loading where the maximum tensile wave was -4.59 MPa (between the two transition thresholds of CAKI-2 and HRE cells), the membrane strain of CAKI-2 cells reached 1.3% while the surrounding HRE cells only exhibited a surface strain of ∼0.4%, indicating a potential cancer cell specific sonoporation effect. On the other hand, the second shock wave loading where cancer cell rupture was expected (∼10% membrane expansion for CAKI-2 cells) resulted in ∼10% membrane strain in HRE cells which is still below its rupture threshold. Therefore, similarly to the single cell case, a cancer cell specific rupture may be expected using this shock wave loading in a cell cluster.

Two new EoS were proposed in Chapter 8 to account for potential damage mechanisms in each shock loading. The reversible damage model assumed the damage induced in each shock loading would recover before the subsequent shock loading arrives, whilst the progressive damage model assumed an accumulative effect of damage from each shock loading. The simulation results showed that under a single shock wave exposure, little difference was found between the two models. However, with more shock loading, the duration of cell area expansion became longer for the progressive damage model while that for the reversible damage model remained the same. This has consequences on firing rate of shock waves.

9.2 Suggestions for future work

9.2.1 Validation of the proposed shock wave profiles

Currently the designed shock wave profiles showed cancer cell-specific effects *in silico*, which still needs to be experimentally validated. By carefully tuning the location of measurement in relation to the shock wave source (i.e., changing the position of the target cells in the pressure field) or adjusting the shock wave sources (e.g., discharge circuit may also affect waveforms), the desired shock wave amplitude may be acquired. The response of the three cell types should be measured through an ultra-high speed camera and compared to the simulation prediction. Furthermore, the predicted bioeffect such as sonoporation effect or cell damage may also be analysed.

9.2.2 Improved imaging technique

One of the key challenges in the current experimental work for visualising single cell deformation in response to shock waves is the imaging and segmentation variability due to object movement, acoustic-optical effects, image quality, etc. Therefore, more accurate evaluation of cell response to shock waves may be quantified with improved imaging techniques. For example, instead of using the bright field ultra-high speed imaging, fluorescent high speed imaging of cell contours or tracking microbeads attached to cell membrane may improve the imaging accuracy. Furthermore, a 3D view of the cell deformation (2D high speed imaging

of cell projections on two planes respectively) may reveal more volumetric and deviatoric cell deformation under shock waves.

9.2.3 Quantification of cell permeability and damage

Currently, the sonoporation effects and cell membrane damage were estimated from the overall membrane strain which may be a good indicator of the occurrence of such bioeffects. However, a quantitative analysis linking the membrane strain to the cell permeability and viability may provide more precise evaluation of shock wave induced bioeffects, thus helping to develop a better shock wave mediated treatment. The cell membrane permeability may be quantified by measuring the proportion of fluorescent molecules (e.g., fluorescein isothiocyanate-dextran with various molecular weights) diffusing into cells, while cell viability can be measured with propidium iodide solution which selectively label the dead cells.

9.2.4 Refinement of the damage model

Two EoS were developed to account for potential microdamage mechanisms associated with cell recovery and shock loading rate. One EoS assumes full cell recovery before the subsequent shock wave arrives while the other one assumes accumulated microdamage during each shock wave exposure. However, in reality, it will be a combination of the two conditions. Hence, a more general EoS may be proposed to dynamically change the damage mechanisms according to the shock loading rate. This has a significant clinical application as it is still not clear for clinicians to decide the optimal shock loading rate and numbers.

9.3 Conclusions

This work is the first attempt to visualise single cell deformation subject to incident shock waves to study the underlying mechanisms for shock wave interactions with cells. It was found that cells were stiffer under the compressive phase of the shock wave than under the tensile phase. The experimental observations were successfully captured by the proposed numerical model with a modified EoS using different bulk moduli for compression and tension, which provides valuable references for research studies on acoustics interactions with biological samples.

Shock wave profiles were designed to differentiate the cell response between cancer and noncancerous cells, by exploiting the difference in their mechanical properties. The designed shock wave profiles allow for selectively targeting cancer cells while minimising the influence healthy cells. Considering the variability of individual cells and possible morphological and physical changes in different biological scenarios such as in different organs, the designed shock waves may not show the differentiation between cancer cells and normal cells *in vivo* as distinctive as predicted. However, the proposed numerical model may still be useful in linking to a larger scale study of shock wave interactions with organs or help optimise cancer cell-specific bioeffects.

The numerical study of cell response to shock waves was extended to take into account of cell size, shape and orientation, and a more tissue-like cell morphology. The results indicate that single cell experiments may not be representative in complex environment.

Furthermore, two new EoS demonstrated the cell response in the assumption of a reversible or a progressive damage paradigm, which may explain the reversible sonoporation effect as well as the irreversible cell damage using multiple shock waves.

In conclusion, the proposed models provide a mechanistic understanding of cell response to incident shock waves, which may help improve the use of current shock wave treatments such as lithotripsy, or open new avenues for shock wave mediated treatments such as cancer therapy.

References

Amira for life sciences, FEI, 2014.

Abaqus. Abaqus user manual 6.12. Technical report, Simulia, 2012.

Akhshi, T. K., Wernike, D., and Piekny, A. Microtubules and actin crosstalk in cell migration and division. *Cytoskeleton*, 71(1):1–23, 2014.

Allen, T. and Cowling, G. *The cell: A very short introduction*, volume 2. Oxford University Press, 2011.

Amador, C., Urban, M. W., Warner, L. V., and Greenleaf, J. In vitro renal cortex elasticity and viscosity measurements with shear-wave dispersion ultrasound vibrometry (sduv) on swine kidney. In *Engineering in Medicine and Biology Society, 2009. EMBC 2009. Annual International Conference of the IEEE*, 2009.

Bao, S., Thrall, B. D., Gies, R. A., and Miller, D. L. In vivo transfection of melanoma cells by lithotripter shock waves. *Cancer research*, 1998.

Bensamoun, S. F., Robert, L., Leclerc, G. E., Debernard, L., and Charleux, F. Stiffness imaging of the kidney and adjacent abdominal tissues measured simultaneously using magnetic resonance elastography. *Clinical imaging*, 35(4):284–287, 2011.

Betney, M. R., Roy, R. A., and Ventikos, Y. *Computational and experimental study of intense shock-cavity interactions*. PhD thesis, University of Oxford, 2015.

Brujan, E. *Cavitation in Non-Newtonian Fluids: With Biomedical and Bioengineering Applications*, volume 7. Springer, 2010.

Brümmer, F., Bräuner, T., and Hülser, D. F. Biological effects of shock waves. *World Journal of Urology*, 8(4):224–232, 1990.

Buades, A., Coll, B., and Morel, J. M. A review of image denoising algorithms, with a new one. *Simul*, 4:490–530, 2005.

Carstensen, E. L., Gracewski, S., and Dalecki, D. The search for cavitation in vivo. *Ultrasound in Medicine & Biology*, 26(9):1377 – 1385, 2000.

Chen, H., Kreider, W., Brayman, A. A., Bailey, M. R., and Matula, T. J. Blood vessel deformations on microsecond time scales by ultrasonic cavitation. *Phys Rev Lett.*, 2011.

Child, S., Hartman, C., Schery, L., and Carstensen, E. *lung damage from exposure to pulsed ultrasound. Ultrasound Med Biol, 1990.*

Church, C. C. *A theoretical study of cavitation generated by an extracorporeal shock wave lithotripter. The Journal of the Acoustical Society of America, 1989.*

Cleveland, R. O. and McAteer, J. A. *The Physics of Shock Wave Lithotripsy. Smith's Textbook of Endourology, 2012.*

Coleman, A. J., Choi, M. J., Saunders, J. E., and Leighton, T. G. *Acoustic emission and sonoluminescence due to cavitation at the beam focus of an electrohydraulic shock wave lithotripter. Ultrasound in Medicine and Biology, 1992.*

Cruzado, A., Gan, B., Jimenez, M., Barba, D., Ostolaza, K., Linaza, A., Molina-Aldareguia, J., Llorca, J., and Segurado, J. *Multiscale modeling of the mechanical behavior of in718 superalloy based on micropillar compression and computational homogenization. Acta Materialia, 2015.*

Dao, M., Lim, C., and Suresh, S. *Mechanics of the human red blood cell deformed by optical tweezers. Journal of the Mechanics and Physics of Solids, 2003.*

Ebert, A. M., Du, J., Wang, X., and Tittmann, B. *The elastic properties of hamster kidney cells evaluated by ultrasonic atomic force microscopy, 2004.*

Egorov, V., Tsyuryupa, S., Kanilo, S., Kogit, M., and Sarvazyan, A. *Soft tissue elastometer. Med Eng Phys, 30(2):206–12, 2008.*

Evan, A. P., Willis, L. R., McAteer, J. A., Bailey, M. R., Connors, B. A., Shao, Y., Lingeman, J. E., Williams Jr, J. C., Fineberg, N. S., and Crum, L. A. *Kidney damage and renal functional changes are minimized by waveform control that suppresses cavitation in shock wave lithotripsy. The Journal of urology, 2002.*

Evans, E. and Yeung, A. *Apparent viscosity and cortical tension of blood granulocytes determined by micropipet aspiration. Biophysical journal, 1989.*

Fan, Z., Liu, H., Mayer, M., and Deng, C. X. *Spatiotemporally controlled single cell sonoporation. Proceedings of the National Academy of Sciences, 2012.*

Freund, J. B., Colonius, T., and Evan, A. P. *A cumulative shear mechanism for tissue damage initiation in shock-wave lithotripsy. Ultrasound in medicine & biology, 2007.*

Gamarra, F., Spelsberg, F., Dellian, M., and Goetz, A. E. *Complete local tumor remission after therapy with extra-corporeally applied high-energy shock waves (hesw). International journal of cancer. Journal international du cancer, 1993.*

Gladstone, J. H. and Dale, T. P. *Researches on the refraction, dispersion, and sensitiveness of liquids. Philosophical Transactions of the Royal Society of London, 1863.*

Gregory, T. R. *The evolution of the genome, volume 1. London : Elsevier Academic, 2005.*

Guilak, F., Tedrow, J. R., and Burgkart, R. *Viscoelastic properties of the cell nucleus. Biochemical and Biophysical Research Communications, 2000.*

Holzapfel, G. *Nonlinear solid mechanics. John Wiley& Sons, 2000.*

Houchmandzadeh, B., Marko, J. F., Chatenay, D., and Libchaber, A. *Elasticity and structure of eukaryote chromosomes studied by micromanipulation and micropipette aspiration. The Journal of Cell Biology, 139(1):1–12, 1997.*

Jérusalem, A. and Dao, M. *Continuum modeling of a neuronal cell under blast loading. Acta biomaterialia, 8(9):3360–3371, 2012.*

Jessica E Parsons, Charles a Cain, J. B. F. *Cost-effective assembly of a basic fiber-optic hydrophone for measurement of high-amplitude therapeutic ultrasound fields. The Journal of the Acoustical Society of America, 2006.*

Ji, B. and Bao, G. *Cell and molecular biomechanics: perspectives and challenges. Acta Mechanica Solida Sinica, 2011.*

Jonas, O., Mierke, C. T., and Kas, J. A. *Invasive cancer cell lines exhibit biomechanical properties that are distinct from their noninvasive counterparts. Soft Matter, 7(24):11488, 2011.*

Kamm, R., McVittie, A., and Bathe, M. *On the role of continuum models in mechanobiology. ASME-AMD, 2000.*

Karcher, H., Lammerding, J., Huang, H., Lee, R. T., Kamm, R. D., and Kaazempur-Mofrad, M. R. *A three-dimensional viscoelastic model for cell deformation with experimental verification. Biophysical journal, 2003.*

Karshafian, R., Bevan, P. D., Williams, R., Samac, S., and Burns, P. N. *Sonoporation by ultrasound-activated microbubble contrast agents: Effect of acoustic exposure parameters on cell membrane permeability and cell viability. Ultrasound in Medicine and Biology, 35 (5):847–860, 2009.*

Kass, M., Witkin, A., and Terzopoulos, D. *Snakes - Active Contour Models. International Journal Of Computer Vision, 4:321–331, 1987.*

Khokhlova, V., Fowlkes, J., Roberts, W., Schade, G., Xu, Z., Khokhlova, T., Hall, T., Maxwell, A., Wang, Y., and Cain, C. *Histotripsy methods in mechanical disintegration of tissue: towards clinical applications. Int J Hyperthermia, 2015.*

Kodama, T., Doukas, A. G., and Hamblin, M. R. *Shock wave-mediated molecular delivery into cells. Biochimica et Biophysica Acta - Molecular Cell Research, 2002.*

Krasovitski, B., Frenkel, V., Shoham, S., and Kimmel, E. *Intramembrane cavitation as a unifying mechanism for ultrasound-induced bioeffects. Proceedings of the National Academy of Sciences, 108, 2011.*

Kunz-Schughart, L., Kreutz, M., and Knuechel, R. *Multicellular spheroids: a three-dimensional in vitro culture system to study tumour biology. International Journal of Experimental Pathology, 2002.*

Larina, I. V., Evers, B. M., and Esenaliev, R. O. *Optimal drug and gene delivery in cancer cells by ultrasound-induced cavitation. Anticancer research, 2005.*

Leclerc, G. E., Debernard, L., Foucart, F., Robert, L., Pelletier, K. M., Charleux, F., Ehman, R., Ho Ba Tho, M.-C., and Bensamoun, S. F. *Characterization of a hyper-viscoelastic phantom mimicking biological soft tissue using an abdominal pneumatic driver with magnetic resonance elastography (mre). Journal of Biomechanics, 2012.*

Lewis, R. N. and McElhaney, R. N. *Membrane lipid phase transitions and phase organization studied by fourier transform infrared spectroscopy. Biochimica et Biophysica Acta (BBA)-Biomembranes, 10, 2012.*

Li, F., Chan, C. U., and Ohl, C. D. yield strength of human erythrocyte membranes to impulsive stretching. *Biophysical Journal*, 2013.

Lim, C., Zhou, E., and Quek, S. Mechanical models for living cells-a review. *Journal of Biomechanics*, 39(2):195–216, 2006.

Lin, K. W., Duryea, A., Kim, Y., Hall, T., Xu, Z., and Cain, C. Dual-beam histotripsy: A low-frequency pump enabling a high-frequency probe for precise lesion formation. *IEEE Transactions on Ultrasonics, Ferroelectrics, and Frequency Control*, 2014.

Lingeman, J., Woods, J., Toth, P. D., Evan, A., and McAteer, J. The role of lithotripsy and its side effects. *The Journal of urology*, 141 (3 Pt 2):793, 1989.

MA, A. and MF., H. Nonlinear distortion of short pulses radiated by plane and focused circular pistons. *The Journal of the Acoustical Society of America*, 102, 1997.

MathWorks. *Detect and Measure Circular Objects in an Image.*

Matlaga, B. R., McAteer, J. A., Connors, B. A., Handa, R. K., Evan, A. P., Williams, J. C., Lingeman, J. E., and Willis, L. R. Potential for cavitation-mediated tissue damage in shockwave lithotripsy. *Journal of Endourology*, 2008.

Maxwell, A. D., Wang, T.-y., Yuan, L., Duryea, A. P., Xu, Z., and Cain, C. A. A tissue phantom for measurement of us induced cavitation damage. *Ultrasound Med Biol.*, 2010.

McAteer, J., Evan, A. P., Willis, L. R., Connors, B., Williams, J. C., Pishchalnikov, Y., and Lingeman, J. E. Shock wave injury to the kidney in swl: Review and perspective. *AIP Conference Proceedings*, pages 287–301, 2007.

McAteer, J. A. and Evan, A. P. The acute and long-term adverse effects of shock wave lithotripsy. In *Seminars in nephrology*, 2008.

McGarry, J. and Prendergast, P. A three-dimensional finite element model of an adherent eukaryotic cell. *Eur Cell Mater*, 2004.

Mehier-Humbert, S., Bettinger, T., Yan, F., and Guy, R. H. Plasma membrane poration induced by ultrasound exposure: implication for drug delivery. *Journal of controlled release*, 104(1):213–222, 2005.

Miller, P., Hu, L., and Wang, J. Finite element simulation of cell-substrate decohesion by laser-induced stress waves. *Journal of the mechanical behavior of biomedical materials*, 3(3): 268–277, 2010.

Mishra, P., Hill, M., and Glynne-Jones, P. Deformation of red blood cells using acoustic radiation forces. *Biomicrofluidics*, 2014.

Mott, P., Dorgan, J., and Roland, C. The bulk modulus and poisson's ratio of incompressible materials. *Journal of Sound and Vibration*, 2008.

Murata, R., Nakagawa, K., Ohtori, S., Ochiai, N., Arai, M., Saisu, T., Sasho, T., Takahashi, K., and Moriya, H. The effects of radial shock waves on gene transfer in rabbit chondrocytes in vitro. *Osteoarthritis and Cartilage*, 2007.

Nasseri, S., Bilston, L. E., and Phan-Thien, N. Viscoelastic properties of pig kidney in shear, experimental results and modelling. *Rheologica acta*, 2002.

Ortiz, M. and Pandolfi, A. Finite-deformation irreversible cohesive elements for three-dimensional crack-propagation analysis. *Int. J. Numer. Meth. Engng.*, 1999.

Qiuquan, G., Ying, X., Martin, S., and Jun, Y. Characterization of cell elasticity correlated with cell morphology by atomic force microscope. *Journal of Biomechanics*, 45(2):304–9, 2012.

R. Quey, P.R. Dawson, F. B. Large-scale 3d random polycrystals for the finite element method: Generation, meshing and remeshing. *Comput. Methods Appl. Mech. Engrg.*, 2011.

Rebelo, L. M., De Sousa, J. S., Mendes Filho, J., and Radmacher, M. Comparison of the viscoelastic properties of cells from different kidney cancer phenotypes measured with atomic force microscopy. *Nanotechnology*, 24(5), 2013.

Rompe, J. D., Furia, J. P., and Maffulli, N. Mid-portion achilles tendinopathy current options for treatment. *Disability and Rehabilitation ISSN:*, 2009.

Ryan, M. J., Johnson, G., Kirk, J., Fuerstenberg, S. M., Zager, R. A., and Torok-Storb, B. Hk-2: an immortalized proximal tubule epithelial cell line from normal adult human kidney. *Kidney Int.*, 1994.

S. Nicolle, P. Vezin, J. F. P. A strain-hardening bi-power law for the nonlinear behaviour of biological soft tissues. *Journal of Biomechanics*, 2010.

Sato, M., Theret, D., Wheeler, L., Ohshima, N., and Nerem, R. Application of the micropipette technique to the measurement of cultured porcine aortic endothelial cell viscoelastic properties. *Journal of Biomechanical Engineering*, 112, 1990.

Schmid-Schonbein, G., Sung, K., Tozeren, H., Skalak, R., and Chien, S. Passive mechanical properties of human leukocytes. *Biophysical Journal*, 36, 1981.

Shigematsu, T., Koshiyama, K., and Wada, S. *effects of stretching speed on mechanical rupture of phospholipid / cholesterol bilayers : Molecular dynamics simulation. Nature Publishing Group, 2015.*

Simo, J. and Hughes, T. *Computational inelasticity. Springer, 2008.*

Snedeker, J. G., Niederer, P., Schmidlin, F. R., Farshad, M., Demetropoulos, C. K., Lee, J. B., and Yang, K. H. *Strain-rate dependent material properties of the porcine and human kidney capsule. Journal of Biomechanics, 2005.*

Sonden, A., Svensson, B., Roman, N., Ostmark, H., Brismar, B., Palmblad, J., and Kjellstrom, B. T. *Laser-induced shock wave endothelial cell injury. Lasers in surgery and medicine, 26(4):364–375, 2000.*

Steinhauser, M. O. and Schmidt, M. *Destruction of cancer cells by laser-induced shock waves: recent developments in experimental treatments and multiscale computer simulations. Soft matter, 2014.*

Stewart, J., Findlay, G., Smith, N., Kelly, K., and Mason, M. *Adding insult to injury - a review of the care of patients who died in hospital with a primary diagnosis of acute kidney injury (acute renal failure). Technical report, National Confidential Enquiry into Patient Outcome and Death (NCEPOD), 2009.*

Suresh, S. *Biomechanics and biophysics of cancer cells. Acta Biomaterialia, 2007.*

Svoboda, K. and Yasuda, R. *Principles of two-photon excitation microscopy and its applications to neuroscience. NNeuron, 2006.*

Tran-Son-Tay, R., Needham, D., Yeung, A., and Hochmuth, R. *Time-dependent recovery of passive neutrophils after large deformation. Biophysical journal, 1991.*

Tripathi, V. and Prasanth, K. V. *Cell nucleus. eLS, 2011.*

Tseng, Y., Lee, J. S., Kole, T. P., Jiang, I., and Wirtz, D. *Micro-organization and viscoelasticity of the interphase nucleus revealed by particle nanotracking. Journal of cell science, 117(10):2159–2167, 2004.*

Umale, S., Deck, C., Bourdet, N., Dhumane, P., Soler, L., Marescaux, J., and Willinger, R. *Experimental mechanical characterization of abdominal organs: liver, kidney and spleen. J Mech Behav Biomed Mater, 2012.*

Vlaisavljevich, E., Maxwell, A., Mancia, L., Johnsen, E., Cain, C., and Xu, Z. *Visualizing the histotripsy process: Bubble cloudcancer cell interactions in a tissue-mimicking environment. Ultrasound in Medicine & Biology, 2016.*

Wang, C. J. *An overview of shock wave therapy in musculoskeletal disorders. Chang Gung medical journal, 26(4):220–232, 2003.*

Wang, Y. and Brennen, C. *the noise generated by the collapse of a cloud of cavitation bubbles. Cavitation and Gas-Liquid Flow in Fluid Machinery and Devices, 1995.*

Webster, M., Witkin, K. L., and Cohen-Fix, O. *Sizing up the nucleus: nuclear shape, size and nuclear-envelope assembly. Journal of cell science, 2009.*

Weinberg, K. and Ortiz, M. *Kidney damage in extracorporeal shock wave lithotripsy: a numerical approach for different shock profiles. Biomechanics and Modeling in Mechanobiology, 2009.*

Weiss, L., Dimitrov, D. S., and Angelova, M. the hemodynamic destruction of intravascular cancer cells in relation to myocardial metastasis. *PNAS*, 1985.

Weiss, L. *biomechanical interactions of cancer cells with the microvasculature during hematogenous metastasis. Cancer and Metastasis Reviews, 1992.*

Williams Jr, J. C., Woodward, J. F., Stonehill, M. A., Evan, A. P., and McAteer, J. A. *Cell damage by lithotripter shock waves at high pressure to preclude cavitation. Ultrasound in medicine & biology, 25(9), 1999.*

Yuan, F., Yang, C., and Zhong, P. *Cell membrane deformation and bioeffects produced by tandem bubble-induced jetting flow. Proceedings of the National Academy of Sciences, 2015.*

Zhong, P. and Zhou, Y. *Suppression of large intraluminal bubble expansion in shock wave lithotripsy without compromising stone comminution: Methodology and in vitro experiments. The Journal of the Acoustical Society of America, 2001.*

Zhong, P., Zhou, Y., and Zhu, S. *Dynamics of bubble oscillation in constrained media and mechanisms of vessel rupture in swl. Ultrasound in Medicine and Biology, 2001.*

APPENDIX

Pressure measurement using FOPH

Experimental results of the pressure measurements inside agarose gel using FOPH.

Figure A.1 shows the voltage measurement inside agarose gel at the shock wave focus using FOPH and energy setting level 4. The experimental setup is illustrated in Section 3.1.3 and four measurement repeats were implemented to obtain the mean value. The voltage output can be converted to the pressure measurement according to Equations (3.3)-(3.6). Figure A.2 shows the converted and smoothed pressure measurement from FOPH. It can be seen that the shock wave rebounds and interferes with the surrounding due to the sample holder. However, the experimental and numerical studies only focus on the cell interaction with the incident shock waves, see Figure A.3.

The shock wave measurements are repeated for energy settings 6 and 8, see Figures A.4.

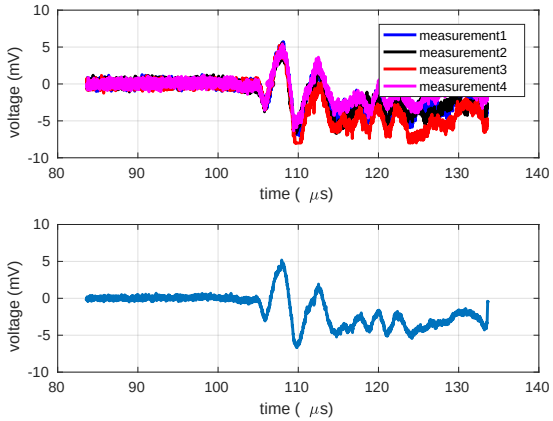

Figure A.1: Voltage output from FOPH measurement inside agarose gel at the shock wave focus.

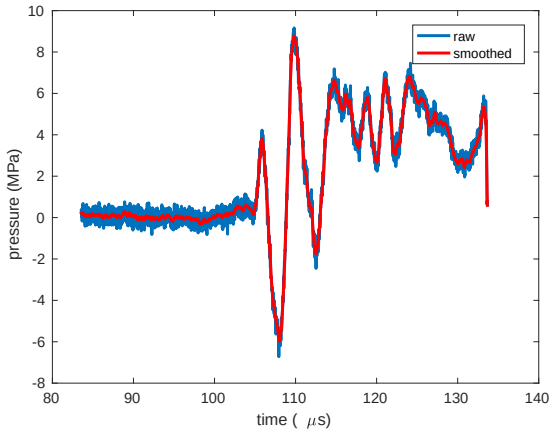

Figure A.2: Converted pressure measurement from the voltage output using FOPH.

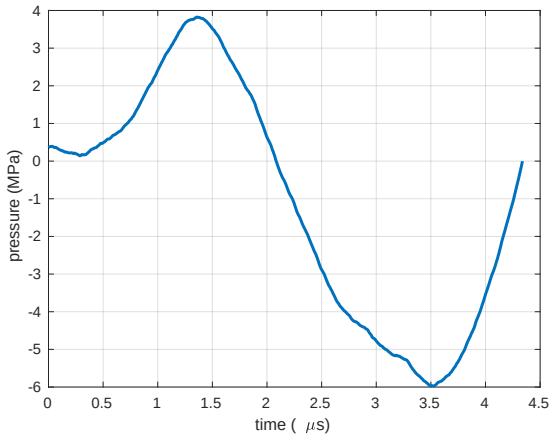

Figure A.3: The region of interest for the pressure profile.

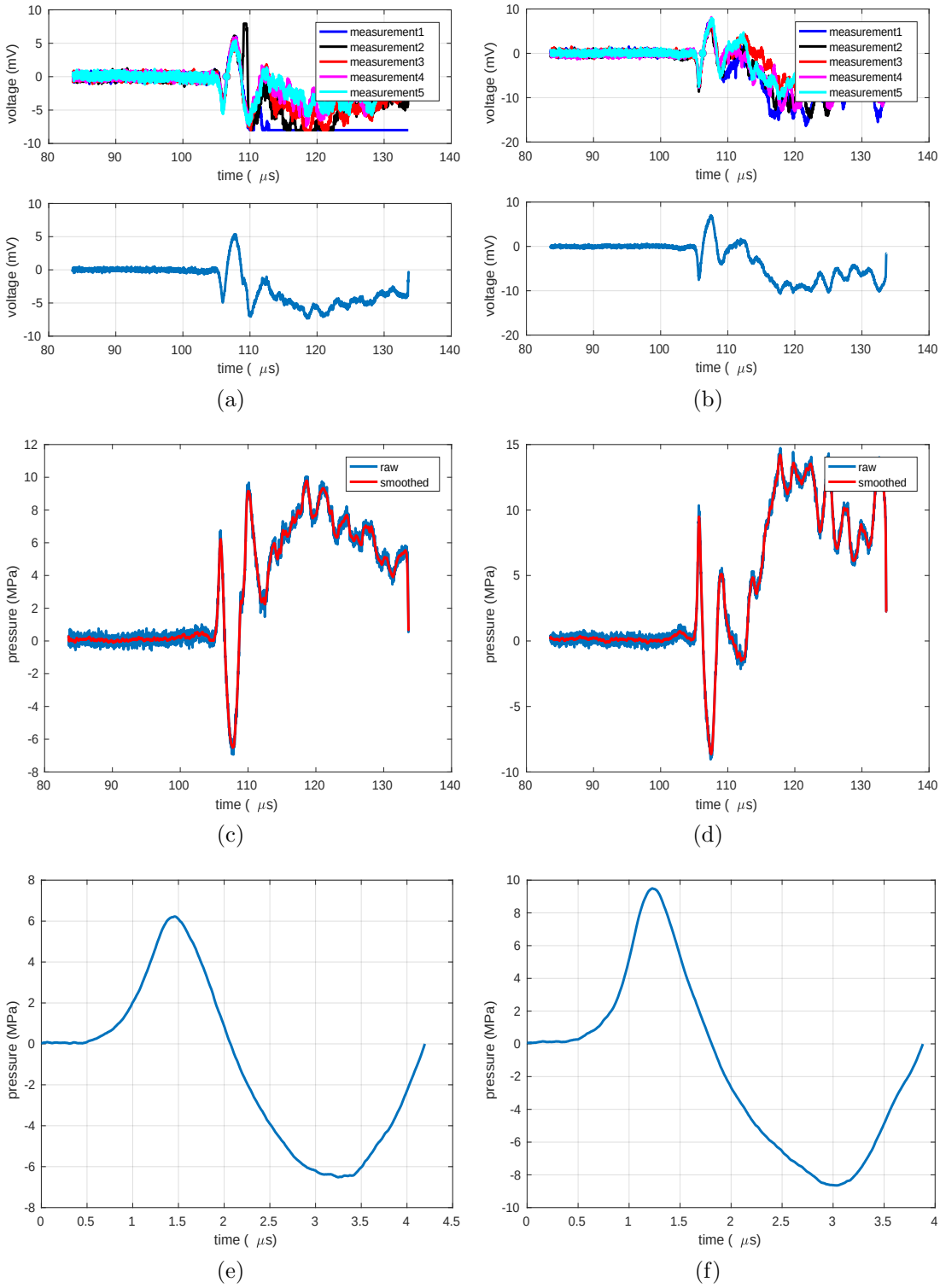

Figure A.4: Pressure measurement using FOPH at energy level 6 and level 8: (a)(b) voltage output; (c)(d) converted and smoothed pressure measurement; (e)(f) region of interest for the mean value of the pressure measurement.

APPENDIX

Mathematical Transformations

Derivation of viscoelasticity, based on the reference "computational inelasticity" (Simo and Hughes, 2008).

B.1 First order generalised Maxwell model

Figure B.1 shows the first order generalised Maxwell model denoted by a long term elastic spring, E_∞, and a viscoelastic branch consisting of a spring (E_1) and dashpot (η_1) components.

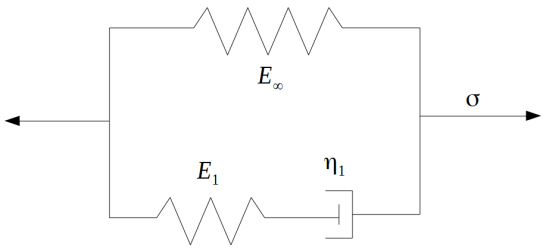

Figure B.1: 1D schematic of a first order generalised Maxwell viscoelastic model

From the figure, the stress, σ, is calculated as the sum of the long term elastic

stress, σ_∞ and viscous stress, σ_{vis}:

$$\begin{aligned} \sigma &= \sigma_\infty + \sigma_{vis} \\ \sigma_\infty &= E_\infty \varepsilon \\ \sigma_{vis} &= \eta_1 \dot{\alpha} = E_1 (\varepsilon - \alpha) \end{aligned} \tag{B.1}$$

where α and $\dot{\alpha}$ are the viscous strain and strain rate respectively.

Therefore, the stress-strain response can be expressed as:

$$\begin{aligned} \sigma &= (E_\infty + E_1)\,\varepsilon - E_1 \alpha \\ \dot{\alpha} &+ \frac{E_1}{\eta_1}\alpha = \frac{E_1}{\eta_1}\varepsilon \end{aligned} \tag{B.2}$$

Since the initial elastic modulus is defined as: $E_0 = E_\infty + E_1$, and relaxation time is defined as $\tau_1 = \frac{\eta_1}{E_1}$, Equation (B.2) can be represented as:

$$\begin{aligned} \sigma &= E_0 \varepsilon - E_1 \alpha \\ \dot{\alpha} &+ \frac{1}{\tau_1}\alpha = \frac{1}{\tau_1}\varepsilon \\ \lim_{t \to -\infty} &\alpha(t) = 0 \end{aligned} \tag{B.3}$$

With convolution integral and integration in parts, Equation (B.3) can also be expressed as:

$$\begin{aligned} \alpha(t) &= \varepsilon(t) - \int_{-\infty}^{t} exp\left[-(t-s)/\tau\right] \dot{\varepsilon(s)} ds \\ \sigma(t) &= \int_{-\infty}^{t} G(t-s) \dot{\varepsilon(s)} ds \end{aligned} \tag{B.4}$$

where $G(t)$ is the relaxation function defined as:

$$G(t) = E_\infty + E_1 exp(-t/\tau) \tag{B.5}$$

B.2 Generalised Maxwell viscoelastic model

Figure B.2 shows the schematics of the generalised Maxwell model which includes multiple viscoelastic branches.

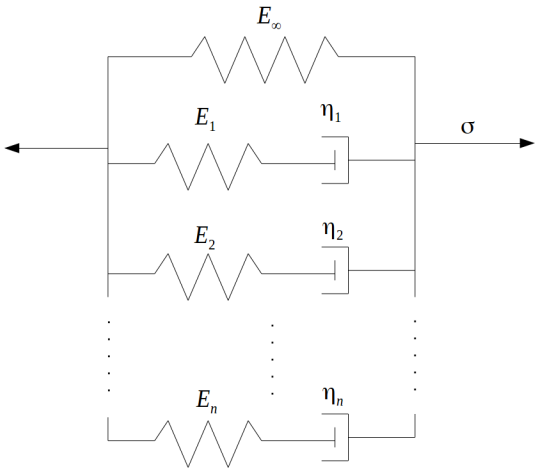

Figure B.2: 1D schematic of the generalised Maxwell viscoelastic model

Similarly to the first order case (Equation (B.3)-(B.4)), the stress response can be defined by:

$$\begin{aligned} \sigma &= E_0\varepsilon - \sum_{i=1}^{N} E_i\alpha_i \\ \dot{\alpha_i} &+ \frac{1}{\tau_i}\alpha_i = \frac{1}{\tau_i}\varepsilon \\ \lim_{t\to-\infty} &\alpha_i(t) = 0 \end{aligned} \tag{B.6}$$

which can be represented as:

$$\sigma = \int_{-\infty}^{t} G(t-s)\dot{\varepsilon}(s)ds \tag{B.7}$$

where

$$\begin{aligned} E_0 &= E_\infty + \sum_{i=1}^{N} E_i \\ \tau_i &= \frac{\eta_i}{E_i} \\ G(t) &= E_\infty + \sum_{i=1}^{N} E_i exp(-t/\tau_i) \end{aligned} \tag{B.8}$$

Define a set of stress-like internal variables q_i, nondimensional moduli γ_i and

stored energy function $W^0(\varepsilon)$ as following:

$$\begin{aligned} q_i &= E_i \alpha_i \\ \gamma_i &= E_i / E_0 \\ \gamma_\infty &= E_\infty / E_0 \\ W^0(\varepsilon) &= \frac{1}{2} \varepsilon E_0 \varepsilon \end{aligned} \tag{B.9}$$

Therefore Equation (B.6) can be expressed as:

$$\begin{aligned} \sigma &= \frac{\partial}{\partial \varepsilon} W^0(\varepsilon) - \sum_{i=1}^{N} q_i \\ \dot{q}_i + \frac{1}{\tau_i} q_i &= \frac{\gamma_i}{\tau_i} \frac{\partial}{\partial \varepsilon} W^0(\varepsilon) \\ \lim_{t \to -\infty} q_i(t) &= 0 \end{aligned} \tag{B.10}$$

B.3 Extension to 3D

Recall from Chapter 5, the stored energy can be decomposed into volumetric and deviatoric components: $W^0(\boldsymbol{\varepsilon}) = U^0(J) + \bar{W}^0(\mathbf{e})$. Therefore,

$$\begin{aligned} \boldsymbol{\sigma}(t) &= \boldsymbol{\sigma}^0(t) - \sum_{i=1}^{N} \mathbf{q}_i(t) \\ \boldsymbol{\sigma}^0 &= U^{0\prime}(J)\mathbf{I} + \mathrm{dev}[\partial_{\mathbf{e}} \bar{W}^0] \end{aligned} \tag{B.11}$$

Furthermore, the evolution of internal variables $\mathbf{q}_i$ can be expressed as:

$$\dot{\mathbf{q}}_i + \frac{1}{\tau_i} \mathbf{q}_i = \frac{\gamma_i}{\tau_i} \mathrm{dev}\left[\partial_{\mathbf{e}} \bar{W}^0(\mathbf{e})\right] \tag{B.12}$$

leading to

$$\mathbf{q}_i = \frac{\gamma_i}{\tau_i} \int_{-\infty}^{t} exp[-(t-s)/\tau_i] \mathrm{dev}\{\partial_{\mathbf{e}} \bar{W}^0[\mathbf{e}(s)]\} ds \tag{B.13}$$

Hence, the stress tensor $\boldsymbol{\sigma}$ can be represented by convolution integral.

$$\begin{aligned} \boldsymbol{\sigma}(t) &= U^0(J)'\mathbf{I} + \int_{-\infty}^{t} g(t-s) \frac{d}{ds} \left(\mathrm{dev}\{\partial_{\mathbf{e}} \bar{W}^0[\mathbf{e}(s)]\}\right) ds \\ g(t) &= \gamma_\infty + \sum_{i=1}^{N} \gamma_i exp[-t/\tau_i] \end{aligned} \tag{B.14}$$

B.4 Nonlinear viscoelasticity

Similarly, volumetric and deviatoric response are uncoupled in the finite strain viscoelasticity.

$$\begin{aligned} &\text{deviatoric deformation gradient} \quad \bar{\mathbf{F}} = J^{-\frac{1}{3}}\mathbf{F} \\ &\text{volumetric deformation gradient} \quad J\mathbf{I} = det[\mathbf{F}]\mathbf{I} \end{aligned} \tag{B.15}$$

Recall from Section 2.3.2.1, the initial stored energy function is also decomposed into volumetric and deviatoric contributions.

$$W^0(\mathbf{C}) = U^0(J) + \bar{W}^0(\bar{\mathbf{C}}) \tag{B.16}$$

where $\bar{\mathbf{C}} = \bar{\mathbf{F}}^T\bar{\mathbf{F}}$ is the deviatoric part of the right Cauchy-Green tensor.

Therefore, the initial stress (Equation (B.11)) is calculated as the derivative of the stored energy.

$$\mathbf{S}^0 = 2\partial_{\mathbf{C}}W^0(\mathbf{C}) = JU^{0\prime}(J)\mathbf{C}^{-1} + J^{-\frac{2}{3}}\text{DEV}[2\partial_{\bar{\mathbf{C}}}\bar{W}^0(\bar{\mathbf{C}})] \tag{B.17}$$

Equations (B.11) and (B.12) are thus adapted as:

$$\begin{aligned} &\mathbf{S}(t) = \mathbf{S}^0(t) - J^{-\frac{2}{3}}\text{DEV}[\sum_{i=1}^{N}\mathbf{Q}_i(t)] \\ &\dot{\mathbf{Q}}_i(t) + \frac{1}{\tau_i}\mathbf{Q}_i(t) = \frac{\gamma_i}{\tau_i}\text{DEV}\{2\partial_{\bar{\mathbf{C}}}\bar{W}^0[\bar{\mathbf{C}}(t)]\} \end{aligned} \tag{B.18}$$

Thus, the second Piola-Kirchhoff stress is expressed as:

$$\mathbf{S}(t) = JU^{0\prime}(J)\mathbf{C}^{-1}(t) + J^{-\frac{2}{3}}(t)\int_{-\infty}^{t} g(t-s)\frac{d}{ds}\left(\text{DEV}\{2\partial_{\bar{\mathbf{C}}}\bar{W}^0[\bar{\mathbf{C}}(s)]\}\right)ds \tag{B.19}$$

where,

$$g(t) = \gamma_\infty + \sum_{i=1}^{N}\gamma_i exp(-t/\tau_i) \tag{B.20}$$

B.5 Numerical discretisation

Define the expression inside the integral in Equation (B.19) as:

$$\mathbf{H}(t) = \int_{-\infty}^{t} exp[-(t-s)/\tau_i]\frac{d}{ds}\left(\text{DEV}\{2\partial_{\bar{\mathbf{C}}}\bar{W}^{\circ}[\bar{\mathbf{C}}(s)]\}\right)ds \tag{B.21}$$

Therefore,

$$\mathbf{H}_{n+1} = \int_{-\infty}^{t_{n+1}} exp[-(t_{n+1}-s)/\tau_i]\frac{d}{ds}\left(\mathrm{DEV}\{2\partial_{\bar{\mathbf{C}}}\bar{W}^{\circ}[\bar{\mathbf{C}}(s)]\}\right) ds \tag{B.22}$$

As $t_{n+1} = t_n + \Delta t_n$, $\mathbf{H}_{n+1}$ can be expressed as:

$$\begin{aligned}
\mathbf{H}(t_{n+1}) &= \int_{-\infty}^{t_{n+1}} exp[-(t_{n+1}-s)/\tau_i]\frac{d}{ds}\left(\mathrm{DEV}\{2\partial_{\bar{\mathbf{C}}}\bar{W}^{\circ}[\bar{\mathbf{C}}(s)]\}\right) ds \\
&= \int_{-\infty}^{t_n} exp[-(t_n+\Delta t_n-s)/\tau_i]\frac{d}{ds}\left(\mathrm{DEV}\{2\partial_{\bar{\mathbf{C}}}\bar{W}^{\circ}[\bar{\mathbf{C}}(s)]\}\right) ds \\
&+ \int_{t_n}^{t_{n+1}} exp[-(t_{n+1}-s)/\tau_i]\frac{d}{ds}\left(\mathrm{DEV}\{2\partial_{\bar{\mathbf{C}}}\bar{W}^{\circ}[\bar{\mathbf{C}}(s)]\}\right) ds \\
&= exp(-\Delta t_n/\tau_i)\mathbf{H}(t_n) \\
&+ \int_{t_n}^{t_{n+1}} exp[-(t_{n+1}-s)/\tau_i]\frac{d}{ds}\left(\mathrm{DEV}\{2\partial_{\bar{\mathbf{C}}}\bar{W}^{\circ}[\bar{\mathbf{C}}(s)]\}\right) ds
\end{aligned} \tag{B.23}$$

Using the mid-point approximation, and defining $\tilde{\mathbf{S}}^{\circ}(s) = \mathrm{DEV}\{2\partial_{\bar{\mathbf{C}}}\bar{W}^{\circ}[\bar{\mathbf{C}}(s)]\}$, the integration can be further approximated as:

$$\begin{aligned}
\int_{t_n}^{t_{n+1}} exp[-(t_{n+1}-s)/\tau_i]\frac{d}{ds}\tilde{\mathbf{S}}^{\circ}(s)ds &\simeq \Delta t_n exp[-(t_n+\Delta t_n-s)/\tau_i]\frac{d}{ds}\tilde{\mathbf{S}}^{\circ}(s)\big|_{s=\frac{t_n+t_{n+1}}{2}} \\
&= exp(-\Delta t_n/2\tau_i)\frac{d}{ds}\tilde{\mathbf{S}}^{\circ}(\frac{t_n+t_{n+1}}{2})\Delta t_n \\
&= exp(-\Delta t_n/2\tau_i)[\tilde{\mathbf{S}}^{\circ}(t_{n+1}) - \tilde{\mathbf{S}}^{\circ}(t_n)]
\end{aligned} \tag{B.24}$$

Therefore, Equation (B.19) is discretised as:

$$\begin{aligned}
\mathbf{S}_{n+1} &= J_{n+1}U^{0\prime}(J_{n+1})\mathbf{C}_{n+1}^{-1} \\
&+ \gamma_{\infty}J_{n+1}^{-\frac{2}{3}}\mathrm{DEV}[2\partial_{\bar{\mathbf{C}}}\bar{W}^{\circ}(\bar{\mathbf{C}}_{n+1})] \\
&+ \sum_{i=1}^{N}\gamma_i J_{n+1}^{-\frac{2}{3}}\mathrm{DEV}[\mathbf{H}_{n+1}]
\end{aligned} \tag{B.25}$$

where, $\mathbf{H}_{n+1}$ is calculated recursively:

$$\mathbf{H}_{n+1} = exp(-\Delta t_n/\tau_i)\mathbf{H}_n + exp(-\Delta t_n/2\tau_i)[\tilde{\mathbf{S}}^{\circ}(t_{n+1}) - \tilde{\mathbf{S}}^{\circ}(t_n)] \tag{B.26}$$